NUMERICAL AND EXPERIMENTAL INVESTIGATION OF BUILDING-INTEGRATED PHOTOVOLTAIC-THERMAL SYSTEMS

Liang Liao

A Thesis

in

The Department

of

Building, Civil and Environmental Engineering

Presented in Partial Fulfillment of the Requirements
for the Degree of Master of Applied Science (Building Engineering) at
Concordia University
Montreal, Quebec, Canada

September 2005

Your file Votre référence
ISBN: 0-494-10222-5
Our file Notre référence
ISBN: 0-494-10222-5

ABSTRACT

Numerical and Experimental Investigation of Building-Integrated Photovoltaic-Thermal Systems

Liang Liao

This thesis presents a numerical and experimental study of a building-integrated photovoltaic-thermal (BIPV/T) system in Concordia University, which generates both electricity and thermal energy. A 2-D computational fluid dynamics (CFD) model is developed to study the air dynamics and thermal behavior inside the BIPV thermal system and develop relationships for convective heat transfer coefficients. A 2-D k-ε turbulent model is used in the FLUENT program to simulate the turbulent flow and convective heat transfer in the cavity, in addition to the buoyancy effect. Longwave radiation between boundary surfaces is also modeled. Experimental measurements taken in a full scale outdoor test facility at Concordia University are in good agreement with the 2-D CFD model.

Velocity and temperature profiles for various average air velocities are predicted and compared with experimental data. Particle Image Velocimetry (PIV) is employed to investigate the velocity profile. Average and local convective heat transfer coefficients are generated for the system. Dimensionless correlations of local Nusselt number as a function of Reynolds number and dimensionless channel height are also generated. These heat transfer coefficients are utilized in simpler models to facilitate the design of BIPV/T systems. PV and the insulation local and average temperatures are predicted and then compared with the experimental data for different conditions and good agreement is obtained.

ACKNOWLEDGMENTS

I would like to express my special gratitude to my supervisor Dr. Andreas Athienitis for his expert guidance, encouragement and support during the graduate studies.

I would like to thank all my colleagues - Kwang-Wook Park, Panagiota Karava, Athanos, Jian Zhang, Mark Pasini, Robert Mourassa, in our group for their kind help and cooperation.

Appreciation also goes to NSERC for funding this project and Natural Resources Canada and ATS Spheral Solar for their support to this project.

TABLE OF CONTENTS

LIST OF FIGURES

LIST OF TABLES

NOMENCLATURE

BIPV/T	Building integrated photovoltaic-thermal
CFD	Computational Fluid Dynamics
C_p	Specific heat capacity of air (J/kg·°C)
G_b	Generation of turbulence kinetic energy due to buoyancy
G_k	Generation of turbulence kinetic energy due to the mean velocity gradients
H	Height of the air flow cavity (m)
h_c	Convective heat transfer coefficient in cavity (W/m^2 °C)
h_o	Exterior heat transfer coefficient (W/m^2 °C)
h_r	Radiative heat transfer coefficient (W/m^2 °C)
K	Thermal conductivity of air (W/m °C)
k	Turbulent kinetic energy
L	Characteristic length of the cavity in 2-D CFD model (m)
Nu	Nusselt number
Nu_H	Local Nusselt number according to channel height
Pe	Peclect number
Pr	Prandtl number
QUICK	Quadratic Upstream Interpolation for Convective Kinetics
Ra	Raleigh number
Re	Reynolds number
S	Incident solar radiation (W/m^2)

SIMPLE	Semi-Implicit Method for Pressure-Linked Equations
S_k	User defined source term for k
S_ε	User defined source term for ε
T	Air temperature in the cavity (°C)
T_{ref}	Reference temperature of air flow (°C)
T_{in}	Insulation temperature (facing cavity) (°C)
T_o	Ambient temperature of Concordia test facility (°C)
$P_{electric}$	Electric power generation by PV panel in BIPV/T system (W)
PV	Photovoltaic
Q_{Loss}	Energy lost to outside by convection and long-wave radiation in BIPV/T system (W)
$Q_{reflected}$	Energy reflected to the outside in BIPV/T system (W)
Q_{source}	Total solar radiation incident on PV panel in BIPV/T system (W)
$Q_{thermal}$	Energy captured by the air flow in BIPV/T system (W)
U	Air velocity in the x direction (m/s)
V	Air velocity in the y direction (m/s)
W	Width of cavity (m)
x	Horizontal direction in the air flow cavity
y	Vertical direction in the air flow cavity
Y_M	Contribution of the fluctuating dilatation in compressible turbulence to the overall dissipation rate
β	Thermal expansion coefficient (1/K)
ε	Turbulent energy dissipation rate

μ	Dynamic viscosity of air (kg/ms)
μ_t	Turbulent viscosity
ϱ	Air density (kg/m^3)
σ_k	Turbulent Prandtl numbers for k
σ_ε	Turbulent Prandtl numbers for ε

Chapter 1

INTRODUCTION

1.1 Background

Photovoltaics (PV) permit the on-site production of electricity without concern for fuel supply or environmental adverse effects. Power is produced without noise and little depletion of resources. It is expected that in the 21st century building-integrated photovoltaic systems will contribute significantly to power production.

One of the most promising applications of PV today is supplemental utility generation. A major benefit of PV is that it tends to generate more electricity at times of the year when more is needed. In most of North America, for example, utility companies struggle to keep millions of power-hungry air conditioners running in the summer months, when photovoltaic cells are most productive. Many utilities are using PV to help cover peak loads, rather than building entirely new plants. Because PV is so modular in design, these supplemental stations can easily grow from year to year, covering higher and higher loads.

Various techniques have been used to integrate the PV modules into the building envelope. For example in various countries, including Canada, amorphous photovoltaic modules are mounted as a roofing material. In Japan, insulated roof panels are designed with amorphous PV modules on the top face. Another growing area of application is placing the cells onto windows with a distance between them to create semitransparent modules that generate electricity while transmitting some daylight. In many parts of the world crystalline PV modules are integrated into the building as atrium glazing, shading device, or even as wall cladding (Athienitis and Santamouris 2002). PV systems have been designed properly and are contributing energy to human beings day after day all over the world.

1.2 Motivation

Photovoltaic modules can be integrated in buildings to form part of the exterior envelope layer. Considering the thermal energy captured by the building integrated Photovoltaic (BIPV) system, their cost-effectiveness is thus improved in comparison with stand-alone systems that need a separate support structure. Their electrical conversion efficiency, which is presently around 6-18%, is rather low in comparison with the potential thermal efficiency 50%-70% in the BIPV-thermal system. Approximately 70-80% of the solar radiation incident on PV panels is lost by convection and infrared radiation to the outdoor environment (Liao and Athienitis 2005).

By placing the PV modules in the layer of a double façade (attached to the inner or outer glazing), and passing fresh air through the glazing cavity, we achieve the twin objectives of capturing much of the absorbed solar energy that would otherwise be lost to outside, while cooling the PV panels and thereby raising their electrical conversion efficiency. Thus, the window or double façade generates both electrical and thermal energy and may also transmit some daylight if semitransparent PV is utilized. The energy efficiency is greatly increased by using this BIPV thermal system.

Having noticed the great potentials of the BIPV system, many researchers have developed various models to study the electrical performance and thermal behavior in the BIPV system. At Concordia's test facility, two configurations of BIPV are investigated (Figure 1). The first, depicted as Configuration 1 in Figure 1 (left), has the PV on the lower half of the façade, facing the outdoor environment directly. The second, depicted as Configuration 2 in Figure 1 (right), has the PV on the lower half of the façade, but placed in the middle of the cavity, permitting air to flow on either side, or both sides at the same time. Both of these BIPV/T systems are connected in parallel to a computer-controlled variable speed fan with motorized inlet dampers. In this thesis, we focus on quasi-steady state performance within 2-3 hours from solar noon in winter and spring in Montreal. Moisture effects are negligible during this period and are not considered in this thesis. Another part of this project will study integration with HVAC systems and control of the inlet damper and variable speed fan to achieve desired

average air velocity and supply temperatures. Charron and Athienitis (2003a,b) reported that when the PV modules were installed in the middle of the cavity, as in Configuration 2, the PV section overall average efficiency was up to 25% higher than if they were installed as in Configuration 1. However, electricity generation was 21% lower as the extra glazing reflected a significant portion of the solar radiation out of the system at low angles of incidence and the PV panel was hotter. With the addition of fins to maximize heat transfer from the PV, both configurations could provide combined thermal-electric efficiencies of over 60% (Charron and Athienitis 2003a).

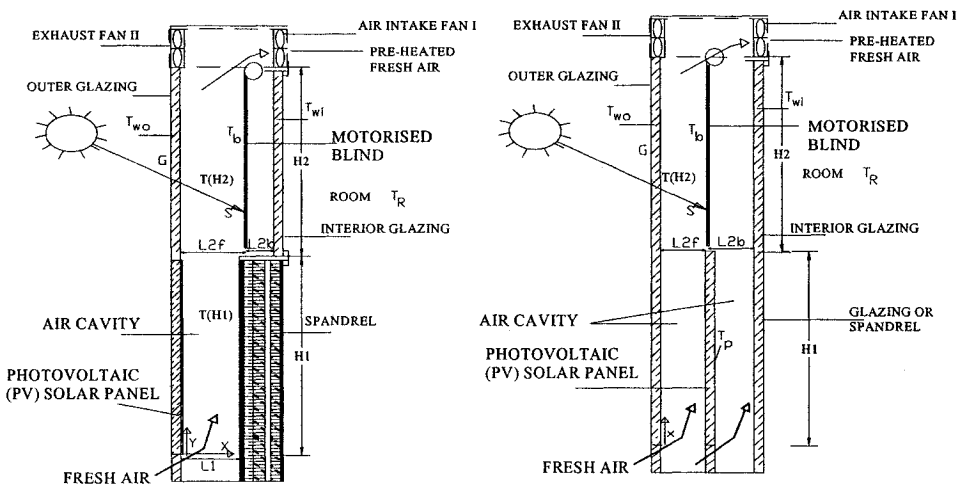

Figure 1.1: Schematic of two configurations of BIPV system in Concordia University (left side using Photowatt panels and right side using Spheral Solar panels) (Charron and Athienitis 2003a)

However, among these models, the key parameter which is the convective heat transfer coefficient is not accurately generated. Since the PV panel has geometrically increasing temperature according to height, and the coupled radiation-convection heat transfer happens inside the cavity, the convective heat transfer coefficients from the literature can hardly fit into this specific case. Some detailed fluid dynamics model coupled with heat transfer equation is thus needed to provide proper heat transfer coefficient for this photovoltaic integrated air flow cavity.

1.3 Objectives:

The objectives of this thesis are the following:

(1) To develop a two-dimensional CFD model to study the fluid dynamics in the air flow cavity of double facades with integrated photovoltaic panels, including the convective heat transfer and long-wave radiative heat transfer inside the cavity.

(2) To provide the average convective heat transfer coefficients for both the PV panel and insulation and use this convective heat transfer coefficients in Charron & Athienitis' (Charron and Athienitis 2003a, b) one-dimensional model to predict the temperature of PV panel and insulation. Basic energy balance can be achieved using this simple one-dimensional model and average heat transfer coefficients.

(3) To develop relationships for the local convective heat transfer coefficient according to height for both the PV panel and insulation. Since the flow is not fully developed in the cavity, the convective heat transfer coefficient is changing along the flow path. This function is provided and is used in Charron & Athienitis' (2003a, b) two-dimensional model to predict the accurate local PV cell temperature at a certain height.

(4) To provide the correlation of the convective heat transfer coefficients with different average air velocity. Dimensional and non-dimensional forms are provided to be used for further research.

(5) To provide experimental results and validated numerical model for later research development.

1.4 Thesis Layout

Chapter 2 examines the relevant numerical and experimental studies of BIPV system and solar collectors. In Chapter 3, the CFD model is presented from the basic equations to computer processing techniques. Experimental investigation is described in Chapter 4. The thermal

performance measurements and PIV investigation are presented. Then in Chapter 5 the CFD modeling results are presented and the convective heat transfer coefficients are generated. Modeling results are validated by comparing with experimental results in Chapter 6. Finally in Chapter 7, conclusions are drawn and future work is suggested.

Chapter 2

LITERATURE REVIEW

2.1 Introduction

Various researchers have developed models to study BIPV systems. As we will see in this section, while some researchers (Mootz 1996; Brinkworth 2002) use the laminar flow model to simulate the BIPV system, others (Zollner 2002; Moshfegh 1996) are using turbulent flow models. Some researchers model the BIPV system without the long-wave radiation calculation inside the cavity, while some researchers (Brinkworth 2002) modeled the radiation. As this study will show, the radiation exchange in the cavity of BIPV systems is important because the PV panel heats up.

In addition to modeling studies, some BIPV system operation reports and experimental investigations are also included in this literature review. From the literature review, we can see the potential market for the BIPV systems and a lot of BIPV systems are continuously contributing a lot of energy every year. The experimental studies can be used to validate the models and also these interesting projects are showing the optimized application of the photovoltaic panels and the cost-effectiveness is thus greatly improved.

2.2 BIPV System

The new type of BIPV/T systems offer architects the option to develop innovative and aesthetically pleasing designs. In Europe a recent marketing study indicated that nearly seventy percent of a sample of polled architects would consider installing PV elements in the design of new developed buildings or on existing buildings during refurbishment. Since 1990 several projects have given many opportunities for creative design and environmental innovation as photovoltaic can be applied to many parts of a building's external skin. More than 9000 square meters of PV integration have been realized already in Europe by 1996 (Benemann and Chehab 1996; Ossenbrink and Helmke 1996)

One PV-system is integrated in the façade of an office building (floor area of 8,100m^2) located in Berlin-Kreuzberg, Germany. The façade consists of granite and panels, mounted by a newly developed technique, thus creating a structural glazing façade by the use of star shaped mounting devices for both the granite and the glass panels. It generates 1689kWh of electricity with the average annual solar irradiation 596 kWh/m^2. In another administration building of the municipal utility Stadtwerke Halle, architect Heitmann used PV systems in a skylight of more than 30m length which covers a hallway. Each panel consists of three parts, where one OPTISOL energy façade element with polycrystalline solar cells is mounted between two smaller insulating glass elements. Thus a sufficient lighting of the hallway with daylight is ensured for any weather. This PV system can generate 2500 kWh of electricity with the average annual solar irradiation 800 kWh/m^2. Also in Germany, the science Park Gelsenkirchen has been created and has installed a 210 kWp generator which represents the largest roof-top power station worldwide by that time. This PV system is contributing 190,000 kWh of electricity with the average annual irradiation of 800 kWh/m^2 (Benemann and Chehab 1996).

2.3 Photovoltaic Cells

A PV module consists of solar (PV) cells permanently wired in series and/or parallel to form a single power unit, and is often packed for protection from the environment while permitting sunlight to reach the active surfaces of PV cells. When solar radiation is incident on a semiconductor, the photons may transmit their energy to the valence electrons. Each time a photon breaks a bond an electron becomes free to move through the lattice. The absent electron leaves behind a vacancy (hole) that can also 'move' through the lattice as the electrons move around it. These holes can be considered like particle (positive). The movement of electrons and holes, if passing through an external circuit, can be just like any other current source.

A solar cell is made from a semiconductor material such as silicon or gallium arsenide which sometimes acts as conductor, other times as insulator. When solar radiation is absorbed it

causes electrons to break loose from atoms, leaving atoms with a positive charge (hole). Under certain conditions the electrons and holes move in opposite directions, creating a current. In a solar cell the free electrons and hole move randomly and they eventually may recombine, or reach regions of semiconductor containing different type of impurity, called p-n junctions (p indicates conduction by holes and n by electrons). When they reach the junction, they will move through an external circuit connected at the p-n junction, creating a current (Athienitis and Santamouris 2002).

When a load is connected to an illuminated solar cell the current that flows is equal to the photogenerated current I_L due to generation of carriers by the sunlight minus the diode or dark current I_D due to recombination of carriers driven by the external voltage:

$$I = I_L - I_D \tag{2.1}$$

The current I is also often defined using short-circuit current I_{SC} and open circuit voltage V_{OC}. This definition allows us to write the characteristic I-V curve of the cell in the following form:

$$I = I_{SC}\left[1 - \exp\left(-\frac{e(V_{OC} - V)}{mKT}\right)\right] \tag{2.2}$$

where,

I_{SC} is the short circuit current

V_{OC} is the open circuit voltage

e is the charge of an electron ($1.602*10^{-19}$ C)

m is the ideality factor ($1<m<2$)

K is the Boltzman constant ($1.381*10^{-23}$ J/K)

T is the temperature of the cell

From this formulation 2.2 or the I-V characteristic curve we can find the maximum-power point as indicated at point A in Figure 2.1. For usual practical solar cells, the maximum-power point is close to the elbow of the characteristic curve.

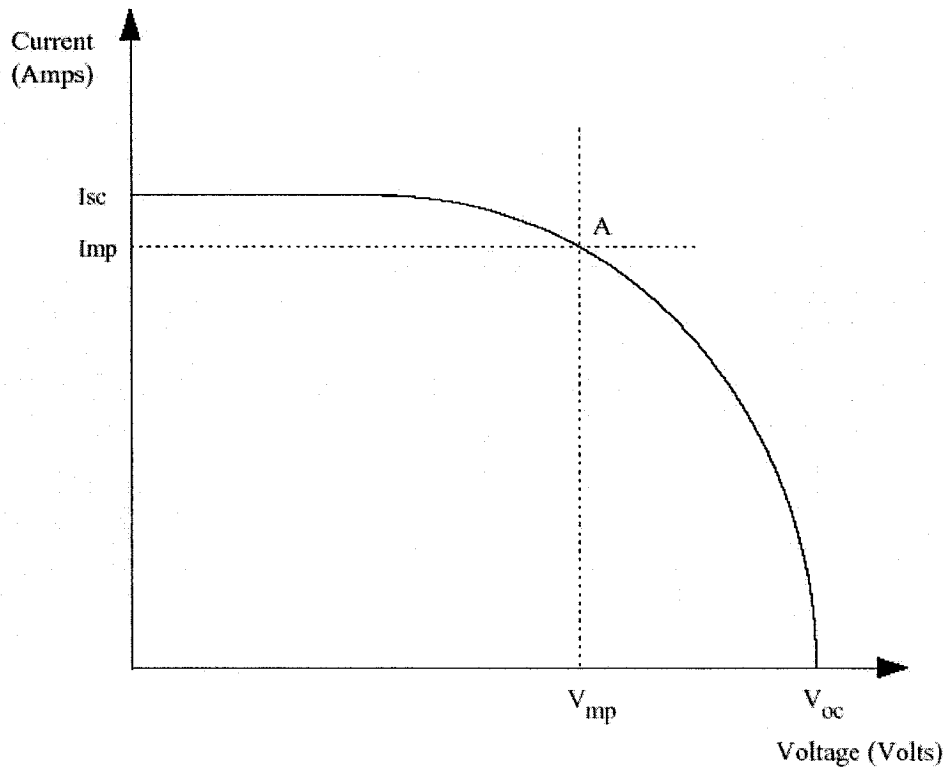

Figure 2.1 I-V characteristic curve of PV cell (Lorenzo 1994)

2.4 Solar Cell Efficiency

Part of the incident solar radiation is converted to electricity while the rest is reflected or converted to heat. An untreated surface reflects up to 35% of the incident solar radiation; surface coatings can reduce this to about 5%. Losses in the conversion of light to electricity occur because some of the sunlight (long wave) does not have enough energy to release electrons and passes through the semi-conductor to be absorbed or reflected by the base of the electrode. Ultraviolet and very short wavelength light has more energy than required to release electrons and generates heat. These two opposing effects limit the maximum

theoretical efficiency of single p-n junction cells to about 30% (Athienitis and Santamouris 2002).

Other effects such as recombination of electrons and holes at defects reduce actual efficiency further. In addition, we have resistance losses due to the cell base material, the surface layers and connections; this is modeled by a series resistance in the cell circuit. Generally the efficiency also decreases with rise in temperature (about 0.5% per °C). We also have shunt losses because imperfect cell fabrication allows current shunt paths through the junction or around the edges. These losses reduce cell efficiency to between 5 and 30% (theoretical maximum) (Athienitis and Santamouris 2002; Poissant and Dignard 2003). The correlation of the PV efficiency due to the temperature variation can be put into the following formula in a very good approximation:

$$\eta_{PV} = \eta_{ce}[1 - \beta_c \cdot (T_c - 25^{\circ}C)] \qquad (2.3)$$

where, η_{ce} is the efficiency under standard conditions and β_c is a parameter that, for crystalline silicon under practically encountered conditions, has values close to 0.4%/° C. Sanberg (1999) suggested the values of η_{ce} 13% and β_c 0.38%/ °C.

2.5 Thermal Modeling of BIPV System

Various authors have modeled the ventilated PV façade by evaluation of energy inputs and outputs through radiation, convection, conduction and power generation. Among those models, the simplest way is to use the single zone model and each element is represented by a node and connected together using the thermal network. The heat transfer through the elements is described using the U factor. Other studies have shown that modeling an AFW with a simple U-factor lacks the complexity to accurately model this type of façade (Saelens 2002).

Carla Balocco (2002) presented a simple model to study ventilated facades energy performance using a physical model to simulate the sample. A steady state energy balance was applied to a

control volume which basic equations were solved by a finite element code with an iterative procedure. The simulated system consisted of an air channel, with insulated opaque wall on the side facing the air space and with an external spherical-granite covering panel of the façade. The heat transfer of the following aspects was examined:

(1) Convective and radiative exchange between the outside ambient and external covering, including solar radiation;

(2) Radiative heat exchange between the two walls of the channel;

(3) Convective heat exchange between cavity walls and the circulating air mass

(4) Conduction through the walls

(5) Heat exchange global coefficient between the opaque wall and the inside ambient that takes into account convective and radiative exchanges.

Li Mei and David Infield (2003) modeled the PV facades system within the TRNSYS simulation program. The building model comprised of three major components: the PV façade (PV panel, air gap and inner double glazing); the solar air collectors; and a TRNSYS single zone building model together with appropriate controller models. This paper outlined the main features of the complete model. To assess the thermal impact of the ventilated PV façade, heating and cooling loads for the building with and without façade were calculated. It was found that the cooling loads were marginally higher with the PV façade for all locations considered, whereas the impact of the façade on the heating load depends critically on location. From both measurement and simulation, it could be seen that the PV façade outlet air temperature reached around 50 °C in summer and 40 °C in winter. Twelve percent of heating energy could be saved using the pre-heated ventilation of the air for the building location in Barcelona in winter season.

The Solar Energy Laboratory at Concordia University (Charron and Athienitis 2003a, b; Liao and Athienitis 2005a, b) has developed three models to study the basic thermofluid processes and to optimize the BIPV/T system:

1. A one-dimensional model that assumes isothermal surfaces but determines the exponential rise of the air temperature with height (Charron and Athienitis 2003a).

2. A two-dimensional model that divides the cavity into control volumes, allowing for the computation of the temperature distribution of the various components(Charron and Athienitis 2003b).

3. A CFD model (part of this thesis) that is intended to study the airflow behaviour within the system, and to help determine appropriate convective heat transfer coefficients to use in models 1 and 2 (Liao and Athienitis 2005a, b).

The first two models were presented by Charron and Athienitis (2003) and the third CFD model is later described with details in this thesis. A simplified version of the one-dimensional model is presented in Figure 2.2 for Configuration 1 in Figure 1.1. This model was also used for quick validation studies. The two boundary surfaces (PV panel and back insulation) were assumed to be isothermal and were assigned an average temperature from experimental data. The air flow was analyzed using finite difference method to calculate the difference between the inlet and outlet air temperatures. Then the mean air temperature was used to calculate the heat transfer with boundary elements using the thermal network.

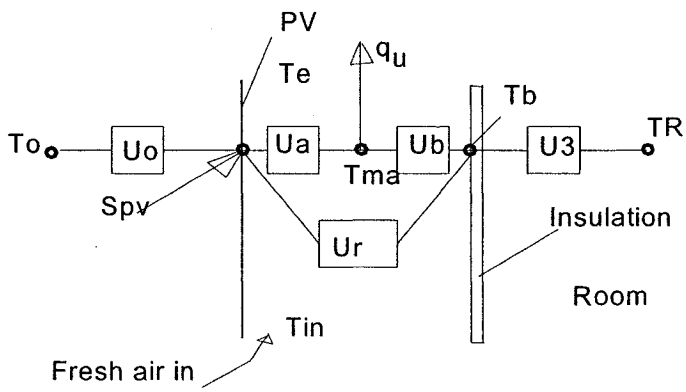

Figure 2.2: Thermal network model of ventilated façades with PV (assuming isothermal surfaces; node b indicates the back panel interior surface).

An exponential variation is obtained for the air temperature as follows:

$$T(x) = \frac{T_{PV} + T_b}{2} + \left[T_O - \frac{T_{PV} + T_b}{2} \right] \cdot e^{\frac{-2X}{a}} \tag{2.4a}$$

with

$$a = \frac{M \cdot c \cdot \rho}{W \cdot h} \tag{2.4b}$$

where M = flow rate = V × A (V is average velocity and A is cross-sectional area) and W is width of façade. Note that the h is an average convective heat transfer coefficient for two cavity surfaces. The PV and back panel temperatures are obtained as follows:

$$T_b = \frac{T_{ma} \cdot U_b + T_R \cdot U_3 + T_{PV} \cdot U_r}{U_3 + U_b + U_r} \tag{2.4c}$$

$$T_{PV} = \frac{U_0 \cdot T_0 + U_a \cdot T_{ma} + U_r \cdot T_b + S_{PV}}{U_0 + U_a + U_r} \tag{2.3d}$$

where U represents conductance between the various nodes (Uo=A·ho, Ur=A·hr, Ua=Ub=A·h, and U3 is negligible).

For most general cases, these thermal models can well predict the thermal performance and PV temperatures or insulation temperatures if proper convective heat transfer coefficients are used. The ways to determine the convective heat transfer can be found in many papers, however, they are for idealized flow and boundary conditions and they may not be suitable for our BIPV system. Thus intensive experimental validation work has to be done to find the suitable relationships. Second, the convective heat transfer coefficients used in the model are normally the average of the whole system. Since the system is working in the developing region of the cavity flow and relatively much stronger heat transfer is happening in the inlet region, the PV temperatures, insulation temperatures and the convective heat transfer coefficients all have a high gradient. Obviously, the average convective heat transfer can not

present these local effects, thus detailed study of convective heat transfer in the air flow cavity is required.

2.6 Convective Heat Transfer Coefficients

Various convective heat transfer coefficient correlations can be found in the literature. Normally they are presented in the non-dimensional form in terms of Nusselt number (Nu), Reynolds number (Re), Rayleigh number (Ra), and Prandtl number (Pr).

Balocco (2002) recommended a correlation valid for a vertical wall at uniform temperature and wide vertical isothermal volume (W>>L). Assuming Prandtl number 0.71, the Nusselt number can be calculated as follows (Holman 1991; Warren 1998):

$$Nu = \left[(Nu_l)^n + (Nu_t)^n \right]^{1/n} \tag{2.5}$$

$$Nu_l = \frac{2}{In(1 + 2/C_l \times Ra^{1/4})} \tag{2.6}$$

$$Nu_t = \frac{C_t \times Ra^{1/3}}{1 + 1.4 \times 10^9 \, \mathrm{Pr}/Ra} \tag{2.7}$$

where,

$$C_l = \frac{0.671}{\left[1 + \left(0.492/\mathrm{Pr}^{9/16}\right)\right]^{4/9}} \tag{2.8}$$

$$C_t = 0.16 \left[\frac{\mathrm{Pr}^{0.22}}{1 + 0.61 \mathrm{Pr}^{0.81}} \right]^{0.42} \tag{2.9}$$

Subscript l stands for laminar flow

Subscript t stands for turbulent flow

For air velocity higher than 4m/s the McAdam formula is often used (Holman 1991)

$$h_e = 5.7 + 3.8 \times v_v \tag{2.10}$$

While Mei and Infield (2003) argued that since the flow was in the entrance developing region and involved a combination of forced and natural convection. Another expression (Mei and Infield 2003; Incropera and Dewitt 1990) was introduced as follows:

$$\overline{Nu} = \left[\left(\overline{Nu}_l \right)^2 + \left(\overline{Nu}_t \right)^2 \right]^{1/2} \tag{2.11}$$

with

$$\overline{Nu}_l = 0.644 \sqrt{\mathrm{Re}} \sqrt[3]{\mathrm{Pr}} \tag{2.12}$$

$$\overline{Nu}_t = \frac{0.037 \mathrm{Re}^{0.8} \mathrm{Pr}}{1 + 2.444 \mathrm{Re}^{-0.1} (\mathrm{Pr}^{2/3} - 1)} \tag{2.13}$$

where

$$\mathrm{Re} = \sqrt{\mathrm{Re}_{force}^2 + \mathrm{Re}_{H,free}^2} \tag{2.14}$$

$$\mathrm{Re}_{force} = \frac{VH}{\nu}, \quad \mathrm{Re}_{H,free} = \sqrt{\frac{Gr_H}{2.5}} \tag{2.15}$$

where Re is the Reynolds number, $\mathrm{Re}_{\mathrm{force}}$ the forced convection Reynolds number calculated using the average air speed and $\mathrm{Re}_{\mathrm{free}}$ the natural convection Reynolds number calculated using Grashof number, Pr the Prandtl number and Gr_{H} the Grashof number, V the air velocity, and ν the kinematic viscosity of air (m^2/s). Using properties of air at the mean temperature, the convective heat transfer coefficient can be obtained as follows:

$$h_c = \frac{\overline{Nu} \times k_{air}}{D} \tag{2.16}$$

where k_{air} is the thermal conductivity of air and D the plate spacing.

As can be seen, the convective heat transfer coefficient is calculated using different empirical correlations in different papers. To find the proper coefficient for one specified case is not easy and often needs a lot of validation. Because of reasons mentioned above, these correlations cannot give proper values for our BIPV/T system. Detailed Computational Fluid Dynamics (CFD) simulation of the fluid flow inside the cavity is needed to solve this problem and provide appropriate convective heat transfer coefficients for our case.

2.7 Computational Fluid Dynamics (CFD) Modeling

Two main methods are often used to solve the coupled fluid flow and heat transfer problem: experimental investigation and theoretical calculation. Reliable information about a physical process is often given by the experimental measurement. However, full-scale test sometimes is not possible or too expensive. The alternative small-scale test may not reproduce all the features of the full-scale equipment, such as the turbulence. Also, some variables such as the convective heat transfer coefficients are not possible to measure directly and have to be calculated from other variables.

A theoretical prediction is based on a mathematical model which mainly consists of a set of differential equations. A look at the classical text on heat transfer or fluid mechanics leads to the conclusion that only a tiny fraction of the range of practical problems can be solved in closed form. Further, these solutions often contain infinite series, special functions, transcendental equations, etc so that their numerical evaluation may present a formidable task (Patankar 1980).

Computational fluid dynamics (CFD) techniques and models have the advantages of low cost, high speed, flexibility to sensitivity analysis, ability to simulate realistic conditions and ability to simulate ideal conditions. The fluid flow domain is divided into many tiny cells and the properties of the fluid are thus assumed constant in one cell. The continuity equation, conservation of momentum equation, and conservation of energy equation are then solved in

every single cell and information is transferred through the convection flux and diffusion flux between the cells, until the whole domain reaches stable and all equations become converged.

One promising use of CFD programs is to couple them with thermal modeling programs. Thermal modeling programs provide energy analyses for an entire building, providing space averaged indoor environmental conditions, cooling/heating loads, coil loads, and energy consumption. A drawback to these programs is that they cannot make detailed predictions of thermal comfort or predict the distributions of air velocity, and temperature like a CFD program could. Convective heat transfer coefficients used in thermal modeling programs generally come from empirical formulas that may or may not be accurate. It would be beneficial to use a CFD program to calculate these coefficients in order to improve their accuracy. Boundary conditions are a requisite for CFD programs and may be obtained from a thermal modeling program, demonstrating one of the benefits of coupling thermal modeling and CFD programs together. Coupling the two programs would allow both to acquire the necessary information in an iterative process (Zhai 2002; Bartak 2002).

Various models and investigations to study BIPV systems or double facades are reported in the literature. A 2-D finite element code was employed in a CFD study by Moshfeg (1996) and Sandberg (1999) with idealized boundary conditions. In 1996, a 2-D laminar flow model was investigated using control volume based finite difference method by Mootz and Bezian (1996). In the same year, detailed CFD studies were carried out by B. Moshfegh and M. Sandberg (1996) for both laminar flow and turbulent flows. The BIPV CFD model is further improved by introducing the radiation heat transfer in terms of the local surface temperature by Brinkworth (2002). However, this study was mainly focused on the laminar flow. Zolner et al. (2002) performed detailed experimental investigations and found that the flow was turbulent mixed convection. They report some measurements of the low velocities including different inlet sizes. In 2002, Mei et al. (2003) presented a dynamic thermal model integrated to the TRNSYS to study how the BIPV system can help to reduce the building load. However, none of the above studies used the real condition encountered in BIPV/T systems, which is non-uniform temperature profile for the PV panel.

2.8 Experimental Investigation

Dozens of the papers can be found about the experimental investigations on BIPV systems, with different experimental techniques and various component focuses. Basically, they are for two main purposes. One is to report the new discoveries or present new techniques to improve the experimental measurement. As we will see the in following paragraphs, these papers (Zollner and Winter 2002; Khedari and Rungsiyopa 2004; Morgan and Harry 2002) are going to guide the following CFD models and provide with many experimental data. The other one (Moshfegh and Sandberg 1996; Park and Augenbroe 2004) is to validate the previous CFD models and compare the experimental results with the related published modeling results.

Zollner and Winter (2002) mentioned in his paper that literature reviews showed that most of the research done in the past for electronic cooling applications has treated heat transfer by natural convection in narrow gaps. They just focused on the laminar flow situations. However, the velocity profile investigation carried out by Zollner showed that the flow was turbulent mixed flow. Due to the wind effect and turbulent variations the velocity measurement is unstable. Khedari and Rungsiyopas (2004) reported the use of a new type of vented concrete block integrating with the solar collector on the roof. They observed that the use of vented concrete block could reduce the house temperature by 2-3 °C when the window is closed and 0.5-1 °C when the window is open. Bazilian (2002) introduced the thermographic analysis to measurement of the BIPV system in Sydney, Australia. The BIPV interior PV array was measured up to 11 °C hotter than the surrounding metal roofing. This showed the significance for removal of heat off the back of BIPV modules and this also provided the graphical way to view the nature of BIPV systems.

Sandberg and Moshfegh (1996) presented an experimental investigation of a laboratory mock up of a façade provided with photovoltaic elements and made data validation of his numerical model in Part I. Surface temperatures were recorded and air velocity was recorded with tracer gas technique. They found that the radiative heat transfer transfers about 40% of the heat from the heated surface to the unheated surface. At laminar flow in the channel, both surface

temperature increase parallel with almost the same and constant slope, however, with transitional flow they also increase parallel but the slope varies with the distance from the bottom to top of the channel.

2.9 Air Velocity Measurement

The air velocity is measured in two different ways in our BIPV/T system, Hot-wire Anemometer and Particle Image Velocimetry. These two different ways both have their advantages and disadvantages. Other technique includes laser-doppler anemometry which uses a laser and associated optics to measure velocity at a point. It is not used in our BIPV/T system and is not covered in this section.

2.9.1 Hot-wire Anemometer

The basic theory for the hot-wire anemometry is to measure the convection heat flow from the ambient air flow to the hot wire. Since the conduction and radiation heat transfer is much smaller than the convection heat transfer, we can neglect them to generate the heat balance equation for an electrically heated wire:

Heat Stored = Electrical Power in – Aerodynamic Heat Transfer out (Stainback and Nagabushana 1996)

$$\frac{dc_s}{dt}T_s = P - Q$$

$$\frac{dc_s}{dt}T_s = I^2 R_s - \pi L d_s h(T_s - T_e) \qquad (2.17)$$

If the heat storage term is properly compensated, then the equation (1) becomes:

$$I^2 R_s = \pi L d_s h(T_s - T_e) \qquad (2.18)$$

For the TSI 1201, 1209 Model, they measure the bridge output voltage instead of current, and the equation becomes (TSI catalog):

$$\frac{E^2 R_s}{(R_s + R_3)^2} = \left[A + B(\rho V)^{\frac{1}{n}} \right](t_s - t_e)$$

where:

A, B = constants depending on fluid and sensor type.

ρ = density of gas or liquid.

V = velocity.

n = exponent (~2)

t_s = sensor operating temperature

t_e = *fluid* temperature

$t_s - t_e$ = ~225°F in air and 40°F in water

R_s = sensor resistance

R_3 = resistor in series with sensor (~40Ω)

E = bridge voltage (2.19)

Advantages:

The greatest advantage for hot-wire anemometry is the easy operation. It can be well used without much training and it can give satisfied results for engineering and industries. In addition the cost is not expensive. For these reasons, the Hot-Wire Anemometry is widely used in velocity measurement.

Limitations & Disadvantages:

(1) Most of the data obtained using hot-wire anemometry is limited to small perturbations. There are cases where this linearization of the anemometry equation is not accurate and non-linear effects can influence both the mean and fluctuating voltages (Corrsin 1943; Hinze 1975).

(2) Because of the mass associated with the wire supports, there can be a significant amount of heat loss from the wire due to conduction to the relatively cold supports. This heat loss results in a spanwise temperature distribution along the wire, which, in turn, causes a variation of heat transfer from the wire along its length (Kovasznay 1959; Sandborn 1972; Lowell 1950).

(3) Near wall or surface measurement can introduce errors due to increased heat transfer from the wire due to conduction to the relatively cold walls. There are cases that a hot-wire calibrated under free-stream conditions measures the velocity too high in the viscous sublayer due to this near-wall effect. (Durst 2001; Dantec Dynamics website www.dantecdynamics.com)

(4) At very low velocities the heated wire can cause a relatively significant vertical movement of the fluid due to buoyancy effects on the lower density fluid adjacent to the wire. So there is always a lowest velocity limit for Hot-Wire Anemometry (Andrews and Bradley 1972).

(5) Hot-Wire Anemometry can only provide velocity measurement at a single point in space over time. Since the Anemometry has to touch the fluids, it may disturb the flow domain in some measure (Mohammad 2002).

2.9.2 Particle Image Velocimetry

Particle Image Velocimetry (PIV) is a measurement technique for obtaining instantaneous whole field velocities. It is based on the well known equation

$$\text{Speed} = \text{distance}/\text{time} \qquad (2.20)$$

In PIV the property actually measured is the distance travelled by particles in the flow within a known time interval. These particles are added to the flow and known as seeding. Different types of seeding are used depending on the nature of the flow to be investigated. The type of seeding particle is chosen to follow the flow, and in order to detect their movement, an area of the flow field is illuminated by a light-sheet. The light-sheet, which is generated by the laser, usually has a very short time delay. This time lag for the pulses of light-sheet is the value of time used in Equation 2.20.

Advantages:

- Whole-field method.
- Non-intrusive of the flow field.

- Instantaneous measurement of the measurement domain.

Disadvantages & Limitations:

First the operation of PIV measurement needs a lot of training and patience. Second, since the PIV assumed that the tracer particles are ideal, i.e. they follow exactly the local fluid motion without altering the flow field. To obtain an unbiased estimate of the displacement field the tracer particles should be distributed homogeneously over the flow. In the near wall area, it may have some problem with the uneven distribution of seeding particles in the shear layer close to the wall (Dantec Dynamics website www.dantecdynamics.com).

2.10 Inlet Effects

Many researchers provide models to simulate the heat transfer problem of the BIPV system, depending on the incident solar energy, ambient temperatures, and air flow velocity. In these models, the ambient temperature is often used as the inlet temperature. Therefore the heat transfer near the inlet region is often missed in the thermal modeling.

Saelens and Roels (2004) studied the inlet effects for a double facade. This paper drew the attention to the importance of a correct modeling of the inlet temperature of naturally and mechanically ventilated multiple-skin facades. They took measurements on multiple-skin facades, and proved that the assumption of an inlet temperature equal to the interior or exterior air temperature was usually not valid. A sensitivity analysis was also made to illustrate the significance of the inlet temperature as a boundary condition for numerical multiple-skin facade models.

The inlet modeling is thus of importance to the whole BIPV system energy analysis. However, there is not much worth on detailed fluid mechanics modeling of the inlet. The physical features of the inlet, large turbulence, inflow and backflow uncertainty, wind effects and local climate effects, make the inlet numerical modeling coupled with many other physics. In this thesis, some qualitative analysis of the inlet is presented and comparison with Particle Image Velocitry (PIV) measurement.

Chapter 3

NUMERICAL MODELING OF BIPV SYSTEM

3.1 Problem Statement

As depicted in Chapter 1, the BIPV systems are tested at Concordia University in two different configurations (see figure 1.1). Configuration 1 with one simple cavity flow is modeled with numerical simulation. Configuration 2 can be considered as two separate cavities similar to Configuration 1 and so the results from the numerical modeling can be also used to develop the convective heat transfer coefficients for Configuration 2. In this thesis, if Configuration 2 is not specified, the discussions are all for Configuration 1.

Based on experimental measurements, we know that our problem is mainly 2-D. Measurements showed negligible temperature or velocity variation along the width of cavity. Therefore, the 2-D CFD model is used and these two dimensional are along the gap and height of the cavity.

Therefore this BIPV thermal system is simplified into two-dimensional air flow and heat transfer problem and is shown in Figure 3.1. The outside air is drawn from the bottom inlet of the cavity and the air intake temperature is measured specifically for the boundary condition setting. The flow is assumed to be quasi-steady, since the experiments show the temperatures and air flow speed barely change in a period of 2 hours around solar noon. The PV panel, located at the left side of the cavity, is heated by the solar radiation and cooled by the air flow in the cavity so its surface temperature appears a function of the height. This temperature gradient also proves that the convective heat transfer coefficient should be different along the flow path. The right hand surface in Figure 3.1 is assumed to be adiabatic (thermal insulation) but exchanges heat with the PV through longwave radiation. The air cavity as shown in Figure 3.1 has width, L=0.092 m and height, H=1 m.

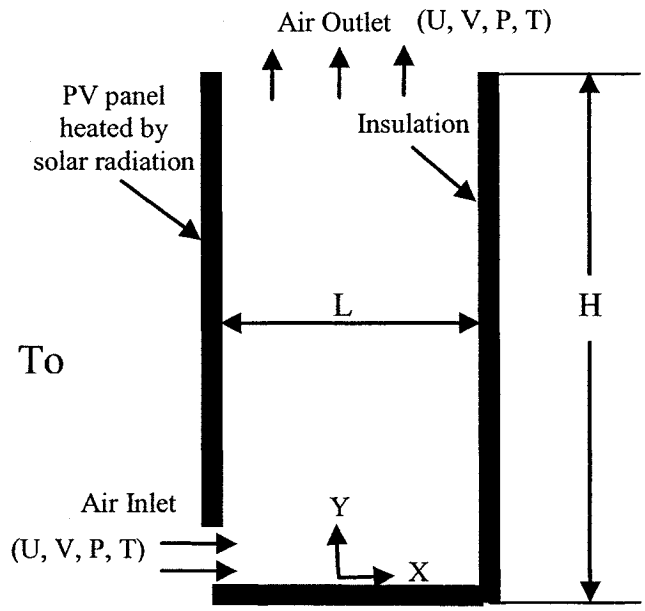

Figure 3.1 Geometry of the 2-D numerical model

The air intake temperature is measured near the intake damper and is set as the inlet thermal boundary condition. Since the inlet velocity distribution is hard to measure and sensitive to the final simulation results, the pressure difference condition is used for the inlet/outlet velocity boundary conditions. The pressure difference is pre-calculated using the pressure loss calculation according to the respective average flow speed. The outlet condition is set to the outflow condition so that only the background temperature is needed to give for the long-wave radiation heat transfer calculation from the background. The left PV panel is the most active component in the whole system, because it participates in various kinds of heat transfer: solar radiation to the outer surface, convection between the outer surface and the ambient air, background radiation between the outer surface and background, convection between the inner surface and flowing air inside the cavity, long-wave radiation between the inner surface and other surfaces inside the cavity, and possible conduction to the attached framing and other structures. For this complexity, the uniform temperature or uniform heat flux is not proper for this boundary setting, the real experimental measurements are taken and a temperature boundary profile curve is generated according to the regression of the experimental data. A CFD software FLUENT is employed to discretize and solve the governing equations.

3.2 Governing Equations

For this quasi-steady two-dimensional fluid flow and heat transfer problem, the governing equations for conservation of mass, conservation of momentum, conservation of energy, equation of the transport of turbulent kinetic energy, and equation of the turbulent energy dissipation are obtained as follows:

Continuity conservation equation:

$$\frac{\partial}{\partial x}(\rho u)+\frac{\partial}{\partial y}(\rho v)=0 \tag{3.1}$$

X-momentum conservation equation:

$$\frac{\partial}{\partial x}(\rho uu)+\frac{\partial}{\partial y}(\rho uv)=-\frac{\partial P}{\partial x}+\frac{\partial}{\partial x}(\mu\frac{\partial u}{\partial x})+\frac{\partial}{\partial y}(\mu\frac{\partial u}{\partial y}) \tag{3.2}$$

Y-momentum conservation equation:

$$\frac{\partial}{\partial x}(\rho vv)+\frac{\partial}{\partial y}(\rho uv)=-\frac{\partial P}{\partial y}+\rho g\beta(T-T_{ref})+\frac{\partial}{\partial x}(\mu\frac{\partial v}{\partial x})+\frac{\partial}{\partial y}(\mu\frac{\partial v}{\partial y}) \tag{3.3}$$

Energy conservation equation:

$$\frac{\partial}{\partial x}(\rho uT)+\frac{\partial}{\partial y}(\rho vT)=\frac{\partial}{\partial x}(\frac{K}{c_p}\frac{\partial T}{\partial x})+\frac{\partial}{\partial y}(\frac{K}{c_p}\frac{\partial T}{\partial y}) \tag{3.4}$$

Transport Equations for the Realizable k-ε Model (FLUENT6 User's Guide). Equation of the transport of turbulent kinetic energy:

$$\frac{\partial}{\partial t}(\rho k)+\frac{\partial}{\partial x_i}(\rho ku_j)=\frac{\partial}{\partial x_i}\left[\left(\mu+\frac{\mu_t}{\sigma_k}\right)\frac{\partial k}{\partial x_i}\right]+G_k+G_b-\rho\varepsilon-Y_M+S_k \tag{3.5}$$

Equation of the turbulent energy dissipation:

$$\frac{\partial}{\partial t}(\rho\varepsilon)+\frac{\partial}{\partial x_j}(\rho\varepsilon u_j)=\frac{\partial}{\partial x_j}\left[\left(\mu+\frac{\mu_t}{\sigma_\varepsilon}\right)\frac{\partial k}{\partial x_j}\right]+\rho C_1 S\varepsilon-\rho C_2\frac{\varepsilon^2}{k+\sqrt{\nu\varepsilon}}+C_{1\varepsilon}\frac{\varepsilon}{k}C_{3\varepsilon}G_b+S_\varepsilon \tag{3.6}$$

where

$$\mu_t=\rho C_\mu\frac{k^2}{\varepsilon} \tag{3.7}$$

$$C_1=\max\left[0.43,\frac{\eta}{\eta+5}\right],\eta=S\frac{k}{\varepsilon}$$

$$C_{1\varepsilon}=1.44,C_2=1.9,\sigma_k=1.0,\sigma_\varepsilon=1.2 \tag{3.8}$$

3.3 Initial Values and Boundary Conditions

Since this problem is quasi-steady, the initial values are not important for the final results. The initial values of the flow parameters and boundary conditions are specified to begin the computer process. The initial values of temperature and velocities are set equal to the ambient conditions. The turbulent kinetic energy k and turbulent energy dissipation rate ε are set to constant 1 by default. The boundary conditions are specified to simulate real conditions as follows:

(1) Outlet boundary conditions:

Pressure-outlet, P=0

(2) Inlet boundary conditions:

Pressure-inlet, T=0°C, P=Pin (range 0.3 Pa to 2.0 Pa)

(3) PV panel inner surface boundary conditions:

U=0, V=0, T(h)=Tpv(h) from experiment (function of height according to experimental data regression)

(4)Other boundary conditions:

U=0, V=0, Adiabatic Surface

All the boundary surfaces have been assumed to be gray-diffuse with emissivity equal to 0.9 and this value is confirmed by measurements with an emissionmeter. The pressure difference between inlet and outlet is set to 0.5 Pa according to flow pressure loss calculation for the average velocity equal to 0.5m/s (measured). Different pressures are also considered to study the flow dynamics and thermal behavior under different air velocities. The Reynolds number for the present case is calculated to be between 10^3 and 10^4 and the Rayleigh number is in the range 10^7 to 10^8. The Rayleigh number also depends on the boundary input of the PV panel temperatures. One example of the temperature inputs for the PV panel is from experimental data for February 18th, 2004, shown in Figure 3.2. It can be changed for different cases.

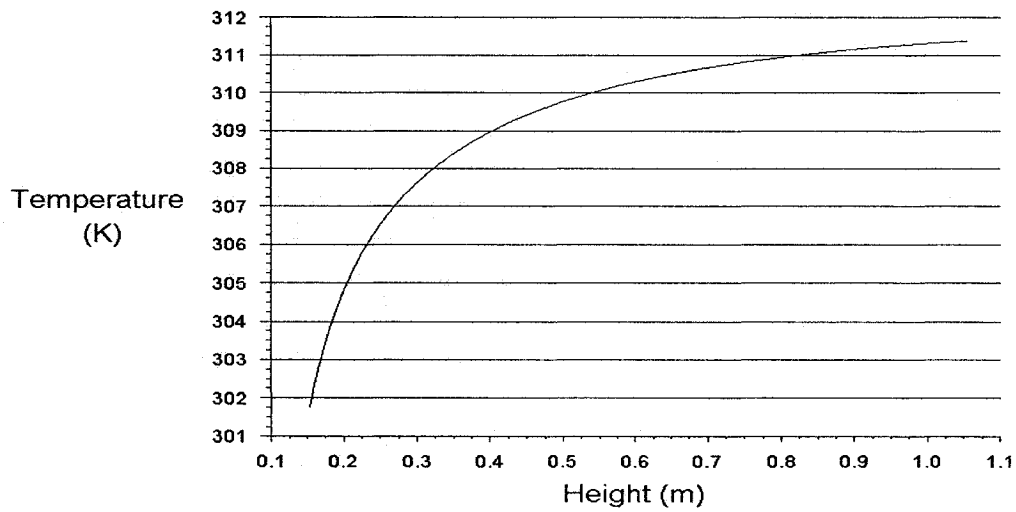

Figure 3.2 PV panel temperature profile used as boundary condition in CFD simulations.

3.4 Conduction-Convection Heat Transfer Modeling

The previous governing equations can all be generalized into one differential equation as equation (3.9). Generally, it has four terms: unsteady term (accumulation term), convection term, diffusion term (conduction term), and source term.

$$\frac{\partial}{\partial t}(\rho\phi) + div(\rho\vec{u}\phi) = div(\Gamma grad\phi) + S \qquad (3.9)$$

where Γ is the diffusion coefficient and S is the source term. The ϕ is the dependent variable and can stand for a variety of quantities, such as the mass, the velocity, the enthalpy, the turbulence kinetic energy or temperature. For different quantity of ϕ, Γ and S have specific meaning.

For example, if we consider at the continuity equation, the unsteady term disappears due to the quasi-steady condition. It can be simply derived from the generalized equation for ϕ=1, Γ=0, S=0. Then if we examine the X-momentum equation, we can still get from the generalized equation if we let ϕ=u, $\Gamma = \mu$ and S=$-\frac{\partial P}{\partial x}$. The same derivation can be used for all the other equations with proper dependent variable ϕ coefficients Γ and source term S.

To describe ratio of the strengths of convection and diffusion, Peclect number is often calculated. It is defined by:

$$Pe \equiv \frac{\rho u L}{\Gamma} \quad \text{where } \Gamma \text{ is the diffusion coefficient} \qquad (3.10)$$

When magnitude of Peclect number is low, it is diffusion (or conduction) dominant. When magnitude of Peclect number is high, it is convection dominant. In the limit of zero Peclect number, we get the pure diffusion (or conduction) problem.

Since the Reynolds number and Rayleigh number are high, the flow in BIPV/T system is convection dominant. The upwind scheme is employed for this 2-D turbulent problem. The

upwind scheme is sometimes said to be based on the "tank-and-tube" model (Gosman, Pun, Runchal, Spalding, and Wolfshtein, 1969). The control volume can be considered as the stirred tanks that are connected in series by short tubes. The flow through the tubes stands for the convection while the conduction through the tank walls stands for the diffusion. Since the tanks are stirred, each contains a uniform temperature fluid. Then the fluid flow into each other tube has the temperature that prevails in the tank on the upstream (upwind) direction. The fluid in the tube would not know anything about the tank in the downstream. This well explains the essence of upwind scheme. In addition, to avoid the false diffusion problem, in this thesis, second-order upwind scheme QUICK scheme is used for special treatment of the cavity flow, which has a 90° turning at the inlet region.

3.5 Radiative Heat Transfer Modeling

Since the PV panel is heated by the solar radiation and the temperature increases to around 310-330K high, the long-wave radiation is thus very strong inside the cavity. As we know the long-wave radiation heat transfer is coupled with the surface temperature and then coupled with the energy conservation equation and buoyancy term in the momentum conservation equations. The non-uniform distribution of the PV panel's temperature makes the radiative heat transfer more difficult to estimate. To choose the correct model to calculate this surface to surface long-wave radiative heat transfer is of great significance for the whole CFD model.

To roughly estimate the magnitude of the radiative heat transfer, the average radiative heat transfer coefficient analysis is used here. Since the surface is assumed to be gray-diffuse, and if the surface is isothermal, then we have the radiative heat transfer coefficient:

$$\bar{h}_r = \varepsilon_{eff}\sigma(T_{PV}^4 - T_{Ins}^4)/(T_{PV} - T_{Ins}) \tag{3.11a}$$

where

$$\varepsilon_{eff} = 1/\varepsilon_{PV} + 1/\varepsilon_{Ins} - 1 \tag{3.11b}$$

If the temperature difference is negligible compared to the mean temperature of the PV panel and insulation, then we can get the approximate radiative heat transfer coefficient:

$$\bar{h}_r = 4\varepsilon_{eff}\sigma T_{av}^3 \qquad (3.11c)$$

where Tav is the mean temperature of PV and insulation. Suppose that Tav is around 330 K, the value of average hr would reach about 8 W/m^2K for black diffuse walls. For most of the situations of Concordia University's test facility, the radiative heat transfer coefficient is around 4-5 W/m^2K.Compared to the convective heat transfer coefficient which is around 5-8 W/m^2K, the radiative heat transfer would be a great part of the heat transfer inside the cavity.

Due to this great significance, different radiative heat transfer models in FLUENT are tested in coupling with the CFD model and test report are showing below as table 3.1. One simple case is chosen for comparison. The flow is coming into the cavity with temperature 0 °C and flow speed 0.5 m/s. PV panel is assumed to have the uniform temperature 30 degrees. All boundary surfaces are gray-diffuse and with the emissivity 0.9.

Table 3.1 Comparison of various radiation models for coupled heat transfer calculation

	Rosseland	P1	Discrete Transfer	Surface to Surface
Total Heat Transfer Rate	269.6	387	231.3	233.1
Radiation Heat Transfer Rate	269.6	220	66.1	67.8

Some detailed temperature profiles and velocity profiles are also studied with different radiation models. As you will see from the comparison, when different algorithms are used in the numerical approach, the final profiles are different and some results are away from the real experiment results. The profiles are shown below as table 3.2.

From the comparison of these profiles to the experimental data, we can summary the features of these different radiation models as below:

- Rosseland model is only good for rough calculation. It converges fast and gives a basic idea of how much heat flux though the surface. But it cannot provide detailed information of either velocity profile or temperature profile.

Table 3.2 Temperature and velocity profile comparison for various radiation models

Models	Temperature Profile	Velocity Profile
Rosse-land	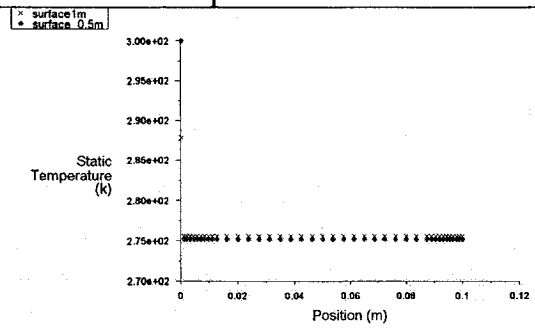	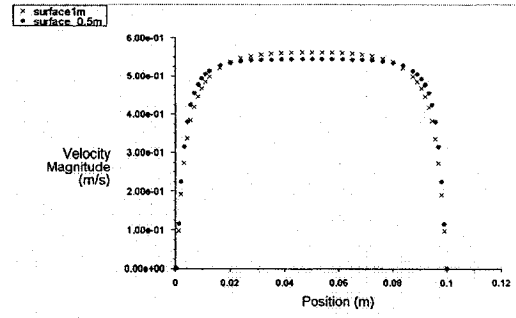
P1	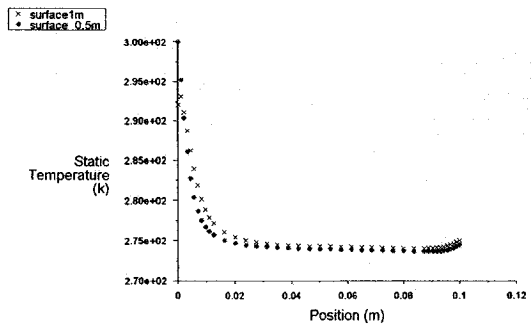	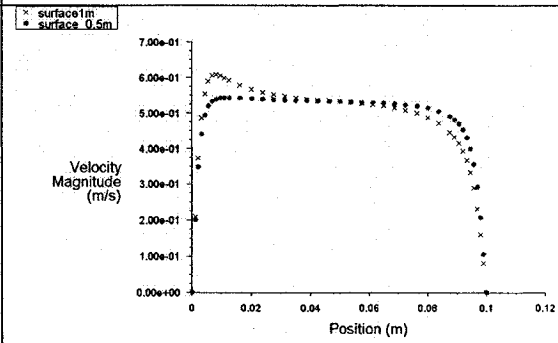
Discrete Transfer	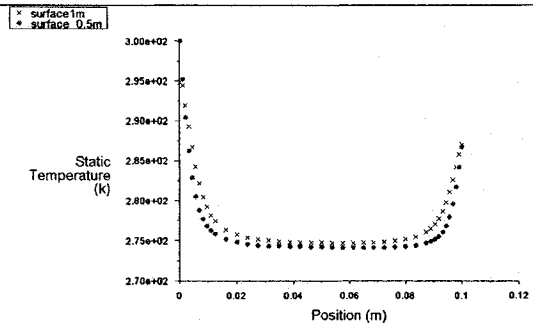	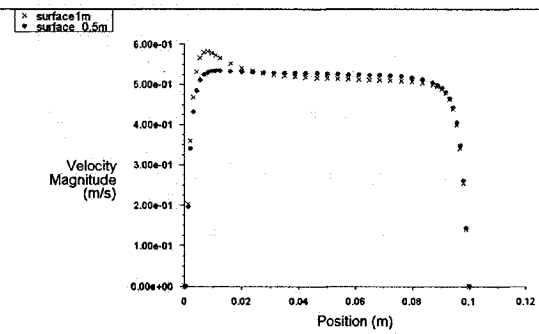

Surface to Surface	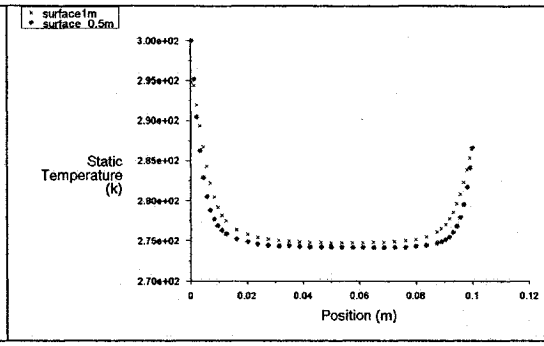	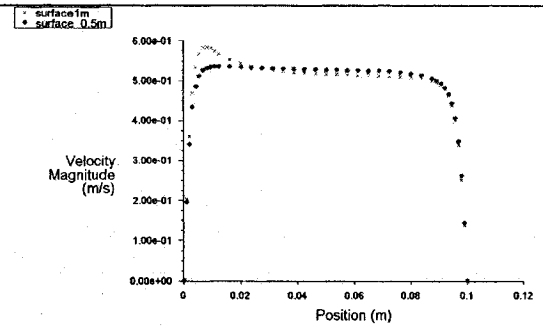

- P1 model use some simplification to calculate the radiation heat transfer and it can also give some information of the temperature and velocity profile. However, the assumptions this model made are very dependent to cases. For this cavity flow model, the results are out of accuracy range.

- Discrete Transfer model is more developed than the previous two. Both the total radiation heat transfer and the detailed profiles are very similar to the value of Surface to Surface model and experimental results.

- Surface to Surface model gives the most accurate values. Radiosity and view factors are calculated during iteration sweep. Results are very similar to the experimental data.

In this thesis the surface to surface model is used in the CFD model to calculate the radiative heat transfer. The boundary surfaces are subdivided into many elements and radiosity analysis is computed at each element. To look at the surface element k, we have net radiation in the surface element $q_{r,k}$, outgoing radiation from the element $q_{o,k}$, and incident radiation on the element $q_{i,k}$. These values can be calculated as follows:

Net radiation in element k:

$$q_{r,k} = q_{o,k} - q_{i,k} \tag{3.12}$$

Outgoing radiation from element k:

$$q_{o,k} = \varepsilon_k \sigma T_k^4 + \rho_k q_{i,k} \tag{3.13}$$

Incident radiation on element k:

$$q_{i,k} = \sum_{j=1}^{N} F_{j,k} q_{o,j} \tag{3.14}$$

Equation 3.12-3.14 can be rearranged to put into matrix form as follows:

$$[A] \cdot [Q_o] = [S] \tag{3.15}$$

where,

$$A_{i,j} = \delta_{i,j} - \rho_i F_{j,i} \tag{3.16}$$

$$S_k = \varepsilon_k \sigma T_k^4 \tag{3.17}$$

$$\delta_{i,j} = \begin{cases} 0, & if \quad i \neq j \\ 1, & if \quad i = j \end{cases} \tag{3.18}$$

The matrix A is known as the known as the radiosity matrix, the vector Q_O represents the amount of radiation leaving the surfaces, and the vector S represents the radiation emitted by the surfaces. After solving for Q_O, the vector Q_i can be found as the difference between the radiation leaving the surface, and what the surface emits, which is equal to the reflected component of the incident radiation:

$$q_{i,k} = \frac{q_{o,k} - S_k}{\rho_k} \tag{3.19}$$

3.6 Pressure-Linked Fluid Flow Problems

The special difficulty is often encountered when solving the pressure linked fluid flow problem. For pure convection-conduction problems, if proper scheme is chosen, we can start

with a guessed velocity field then what is left is the numerical iteration. However, if the fluid problem is linked with the pressure source, the pressure gradient forms part of the source term in momentum equation. Yet, there is no obvious equation for obtaining the pressure. For given pressure field, of course there is no difficulty, but if the pressure has to be solved coupled with the velocity field and temperature field, the special treatment has to be employed.

The only equation left to determine the pressure field is the continuity equation although the pressure field is very indirectly specified. When we substitute the pressure filed into the momentum equation, the resulting velocity field is then calculated to satisfy the continuity equation. Thus the pressure field is indirectly corrected. This indirect approach however is not widely used because it is not easy to realize in the computer iteration process. The convergence is quite slow since the pressure field and velocity field are interdependent.

Two approaches are taken to handle this pressure linked fluid flow difficulty. One is called "stream function/vorticity method". Since the main difficulty is the pressure field calculation, this stream function method tries to eliminate the pressure from the two momentum equations and transforms the velocity field to a stream function, vorticity equation. This approach is taken by some researchers and has some attractive advantages. First, it makes the pressure term disappeared from the governing equation. Second, instead of solving three equations, continuity equation, two momentum equations, this approach just needs to solve two equations, stream function equation and vorticity equation. Third, some of the problem is becoming easy to define and straightforward to handle, for example irrotational problems. However, the main drawback of this method is that it cannot be extended to three-dimensional situations, for which the stream function and vorticity do not exist.

The other approach, which is used in this thesis, is called Semi-Implicit Method for Pressure-Linked Equations (SIMPLE). This procedure is developed by Pantankar and Spalding (1980). In this approach, it starts with the guessed pressure field and velocity field is then generated using the momentum equation. By some mathematical assumptions, the pressure correction equation is derived and then calculated using the velocity field. Then the pressure field is corrected using new values. Then the velocity field can be renewed and all other dependent

variables are renewed accordingly. If the results are not finally converged, the iterations are repeated to update these variables. This approach contains a lot of detailed mathematical treatment of the momentum equation and continuity equation, and too detailed discussion about this method is away from the main objective of this thesis.

3.7 Mesh Generation

Since the flow has non-slip boundary condition, the velocity has a high gradient near the boundary. In addtion, due to the buoyancy effect near the hot PV panel, the velocity field is supposed to be influenced near the PV boundary. However, at the center region of the cavity, the flow is not influenced and also the temperature also is expected to stay stable, so that some coarse grids will be good enough to solve the problem. For these reasons, some special grids have to be designed to take care of the expected large gradient of these variables. Near the boundary, a geometrically increasing mesh with the expansion factor 1.05 is generated and 20 control volumes are arranged to attach each boundary layer. The Mesh pattern (60X80) is shown as Figure 3.3 below.

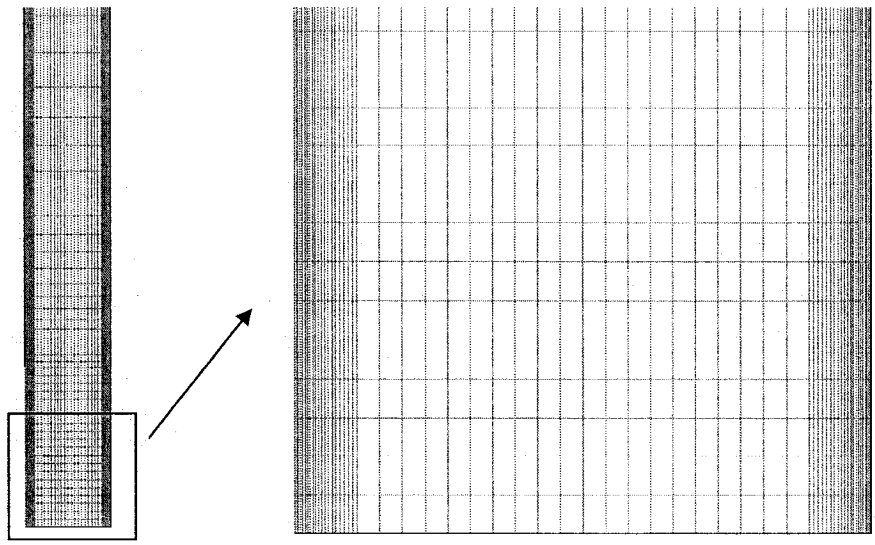

Figure 3.3 Mesh pattern for near boundary treatment

In order to assess the numerical accuracy of the results obtained by this mesh design, numerical results are compared on different meshes. One same case is studied for all different

meshes: the air flow enters the cavity with intake temperature 0 °C under pressure difference 0.5 Pa and maintains the average air speed to around 0.5 m/s. The left surface is PV panel with non-uniform specified temperature according to the experimental data. The right surface is set as adiabatic boundary. First original mesh is used for this case study, then the original mesh is refined twice (80X80, 120X80) and the same case is studied on two refined meshes. The outlet temperature profile and velocity profile are predicted on different meshes and results are compared in Figure 3.4-3.5. As can be seen, the results overlap with each other on different grids. Convective heat transfer coefficients are then generated on these different grids, and from Figure 3.6 we can observe that these different grids generate the convective heat transfer coefficients with negligible difference. Therefore, the further refinement of the mesh becomes not necessary and the original mesh is later used for this problem.

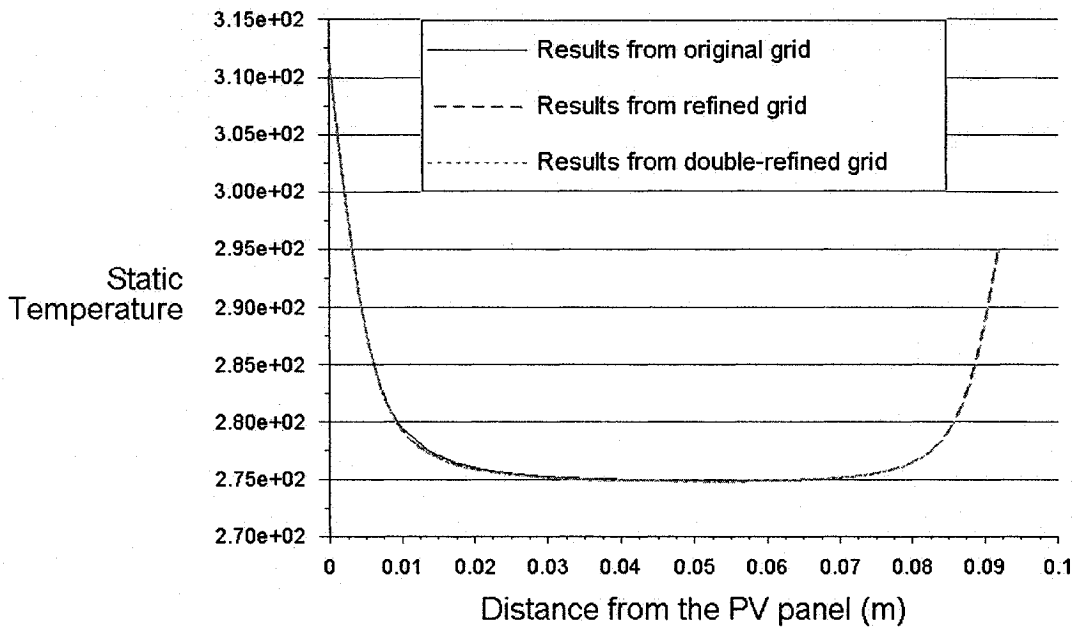

Figure 3.4 Comparison of temperature profiles at outlet of the cavity on different grids

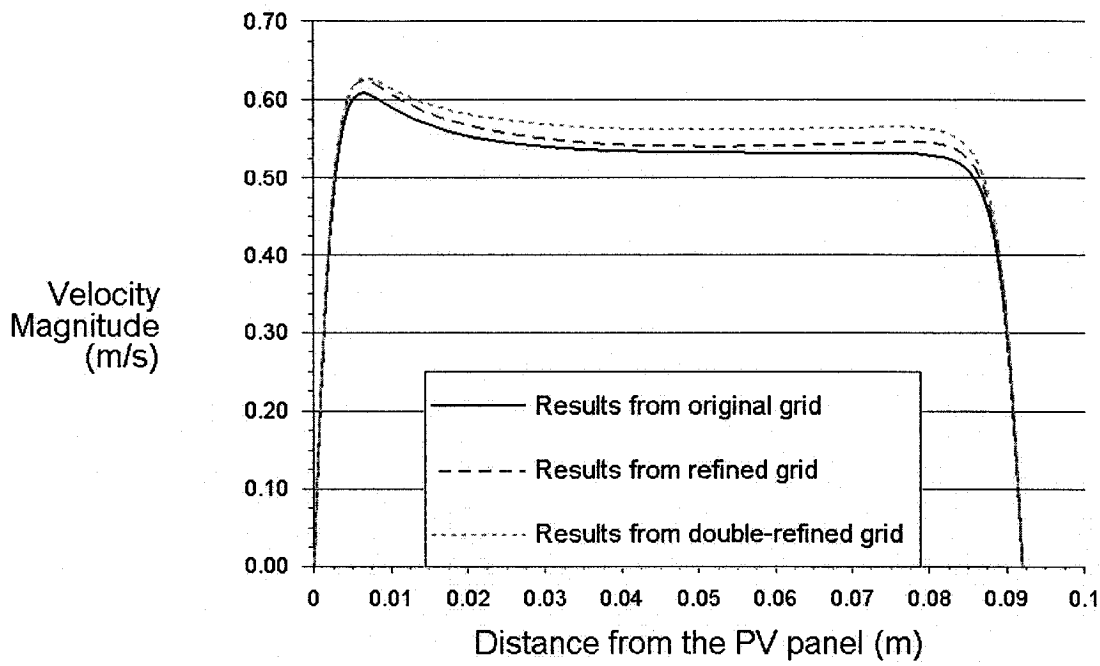

Figure 3.5 Comparison of velocity profiles at outlet of the cavity on different grids

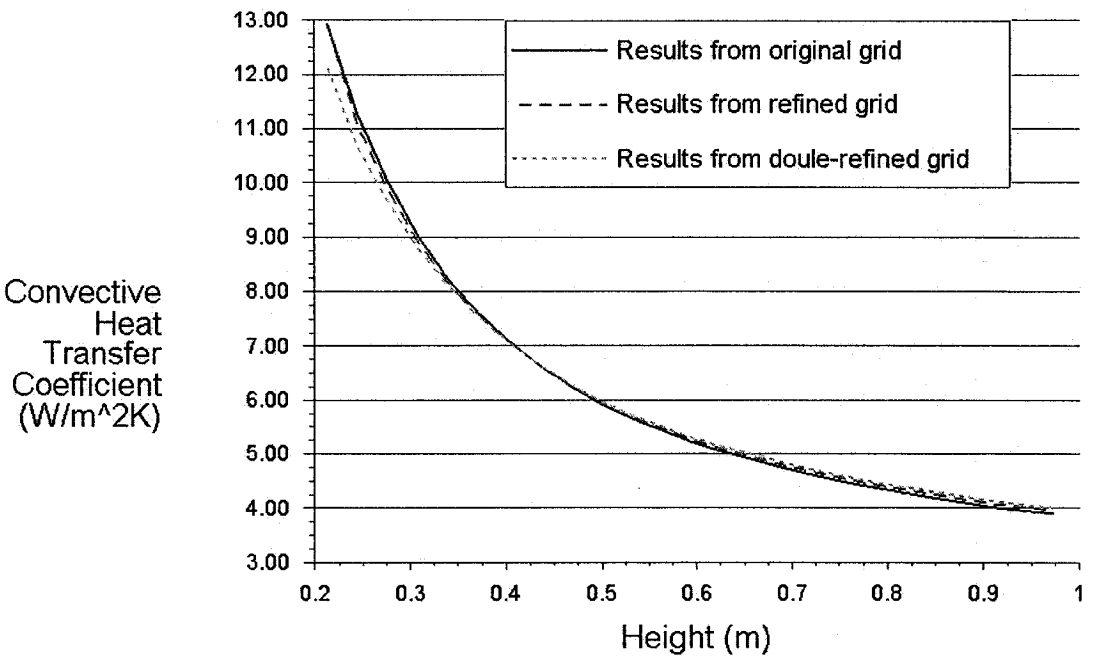

Figure 3.6 Comparison of convective heat transfer coefficient profiles on different grids

3.8 Computer Process

The governing Equations (3.1) - (3.8) with the given boundary conditions are discretized and solved using FLUENT 6.1. A control volume based finite difference method is used to simulate the flow region in the cavity. The realizable k-ε model employed by FLUENT is utilized with constant fluid properties except for the buoyancy term of the momentum equations, where the Boussinesq approximation is used to account for the density variation. The full buoyancy effect is also considered in the k-ε turbulent model. For the longwave radiation heat transfer, view factors and radiosity are computed using surface to surface radiation model and it was assumed that the surfaces are gray-diffuse and the fluid is transparent to radiation. Since detailed analysis is desired near the boundaries, a finer grid is employed in those regions in addition to the enhanced wall treatment that is utilized for the k-ε turbulent model.

To facilitate numerical convergence the pressure-velocity coupling problem is solved using SIMPLEC scheme; momentum, energy, turbulence kinetic energy and turbulence dissipation rate equations are solved using QUICK scheme. To overcome the difficulty of numerical convergence, the under-relaxation factors for pressure, momentum, turbulence kinetic energy and turbulence dissipation rate are set to 0.5, 0.7, 0.8 and 0.8, respectively. The convergence criteria are less than 10^{-4} for all equations and 10^{-8} for the energy equation. These criteria are further tested. When the criteria are put into one order higher, the differences of the final results change less than 1%. In addition, since there is no heat source inside the calculation domain, the net heat transfer rate is supposed to converge to 0 after all dependent variables get converged. This physical criterion is double checked to make sure the final energy balance for the whole BIPV thermal system is achieved. The computer processing time is dependent on the complexity of the governing equations and criteria for the dependent variables. For most cases, the numerical results get converged after 1500-2000 times of iterations.

3.9 Integration with Charron&Athienitis' 2-D Model

The CFD model presented in this thesis is to study the fluid dynamics and thermal behavior

details inside the air flow cavity, and for these purposes the measured PV surface temperature profile is set as the boundary condition. The convective heat transfer coefficients can be generated. However, to predict the electrical and thermal performance of the PV panel, the surface temperature has to be predicted. For this objective, some thermal network model with the heat balance calculation is needed to cooperate with 2-D CFD model. Charron&Athienitis' 2-D model (Charron and Athienitis 2003a) is used in this thesis.

The integration procedure is shown as Figure 3.7. The guessed values of the surface temperatures or surface temperature profiles obtained from the experiment are first used in the FLUENT model as boundary conditions. After computer process, the convective heat transfer coefficients will be generated. The correlation of the convective heat transfer coefficient profile for respective velocity and height is then used to substitute into Charron&Athienitis' 2-D model to calculate the new surface temperature profiles. This new temperature profile is calculated using the thermal network heat balance calculation, in which the PV panel is considered as one component in the macro BIPV system. Later, the updated surface temperatures are compared with the CFD model settings in FLUENT. If the surface temperature profile doesn't change much (less than 2% variance), the final results of the PV temperatures, insulation temperatures and convective heat transfer coefficients can be obtained. If not, the updated surface temperature profile has to be reset into FLUENT model and the whole iteration begins from the beginning again.

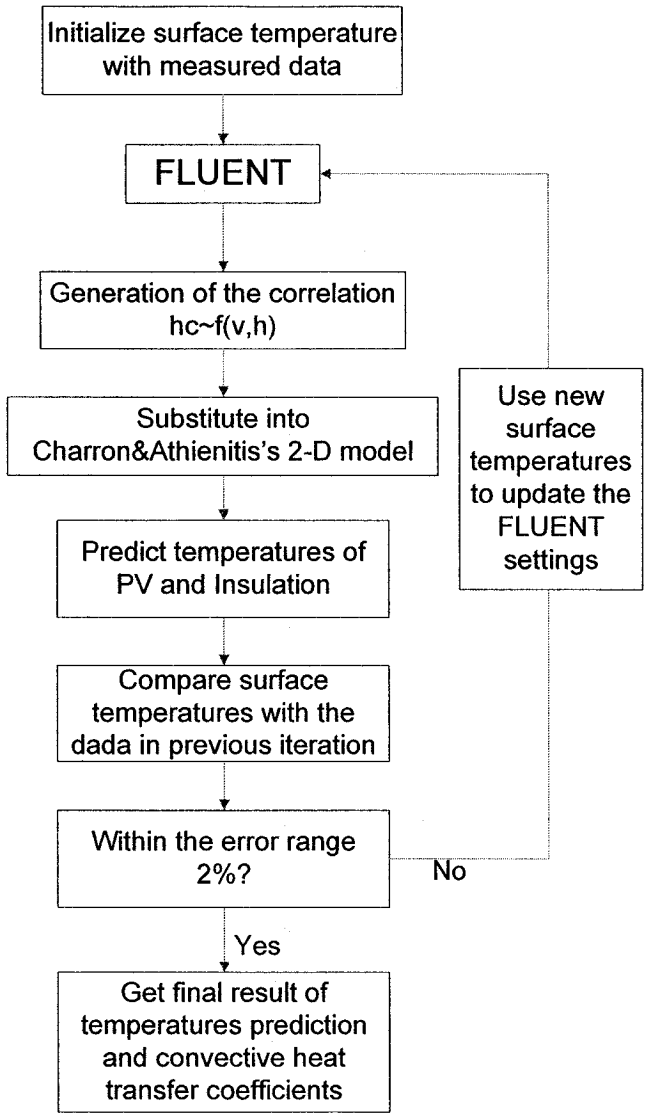

Figure 3.7 Generation of hc and integration with 2-D model (Charron&Athienitis 2003)

Chapter 4

EXPERIMENTAL INVESTIGATION OF BIPV SYSTEM

4.1 Test Facility Introduction

The experimental investigation is of great significance for research, not only because it can provide sufficient data to validate the modeling results, but also because the discoveries found by the experiment investigation can lead the direction of theoretical studies and thus improve the physical model.

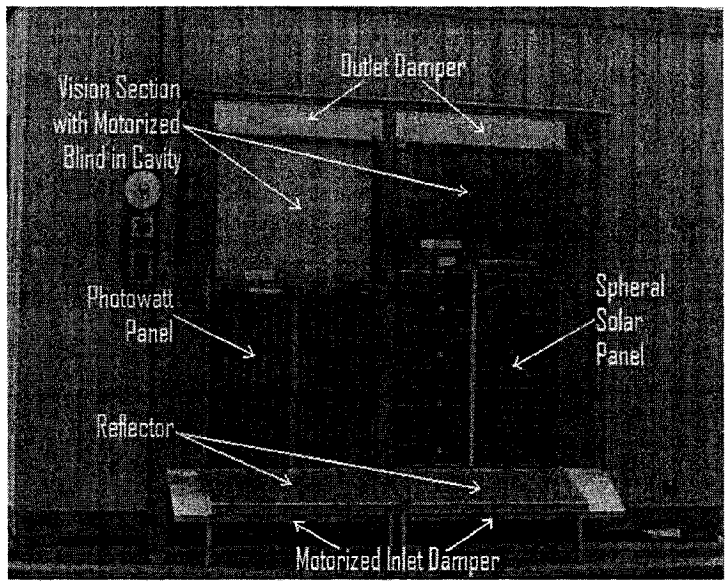

Figure 4.1 Photograph of Concordia's building-integrated PV test facility.

A test room was built at Concordia University to investigate the application of BIPV/T system. It has interior dimensions of 2.972 m x 2.896 m x 3.045 m, with a total interior floor area of 8.61 m^2. At Concordia's test facility, two configurations of BIPV thermal systems are intensively investigated (Figure 4.1). The first, depicted as Configuration 1 in Figure 1.1 (left), has the PV on the lower half of the façade, facing the outdoor environment directly. The Photowatt panel is mounted as shown in Figure 4.1 on the left hand side. The second, depicted as Configuration 2 in Figure 1.1 (right), has the PV on the lower half of the façade,

but placed in the middle of the cavity, permitting air to flow on either side, or both sides at the same time. The spheral solar panels are mounted inside the cavity as shown on the right hand side of Figure 4.1. Both of these BIPV/T systems are connected in parallel to a variable speed fan with motorized inlet dampers.

Configuration 1 is studied with detailed CFD model and Charron&Athienitis' 2-D heat transfer model. The convective heat transfer coefficients are generated for different average air velocities. PV temperature and insulation temperature can be predicted using respective heat transfer coefficients. The experimental investigation is carried on to compare with modeling results.

The CFD model is using the same geometry as the experiment. The width of the air flow cavity is 0.092 meters and the height of the cavity is 1 meter. However, when comparing the modeling predictions with the experimental results, it must be considered that some of the boundary conditions are different. The main differences are summarized and given in table 4.1 as below. The experimental investigation and CFD modeling can be complementary to help to understand and predict the thermal performance of the BIPV system.

Table 4.1 Main differences between CFD model and experiment

Main Differences	CFD Model	Experiment
Perfectly insulated from the room side conditions	Yes	No
Transitional flow consideration	No	Yes
Wind effect near the inlet region	No	Yes
Air leakage	No	Yes
Rough surface and irregular shape of the inlet	No	Yes

4.2 Experiment Instrument

This BIPV/T system is investigated at Concordia University's test facility as presented in

previous section. Since the electrical performance is linked with the thermal performance, and thermal behavior is coupled with the air dynamics in the air flow cavity, the investigation of this system requires different kinds of sensors and a careful arrangement of all these sensors.

The list of measuring sensors is presented below in table 4.2. First, ambient conditions are detected in every minute by LICOR weather station LI-1401 Agro-Meteorological Station. The variables measured by this sensor include solar radiation (W/m^2), air temperature (°C), relative humidity (%), vapor pressure (kpa), wind speed (m/s), wind direction (degrees), precipitation (mm), soil temperature (°C), and dew point (°C). Among these variables, we are most interested in solar radiation, air temperature, and wind speed. For most accurate investigation of the wind effect, another wind sentry is utilized. It is Model 03002V from YOUNG Company. The ambient temperature sensor is covered with Multi-Plate Radiation Shield, provided by YOUNG Company model 41003. The error from the solar heating on the temperature sensor can be eliminated. Two pressure sensors are employed; one is from ASHCROFT Company model XLdp, the other is from Dwyer Company model 607-0. They both are good at low pressure difference measurement. The hot-wire anemometer is utilized to measure the flow speed in the cavity. Series 640 air velocity transmitter from Dwyer Company is installed in the system to check the flow speed within accuracy ±2%. Dozens of T-type thermocouples are mounted inside the cavity. The arrangement will be discussed later. Some shield cups are designed to avoid the direct solar radiation at the thermocouples. Also, the damper can be proportionally controlled by Model LM24-SR-2.0 US from Belimo Company. The variable frequency fan is used to control the air flow. Model M1105SB from AC Technology Corporation is employed for this application.

Table 4.2 List of sensors for BIPV system measurement

Item	Company	Model	Power supply	Measuring range	Output Type	Accuracy (percentage of full span output)
Wind Sentry	YOUNG	03002V	8-24VDC	0-50 m/s (112mph)	0-1.0VDC	±0.3m/s
Solar Radiation Meter	LICOR	LI-1401	7-16VDC	0-1500W/m^2	90μA(1000W)$^{-1}m^{-2}$	±5%
Ambient conditions	LICOR	LI-1401	7-16VDC	-40°C- 60°C 10-90% RH	0-1.0VDC	±0.8°C ±3%

sensor						
Wind Sensor	LICOR	LI-1401	7-16VDC	0-112mph	0-1.0VDC	±1.1mph
Pressure meter #1	ASHCROFT	XLdp	12-36VDC (24VDC typical)	-0.25/0.25 WC (±62.5Pa)	4-20 mA	0.5%
Pressure meter #2	Dwyer	607-0	12-36VDC unregulated	0-0.10 WC (0-25Pa)	4-20 mA	0.5%
Air velocity meter (Hot-Wire)	Dwyer	Series 640	18-24 VAC or 22-28 VDC	0-200 FPM	4-20 mA	5% (0-80 C)
				0-1000 FPM		2% (0-80 C)
				0-3000 FPM		2% (0-80 C)
				0-12000 FPM		2% (0-80 C)
Air velocity meter (PIV)	DANTEC	2-D	110VAC		Computer integration	Less than 1%
Thermocouples	T-type					±2°C
Damper Control	BELIMO	LM24-SR-2.0 US	24VAC ±20% 50/60HZ 24VDC ±10%	Angel of rotation: Max 95° (20%-100% electronically adjustable)	2-10 VDC 4-20 mA Control signals	
Variable Frequency Fan	AC TECH	M1105SB	120/240VAC	0-60Hz	0-230V 0-120Hz	
Data Logger	Agilent	34970A	120VAC			

4.3 Energy performance measurement

To examine the dependance of the thermal performance and electrical performance, and to optimize the combined system efficiency, including thermal efficiency and electrical efficiency, the thermal behavior inside the cavity is carefully measured. Dozens of thermocouples are arranged and mounted by Kwang-Wook and me to measure the temperature profile in different heights (Liao and Athienitis 2005a).

Figure 4.2 (a) shows the arrangement of the thermocouples for Configuration 1 (Photowatt side) and Figure 4.2 (b) shows the arrangement for Configuration 2 (Spheral solar side). Five thermocouples are mounted along the height on the PV panels, and two extra thermocouples are mounted at the mid-height line to investigate the average temperature with higher accuracy. They are circled with red line in the picture. Five thermocouples are mounted along the height of insulation board and all are circled in the picture with green line. Thermocouples are also mounted to measure the temperature profile of the air gap. Five thermocouples along the line

are designed at the top and bottom of the cavity for the air gap profile, and three and designed at the middle, middle-top and middle-bottom. Thus, the thermal behavior could be investigated along the height and the temperature gradient could be observed.

The measured temperature at different positions for Configuration 1 (Photowatt side) is shown in Figure 4.3. This experimental investigation is an example from the average data between 11:30 and 12:30 on March 14th 2005. From the data we got on that day, we calculated the thermal performance in a Mathcad program. The results are presented below and the original program is listed as appendix A. The average temperature of PV panel and insulation are calculated to be 27.4 °C and 8.8 °C respectively. Average air speed is measured to be 1.15 m/s. Average temperature at the top of the cavity is calculated 5.2 °C thus the temperature increase through the cavity is 5.2-0.9=4.3 °C. Thus the thermal energy captured by the air can be calculated:

$$Q_{thermal} = \dot{m} c_p \Delta T = \rho \cdot v \cdot L \cdot W \cdot c_p \cdot (T_{top} - T_{intake}) = 535.1W \quad (4.1)$$

The electrical performance is optimized using the maximum-power point tracking according to equation 2.2 and I-V characteristic curve (Figure 2.1). The resistances for the maximum-power point are found to be 15.7 ohms for configuration 1 (Photowatt side) and 29.0 ohms for configuration 2 (Spheral solar side). The electrical energy generated is calculated by measuring the load resistance and the voltage drop across the resistance. The electric power is calculated to be 84.7 W. Therefore, we can have the system efficiency and electrical efficiency as below:

$$\eta_{total} = \frac{Q_{thermal} + P_{electric}}{S \cdot A_{PW}} \cdot 100\% = 62.1\% \quad (4.2)$$

$$\eta_{electric} = \frac{P_{electric}}{S \cdot A_{PW}} \cdot 100\% = 8.5\% \quad (4.3)$$

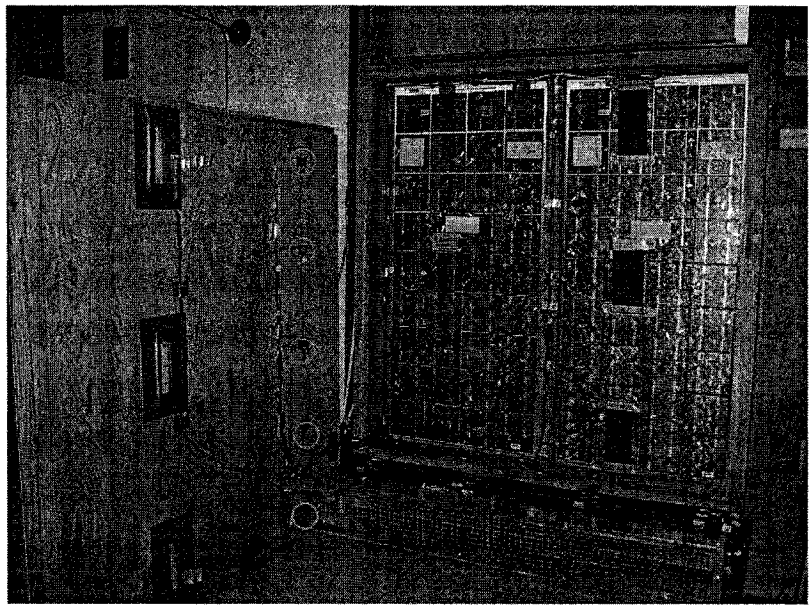

Figure 4.2 (a) Photograph of the arrangement of thermocouples for configuration 1 (Photowatt side)

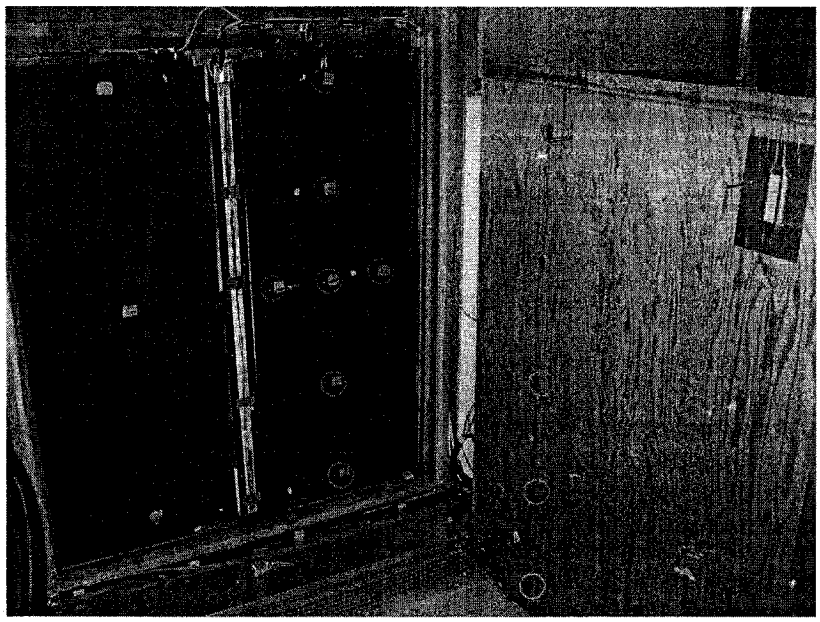

Figure 4.2 (b) Photograph of the arrangement of thermocouples for configuration 2 (Spheral solar side)

To check the validity of these experimental data, a simple calculation of the energy balance can be utilized. As we know, the incident energy into the BIPV system is the source of the BIPV

system Q_{source}. (A reflector coefficient is used here to compensate the energy reflected from the inlet damper reflector to the PV panel.) It should equal to the energy captured by the incoming air plus the electricity generated by the PV panel plus the energy wasted to the outside (note that the insulation reduces heat transfer to the room to a negligible amount).

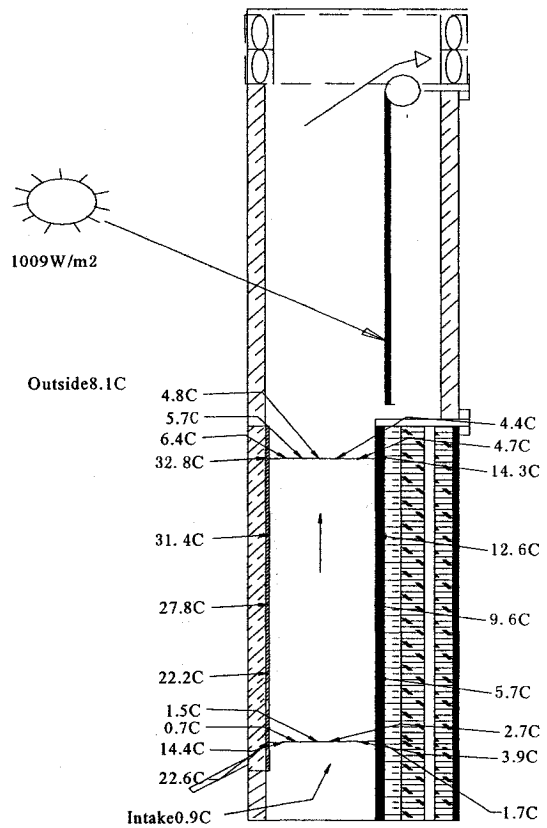

Figure 4.3 Experimental data of thermal performance for configuration 1 (Photowatt side)

$$Q_{source} = \eta_{refl} \cdot S \cdot A_{PW} = 998W \tag{4.4}$$

$$Q_{reflected} = \rho_{ref} \cdot S \cdot A_{PW} = 99.8W \tag{4.5}$$

$$Q_{Loss} = h_o \cdot (T_{gla\_ave} - T_o) \cdot A_{PW} = 215.4W \tag{4.6}$$

$$Q_{thermal} + Q_{Loss} + Q_{reflected} + P_{electric} = 535.1W + 215.4W + 99.8W + 84.7W = 935W \quad (4.7)$$

Therefore, we can have the energy balance equation:

$$Q_{source} \approx Q_{thermal} + Q_{Loss} + Q_{reflected} + P_{electric} \quad (4.8)$$

A similar experimental result for Configuration 2 (Spheral solar side) is shown in Figure 4.4 on the same day. The thermal analysis and heat balance calculation can be also found in Appendix A. From the experimental data, we can see that the average temperatures of PV panel, outer glazing, and insulation are 34.0 °C, 24.0 °C and 12.7 °C respectively. The PV average temperature is 6.6 °C higher than for configuration 1 (Photowatt side). However, the temperature rise is 9.4 °C which is double the temperature rise of Configuration 1 (Photowatt side). The thermal energy captured by the air is 833.7W. This high thermal efficiency makes the total system efficiency to be 78%, although the electrical efficiency is as low as 4.3% in this case. However, we need to note that the panels used on this side have a lower electrical efficiency (about 6% max.). The similar energy balance calculation could also be achieved at this Configuration 2 (Spheral solar side). The source radiation incident into the system is calculated to be 1133 W. The electrical power generation and lost energy to the outside are 49 W and 301.2 W respectively. Therefore, if we put all energy (generated, captured and lost) together, we can have the value 1184 W, which is within 5% error of the incident solar energy. The energy balance is thus achieved.

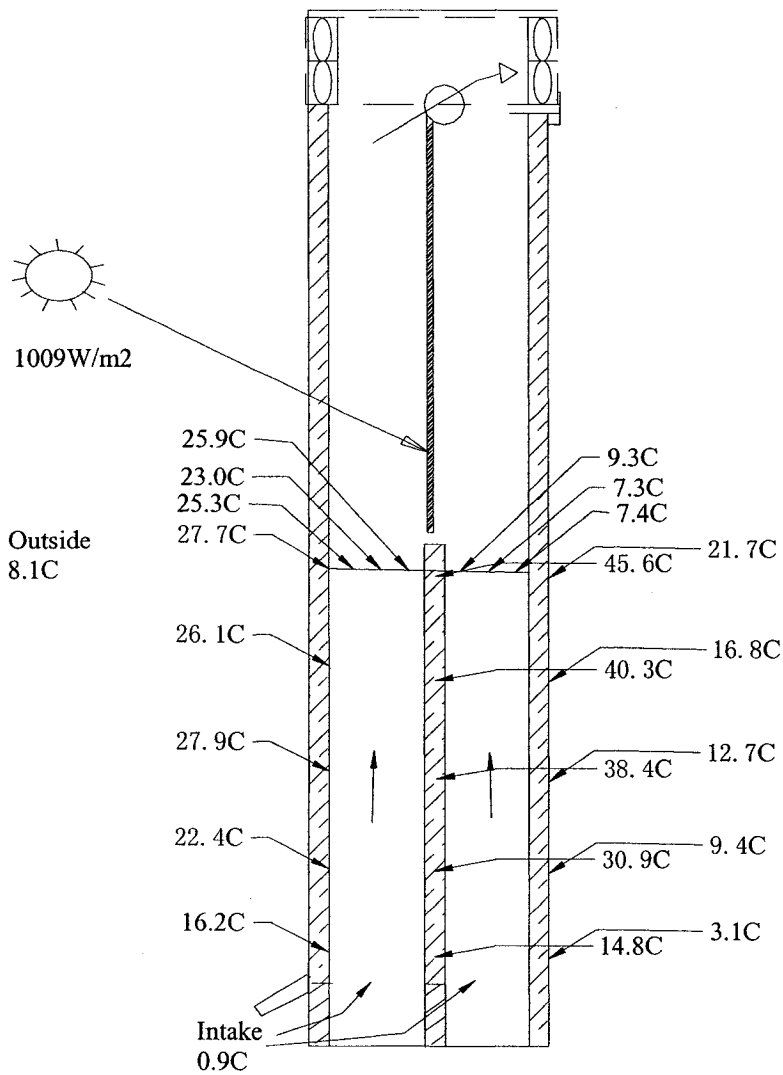

Figure 4.4 Experimental data of thermal performance for configuration 2 (Spheral solar side)

4.4 PIV Investigation

Particle Image Velocimetry (PIV) is employed to investigate the air flow dynamics inside the cavity. As discussed in Chapter 2, the PIV measurement has the advantages of whole-filed measurement, non intrusive of the flow field, and instantaneous measurement of the whole flow domain. These properties make it feasible to investigate the air dynamics and flow patterns inside the cavity.

PIV instrument is mounted both for Configuration 1 (Photowatt side) and Configuration 2 (Spheral solar side). A laser with intensive lighting wavelength of 532nm is used for the lighting source. Model Newwave Solo from New Wave Company is employed. A CCD-chip of 7.4μm×7.4μm from Dantec Company is utilized with the corporation of 105mm AF MICRO NIKKOR lens. Special filter for this specified wavelength is applied to sweep the background noise light. The camera is mounted parallel to the top surface of the air flow cavity to measure the outlet air velocity profile. The Configuration of the mounting is shown in Figure 4.5.

Fist, the seeding particles are scattered and suspended in the flow of interest. Then a 2-D plane of the flow is illuminated with the laser and a camera placed perpendicular to the light sheet records scattered light from the seeding particles. A pair of light pulses freezes two consequent position fields, with time t apart. The displacement vector between successive images of the same seeding particle is then calculated by:

$$\vec{d} = M \cdot \vec{v} \cdot t \qquad (4.9)$$

where $\vec{v}$ is the local velocity vector, and M is the object image scale factor.

Image maps are sub-divided into small regions (interrogation areas) and spatially correlated to determine the local seeding particle displacement. The local velocity is finally determined from the equation (4.9) above. It is suggested that for the flow of 10% turbulence, at least 100 vector maps need to be acquired to achieve 1% accuracy (Dantec Dynamics website www.dantecdynamics.com).

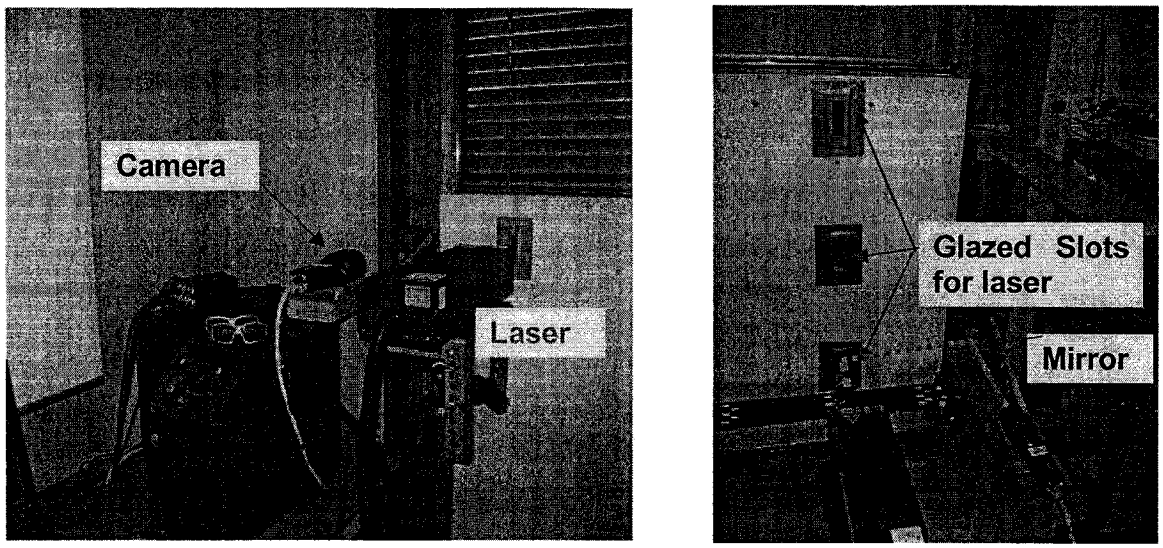

Figure 4.5 Facility mounting of the PIV instrument in Concordia test room

Experimental results are shown in Figures 4.6 - 4.10. In Figure 4.6, the image shows the velocity vector domain for configuration 1 (Photowatt side) (measured on March 30th, 2005) and Figure 4.7 shows the velocity vector domain for configuration 2 (Spheral solar side) (measured on March 22nd, 2005). The length of the arrow stands for the velocity magnitude and direction shows the velocity direction. The reference velocity of 1m/s is shown at the left bottom corner of the graph. From the graph we can see the profile of the velocity at the top of the cavity and some turbulence vortex generation. Figure 4.8 and 4.9 show the PIV measurement for each cavity at different average air velocity. These results can be used to validate the numerical model and also can be applied to calculate the flow speed in the cavity. The images can be compared and show the turbulence intensity and wind effects on the flow domain. From PIV measurement, 10-15% turbulence intensity is measured for Configuration 1 (Photowatt side) and 10-20% is found at different positions for Configuration 2 (Spheral solar side). Detailed study of the flow pattern can be investigated using PIV. Figure 4.10 shows the PIV investigation of formation of boundary layer for configuration 1 (Photowatt side) (measured on March 10th, 2005). The reference velocity 0.5m/s shows at the left bottom corner of the image. This near wall measurement of air velocity is of great value for validation of future detailed numerical studies.

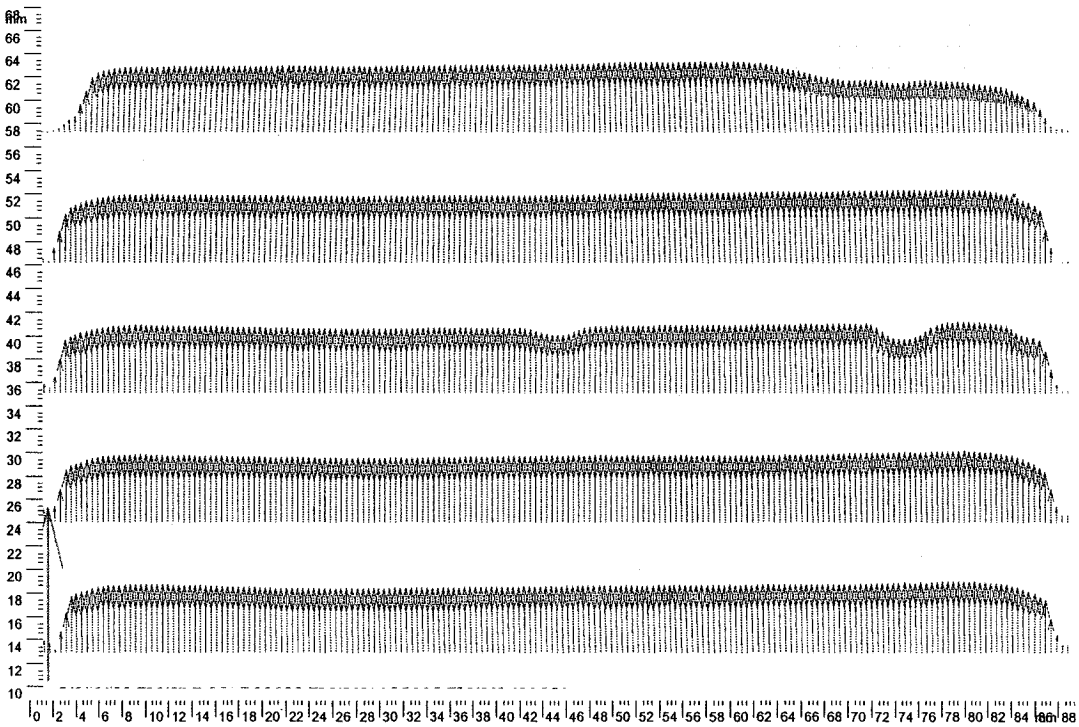

Figure 4.6 PIV test velocity vectors image for configuration 1 (Photowatt side)

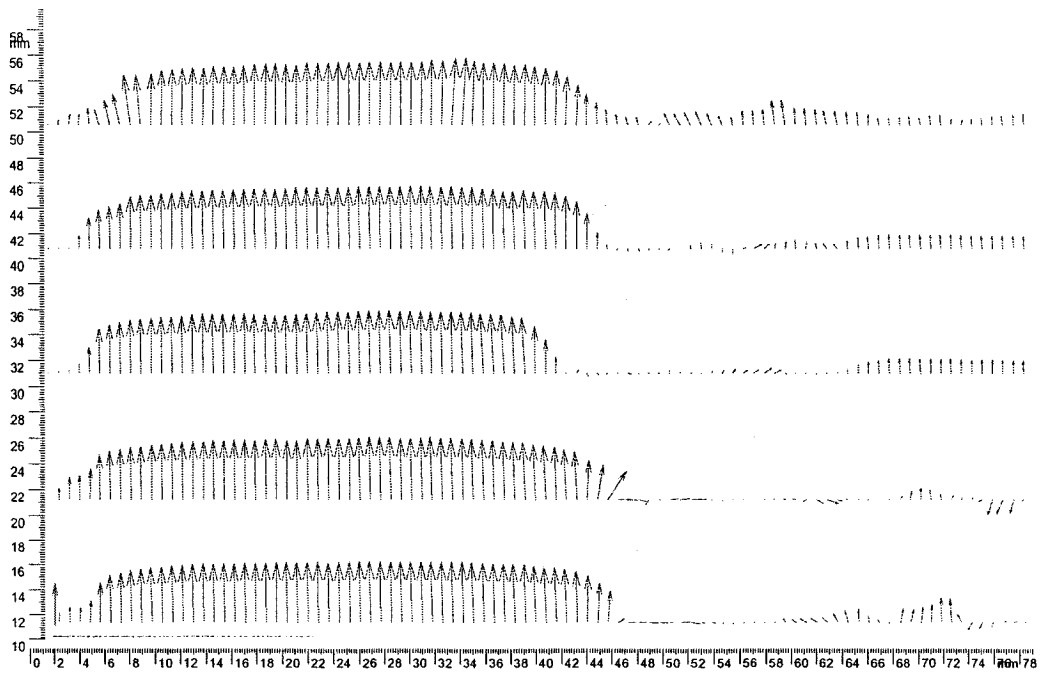

Figure 4.7 PIV test velocity vectors image for configuration 2 (Spheral solar side)

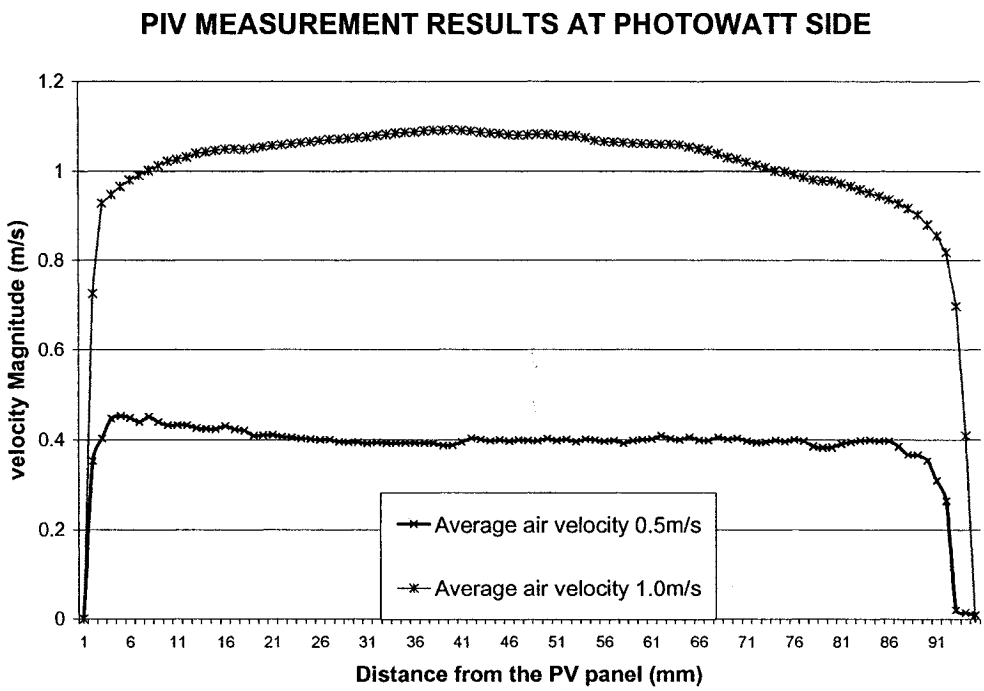

Figure 4.8 PIV measurement of velocity profile for configuration 1 (Photowatt side)

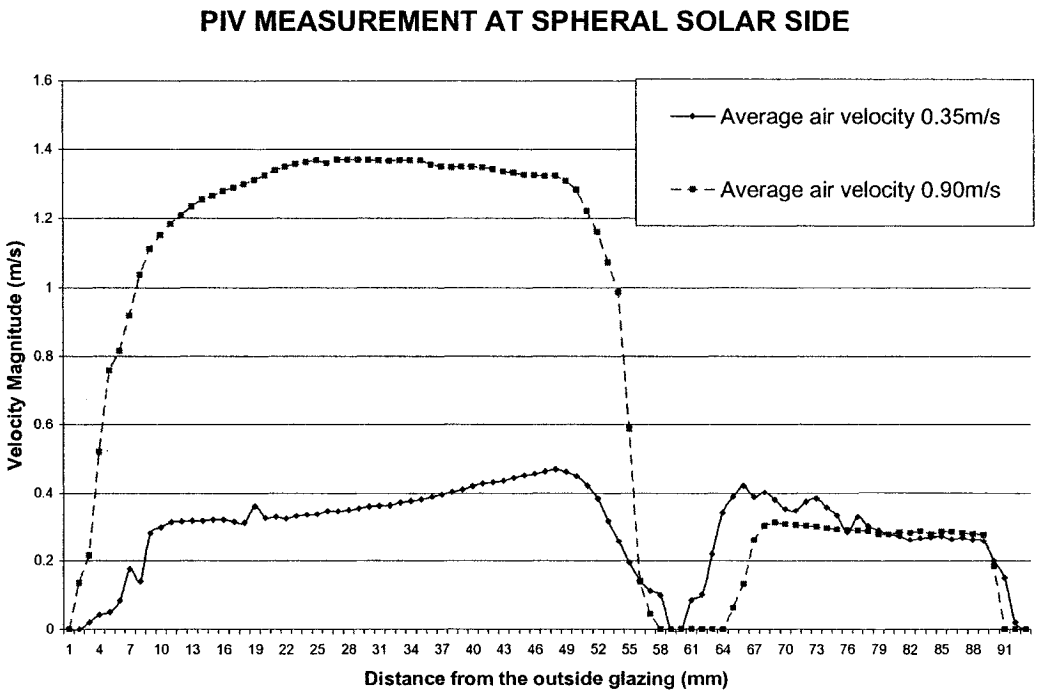

Figure 4.9 PIV measurement of velocity profile for configuration 2 (Spheral solar side)

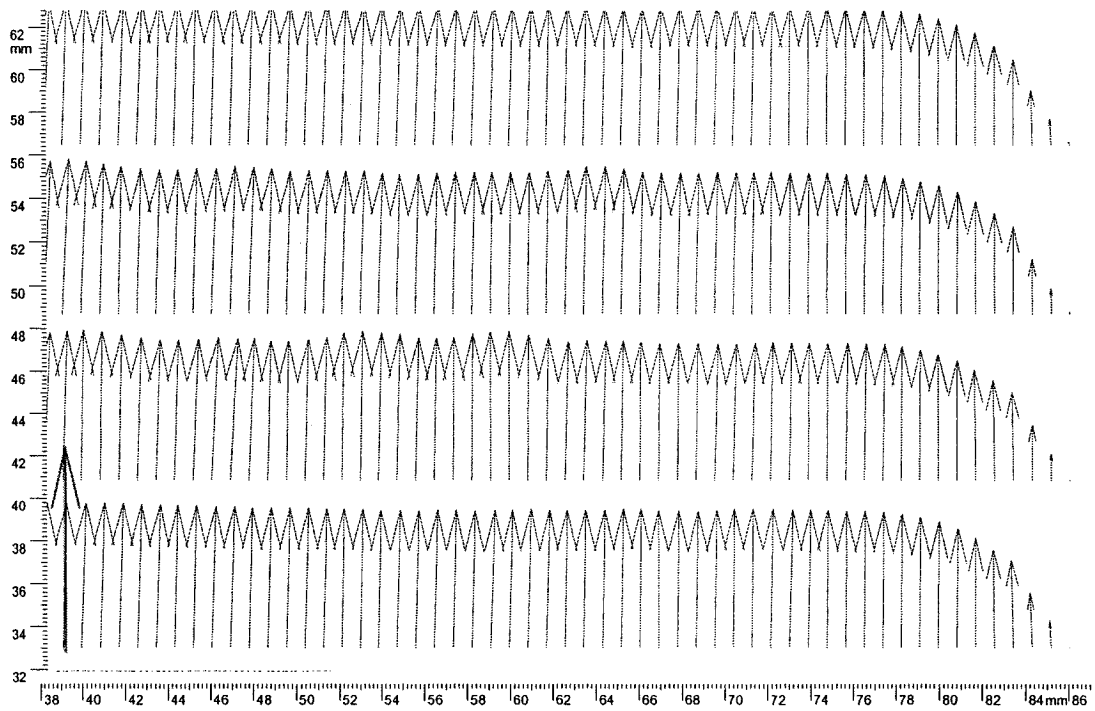

Figure 4.10 PIV investigation of velocity boundary layer for configuration 1 (Photowatt side)

By the favor of PIV technology, the inlet flow region can be firstly investigated. The turbulence and uncertainty of the inlet flow region can be thus clearly seen from the vector images and further studies can be carried on. Investigation results on April 14th, 2005 are shown as Figure 4.11 and 4.12. In Figure 4.11, the air enters the BIPV system cavity under the fan frequency 15Hz, and has an average air speed 0.5 m/s (the reference velocity shows at the left bottom corner with 1m/s magnitude). While in Figure 4.12, the air enters the cavity with the fan frequency 30Hz and average air speed 1.0 m/s accordingly. Since the laser cannot directly shoot at the inlet, the region just above the cavity inlet is inspected. It is easy to see the turbulence generation at the inlet region. At average air speed 0.5 m/s, the small vortex appears at the top of inlet and attached to the inlet side. Some minor backflow can be examined near the PV panel and may go out of the entrance. While in Figure 4.12 the vortex appears much more obvious. The turbulence vortex becomes dominant at the inlet region and vortex increases from the near wall region to the whole width of the cavity. The flow near the PV panel goes backwards with the speed 0.5 m/s and will exhaust outside. This counter flow will complicate the flow region inside the cavity and reduce the thermal efficiency. Therefore, high flow speed is not recommended in this BIPV thermal system.

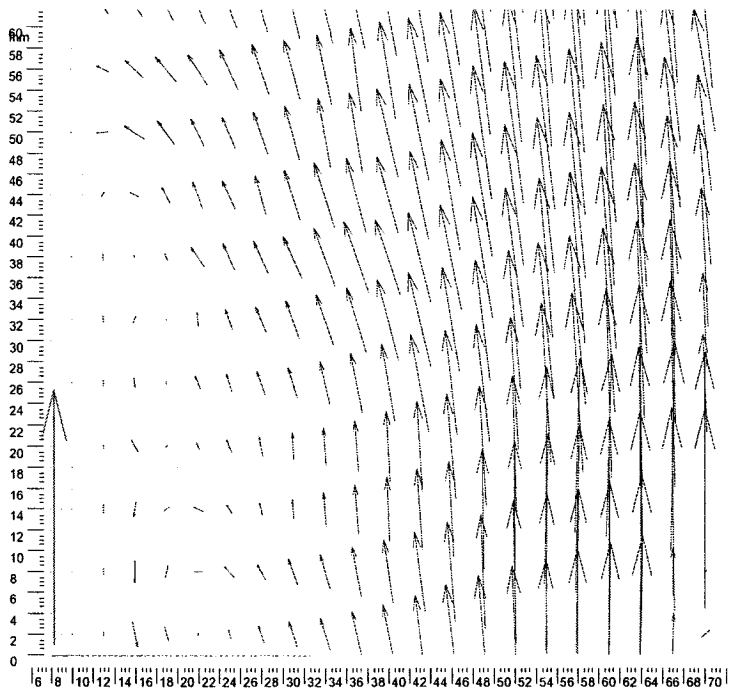

Figure 4.11 PIV investigation of velocity domain at inlet region for average inflow velocity 0.5m/s

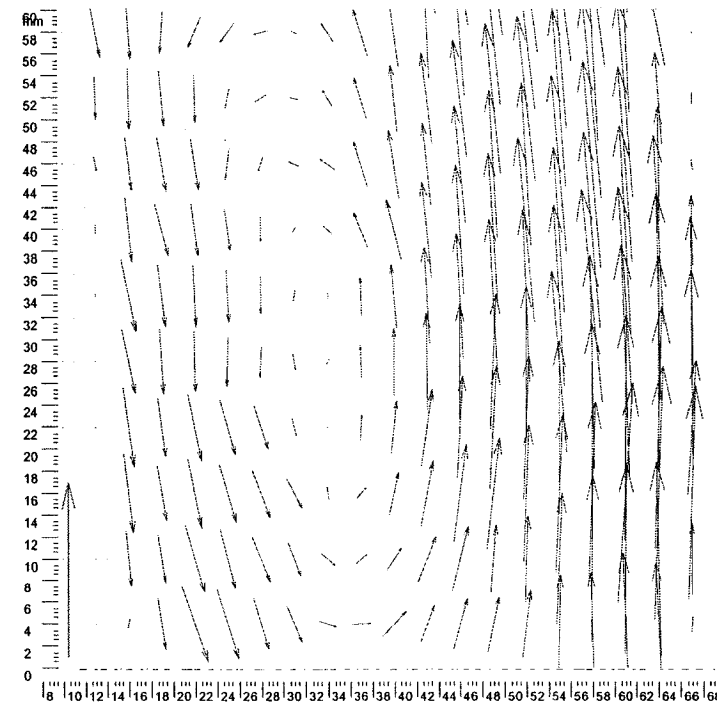

Figure 4.12 PIV investigation of velocity domain at inlet region for average inflow velocity 1.0m/s

4.5 Painting Effect & Reflection Effect

To further improve the thermal performance and electrical performance of BIPV thermal system, some experimental tests are investigated. In this section two different improvement tests of the BIPV system are presented and discussed.

As we know the PV panel acts as the key part of the BIPV system; it absorbs the solar radiation, generates heat and electricity, and transfers the heat to the air passing by. Therefore one thought to optimize the BIPV/T system is that we can put some fins on the PV panel so as to increase the heat transfer coefficient between the PV panel and the air. This approach however, has to make sure the fins have well conductance with the PV panel and effects of the fins are not easy to model. Here in this section, two quick methods are used to improve the system performance. Since the spheral solar panel had shiny Aluminum backing, one idea is to paint the back of the PV panel black. By doing this, the emissivity of the back of the PV panel increases from 0.5 to 0.95, and thus the radiative heat transfer between the PV panel and insulation is enhanced. This will indirectly increase the heat transferred to the air flow, because the radiation heat emitted from PV to the insulation is going to transfer to the air flow by convection. Table 4.3 shows the painting effects on the PV panel. The left PV panel is painted black and right panel left unpainted so as to make comparison. From the table we can read that the average temperature of the left PV panel is 2.5-3.5°C less than the right panel with the solar radiation around 700W/m^2. The average temperature difference could be even higher when the solar radiation reaches 1000W/m^2. If the temperature could be reduced by 5°C by this painting effect, we can roughly calculate that the electrical efficiency of the PV panel can increases by 2%-2.5%.

Table 4.3 Experimental data of painting effects on the PV panel

Date (2003)	S. R. (W/m^2)	To (°C)	Tr (°C)	Tsph_left_mid (°C)	Tsph_right_mid (°C)	Tsph_left_top (°C)	Tsph_right_top (°C)
Mar.11	720	9.2	21.5	47.2	50.1	52.2	54.0
Mar.12	683.3	8.6	21.5	45.0	48.6	50.7	52.8
Mar.13	749.4	-4.4	12.8	37.2	39.6	41.9	43.6

Another method to improve the performance of the BIPV performance is to increase the solar radiation absorbed by the PV panel by putting some reflection material below the PV panel. For the BIPV system, this could be the top of the inlet damper. Experimental investigation is carried on to examine this reflection effect. Results are shown as Table 4.4. By putting the reflector, the solar radiation ratio of increase reaches 9.5% for Configuration 2 (Spheral solar side) and 13.1% for Configuration 1 (Photowatt side). Since the solar radiation is proportional to the electrical performance, the electrical efficiency then can increase by 1%-1.5% by adding the reflection material.

Table 4.4 Experimental investigation of reflection effect

Time	Power & position	Without reflec.	With reflec.	Ratio of increase
11:00AM	P_sph	37.48	40.63	8.4%
	P_w	52.28	58.85	12.6%
12:00PM	P_sph	37.16	40.70	9.5%
	P_pw	52.04	58.88	13.1%

4.6 Conclusion

In this chapter, the test facilities for this project are introduced and experimental data are analyzed. Due to the complexity of the BIPV system, various meters are employed to look into the thermal performance and electrical performance of the system. Experimental equipment is listed in this section with the model name and most important specification. The mounting of the thermal couples is then pictured and the measurement results are shown for both Configuration 1 (Photowatt side) and Configuration 2 (Spheral solar side). Data are analyzed and system efficiency, thermal efficiency and electrical efficiency are calculated. The total system efficiency for configuration 1 (Photowatt side) can reach 62.1% while for configuration 2 (Spheral solar side) it can reach 78% because of the air flow on both sides for configuration 2 (Spheral solar side). PIV instrument is utilized to explore the air flow dynamics inside the cavity. Detailed PIV investigation pictures of the velocity vectors are presented for both sides.

Also, the formation of the boundary layer and inlet region is discussed using the PIV investigation results. The vortex at the inlet region is interesting to inspect and of great value for future research. Some other improvement methods are then tested with experimental results. Black color painting on the back of Spheral solar PV panel can result in increasing the electrical efficiency up to 2-2.5% and putting reflection materials at the bottom of PV panel can increase the PV electrical efficiency by 1-1.5%.

Chapter 5

CFD MODELING RESULTS

5.1 Introduction

In this Chapter, the CFD modeling results are presented. Various flow parameters are tested and heat transfer rates are summarized. Detailed profiles of the temperature and velocity at the outlet of the air flow cavity are also plotted. These detailed profiles are helpful to understand and further study the flow dynamics characters and thermal behavior of the air flow cavity. Later, some other flow parameters are also studied, including the turbulence intensity, pressure loss distribution. At the last section, convective heat transfer coefficients are generated. The average convective heat transfer coefficients are provided with different average air speed, and then the correlations of the convective heat transfer coefficients according to channel height and average air velocity are given. To predict the local PV temperature, the profile of the convective heat transfer coefficients are generated and is later validated in the validation chapter. Since this convective heat transfer profile can be used to calculate the local heat transfer rate at any position, the predicted PV temperatures are more accurate and similar to the experimental results.

5.2 Heat Transfer Analysis

In the BIPV thermal system, the PV panel acts as a heat source. It absorbs the solar radiation and generates electricity and heat. Part of the heat is lost to the outside by natural convection and longwave radiation, while another part of the heat is captured by the air flow and could be used immediately or later according to the demand if stored. Thus the PV panel and air flow channel make up the main components of BIPV thermal system. Since the PV panel's electrical efficiency is linked with the temperature of the PV cells, how much heat can be taken away by the air flow is thus important to know to predict the performance of the PV panel.

Typically, two paths of heat transfer from the PV panel to the air flow are investigated in this air flow channel. One is by convection, either natural convection or forced convection. When the air flow passes the PV panel, as long as there is temperature difference between the PV panel and air, the convection heat transfer will take place and the PV panel transfers heat to the air flow. This convection heat transfer could be enhanced by increasing the air velocity or putting some fins attached to the PV panel. The other path is indirect but still significant. When the PV panel is heated by the solar radiation, experimental investigation shows the temperature could reach 300K-310K in the winter and 320-330K in the summer. The longwave radiation from the PV panel is thus activated greatly. Some quick estimation using the mean temperature of the PV and insulation can give the radiative heat transfer hr equal to 5-8 W/m^2K approximately. Therefore, the PV panel emits a big amount of energy by irradiation and heats the insulation at the other side of the channel. The insulation is heated and transfers the energy to the air by convection. Thus the longwave radiation from the PV panel activates the convection on the other side of the cavity. Heat is finally transferred from the PV panel to the air flow in this indirect approach. This radiative heat transfer from the PV, also the convective heat transfer from the insulation, could be enhanced by increasing the PV temperature or increasing the emissivity of the PV panel, but may not vary much when increasing the flow speed.

This convective and radiative combined heat transfer problem is studied for various air velocities and results are summarized as table 5.1. The non-uniform temperature profile of height is assigned to the PV panel and ambient conditions with intake temperature 0 °C are specified for this comparison. These cases are set according to the winter condition with the ambient condition around 0 °C and the PV average temperature around 30 °C.

Table 5.1 Summary of heat fluxes for various air velocity

Average air speed (m/s)	Total heat flux from PV (W/m^2)	Convective heat flux form PV (W/m^2)	Radiative heat flux from PV (W/m^2)	Convective heat flux from insulation (W/m^2)
0.5	293	200	93	86

0.7	330	230	100	93
1	406	295	111	103
1.25	462	346	116	107
1.5	510	390	120	111

From table 5.1 we can observe the effects of different air velocities on the thermal performance of the BIPV system. From the correlation in Figure 5.1, we can see that the convective heat transfer is enhanced almost linearly by increasing the flow speed. On the other hand, the radiative heat transfer from the PV and the convective heat transfer from the insulation are relatively stable. It is interesting to note here the convective heat transfer from the insulation is barely dependent on the air flow speed, for reasons which are discussed above in the heat transfer analysis. Thus the total heat transfer is increasing parallel to the convective heat transfer. However, the real experiment could be more complex because the boundary layer temperature is also coupled with the average air speed. When the average air speed is increased, stronger heat transfer would take away more energy from the PV panel thus reduce the PV panel's temperature. To study this conjugate heat transfer, the convective heat transfer coefficients will later be generated and can be put into Charron&Athienitis' 2-D thermal model to calculate more accurate heat transfer considering these coupled relations.

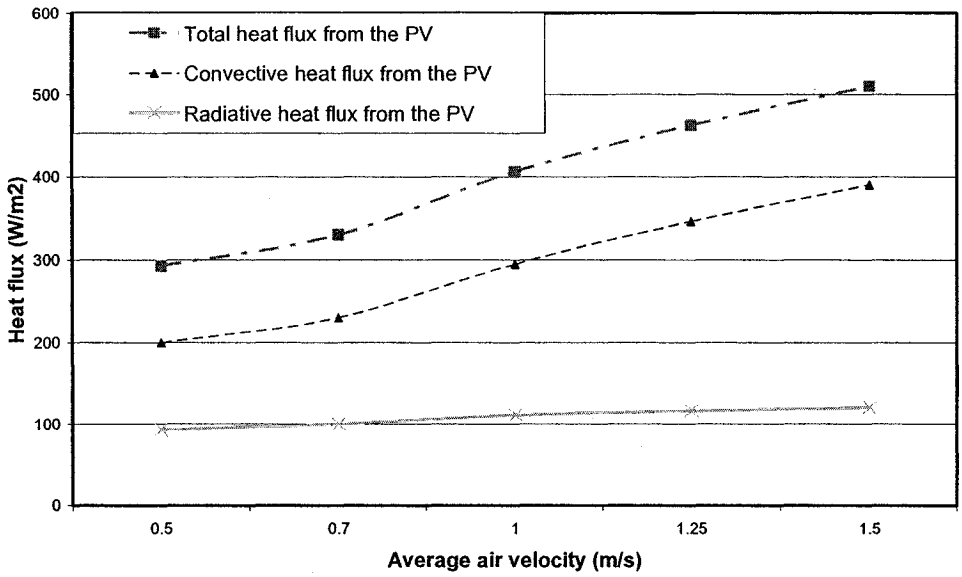

Figure 5.1 Correlation of heat flux for different air velocities for Configuration 1

5.3 Modeling Results of Temperature Profile

Since PV panel is only 1 meter high, this distance is not enough for the air flow to become fully developed. The airflow in this BIPV system is still in the developing region. So it is interesting to examine how this air flow is developed and how much heat has been taken to the air at different heights. Thus the temperature profile would be the best detailed point to check the thermal behavior of the BIPV system. Also the temperature profile could be compared with experimental data and used as a validation method for the CFD modeling.

The temperature profile is presented below in Figure 5.2. This case is designed for winter condition. The air flow enters the cavity with intake temperature 0 °C under pressure difference 0.5 Pa and maintains the average air speed to 0.5 m/s. The left surface is PV panel with non-uniform specified temperature according to the experimental data. The right surface is set as adiabatic boundary. The temperature profile is examined for four different heights, 0.25 meter, 0.50 meter, 0.75 meter and 1 meter high.

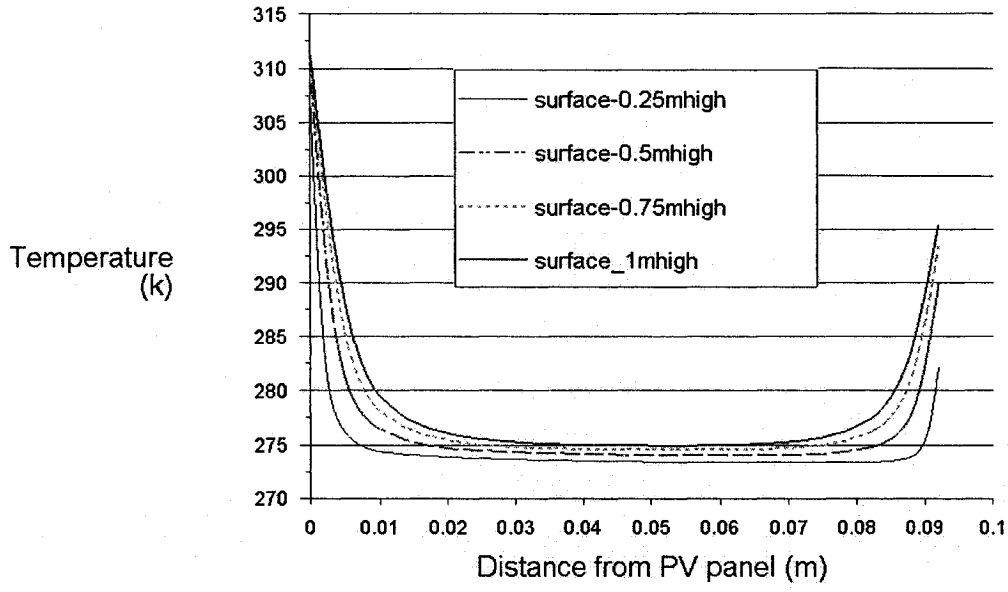

Figure 5.2 Temperature profiles at various height of the cavity for average air speed 0.5 m/s

From the temperature profile graph we can observe that the temperature falls sharply in the left thermal boundary layer from 37 °C to about 4-6 °C and then remains flat in the inflow region until the other thermal boundary layer near the insulation. As the air flow goes at higher position, the air gradually heated by the PV panel and the temperature profile moves upwards. In addition the flow pattern also changes according to heights. As we can see from the temperature profile, the thermal boundary layer is becoming thicker when the air flow moves up and also the air flow becomes more developed. Another point to draw attentions here is the temperature increasing at the insulation side. Since there is negligible heat flux through the insulation, the convection heat transfer should equal the net radiation heat transfer. The radiation heat emitted from the PV panel is thus transferred to the air by convection. Therefore, the convection heat transfer from the insulation is not only determined by the flow dynamics but also can be influenced by the PV and insulation surface radiative properties.

5.4 Modeling Results of Velocity Profile

For the same significance to examine the temperature profile, the velocity profile is also

important for understanding and studying the air flow dynamics and thermal performance inside the cavity. From the velocity profile, the development of the flow in this developing region can be clearly observed. Also the velocity profile is another key parameter to check the validity of the CFD model.

In the momentum conservation equation, the velocity is coupled with the temperature by the buoyancy term and also linked to the pressure difference. Due to the complexity of the governing equations, these equations cannot be solved using any analytical method. The numerical approach seems the only way to examine the velocity profile inside the air flow cavity. In many cases the velocity profile has become the criterion to compare and validate different CFD models.

In Figure 5.3 velocity profiles at different heights for the average air flow speed 0.5 m/s are presented. This case is designed for winter condition. The air flow enters the cavity with intake temperature 0 °C under pressure difference 0.5 Pa and maintains the average air speed to around 0.5 m/s. The left surface is PV panel with non-uniform specified temperature according to the experimental data. The right surface is set as adiabatic boundary. The velocity profile is examined for four different heights, 0.25 meter, 0.50 meter, 0.75 meter and 1 meter high.

From the velocity profile we can observe that the flow pattern has undergone a large difference from the inlet to the 1 meter high top of the cavity. At the inlet region, when the air enters into the cavity under the pressure difference, the flow is forced to make a 90° turn and thus the air flow blows with higher speed at the insulation side but with little speed at the PV panel side. Some vortex could be generated at the PV panel side in the inlet region. As the flow goes upwards, the hot PV panel heats the nearby air and thus accelerates the airflow by stack effect (buoyancy effect). On the other side, the flow speed is reduced by the friction near the insulation region. Therefore, at 1 meter high, the typical velocity profile is formed with a buoyancy induced peak near the PV panel and a long flat region at the center, which is the characteristic shape of the turbulent flow.

Figure 5.4 presents the velocity profiles for different average air velocities. It is interesting to note that as the average air speed increases, the velocity profile becomes developed. The buoyancy-induced peak at the average air speed 0.5 m/s disappears, and another minor peak appears near the insulation side at the average air speed 1.5 m/s. However, this minor change of the flow pattern reveals the significant fact that the flow is changing from the combined natural and forced convection to mainly forced convection. At the average air speed 0.5 m/s, the pressure difference is about 0.5 Pa. This small pressure difference is not significant and is comparable to the pressure difference caused by the stack effect. Therefore, the buoyancy force near the PV panel is strong enough to influence the flow pattern. However, when the average air speed increases to 1.5 m/s, the pressure difference increases to around 4.0 Pa. This pressure difference is thus dominant in the air flow cavity and the stack effect becomes negligible.

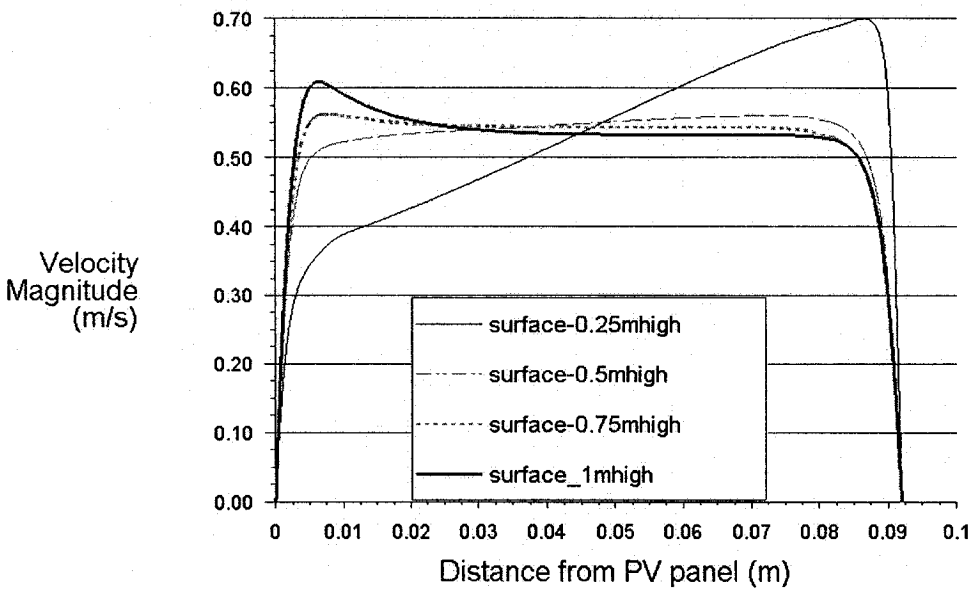

Figure 5.3 Velocity profile at different heights for average air speed 0.5m/s

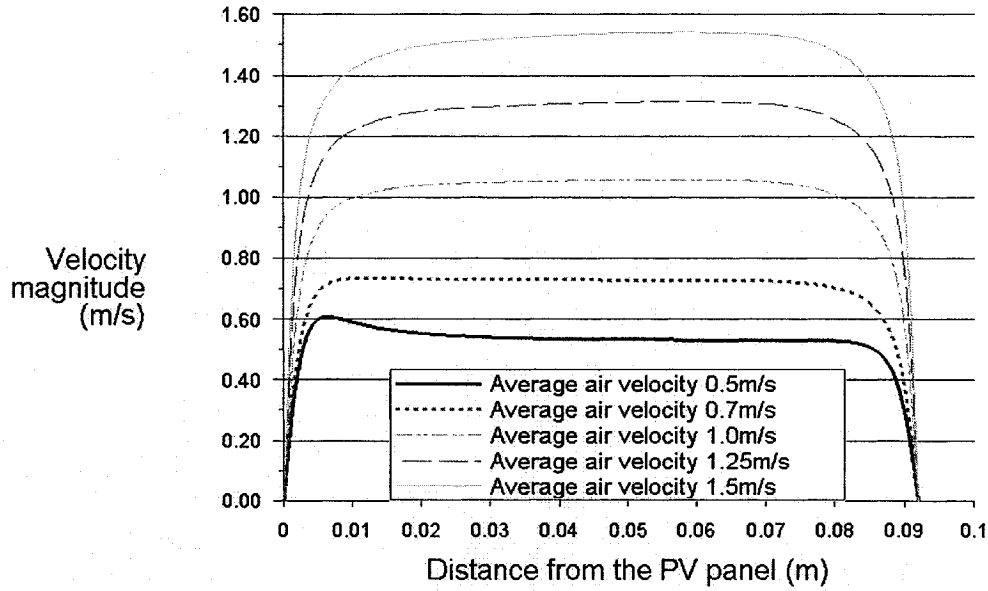

Figure 5.4 Velocity profiles under various average air velocities

5.5 Modeling Results of Other Profiles

Temperature profile and velocity profile are presented in previous sections. Some other profiles such as the turbulence intensity and pressure loss distribution are also important for understanding the flowing dynamics and further studying the thermal performance inside the cavity. In this section, these profiles are plotted and analyzed.

In Figure 5.5, the turbulence intensity graph is presented for different heights inside the cavity. As the same as the previous cases, the winter condition is assigned to this study. The airflow enters into the cavity with 0 °C under the pressure difference 0.5 Pa and maintains the average air speed to around 0.5 m/s. The left surface is PV panel with non-uniform specified temperature according to the experimental data. The right surface is set as adiabatic boundary. The turbulence intensity profile is examined for four different heights, 0.25 meter, 0.50 meter, 0.75 meter and 1 meter high.

From the graph 5.5 we can see that the turbulence intensity is reducing as the flow goes up and develops. At a height of 0.25 meter, the profile shows the peak turbulence intensity at the center about 33%, while at the height of 1 meter this peak turbulence intensity declines to 6%. Another interesting change happens when the profile develops from the 0.25 meter height to 0.50 meter height. The turbulence intensity of 0.50 meter height almost shrinks to one third of the former one. This sudden change of the turbulence intensity can be explained by the 90° turning in the inlet region, where the flow is forced to change the direction and thus a big amount of turbulence is created.

Turbulence intensity profile is also studied for various air velocities and is shown in Figure 5.6. The turbulence intensity is developing when the flow speed increases. When the average air speed is as low as 0.5 m/s, the peak turbulence intensity at the center is only 6%. When the average air speed increases to 1.5 m/s, the turbulence intensity peaks at the insulation side with the value of 14%. The turbulence profile becomes more and more developed as the flow speed increases. At the average air speed 1.5 m/s, typical turbulence intensity profile is generated with peaks at two boundary side and main flat region in the center.

The pressure drop study is critical for the control strategy. The pressure distribution is simulated for different air velocities and plotted in Figure 5.7. The same boundary condition is used for different cases, in which non-uniform specified temperature at the left surface and adiabatic surface on the right are used. Since the large turbulence intensity at the inlet region, the pressure distribution becomes irregular in the inlet region.

From the graph 5.7, we can notice that pressure drop in the main flow region is not obvious. The biggest part of the pressure drop just happen in the inlet region, where the 90° turning forces the flow to change direction. Another interesting point can be observed from this graph that the pressure is increasing with height when the flow speed is low and decreasing when the flow speed is high. This is also due to the buoyancy effect. At low flow speed, the buoyancy effect acts as the part of the source to accelerate the flow and that is why the static pressure can be increased along the path. However, when the higher fan power increases the flow speed

in the cavity, the forced flow becomes dominant. Thus the pressure is dropping due to the friction at the wall.

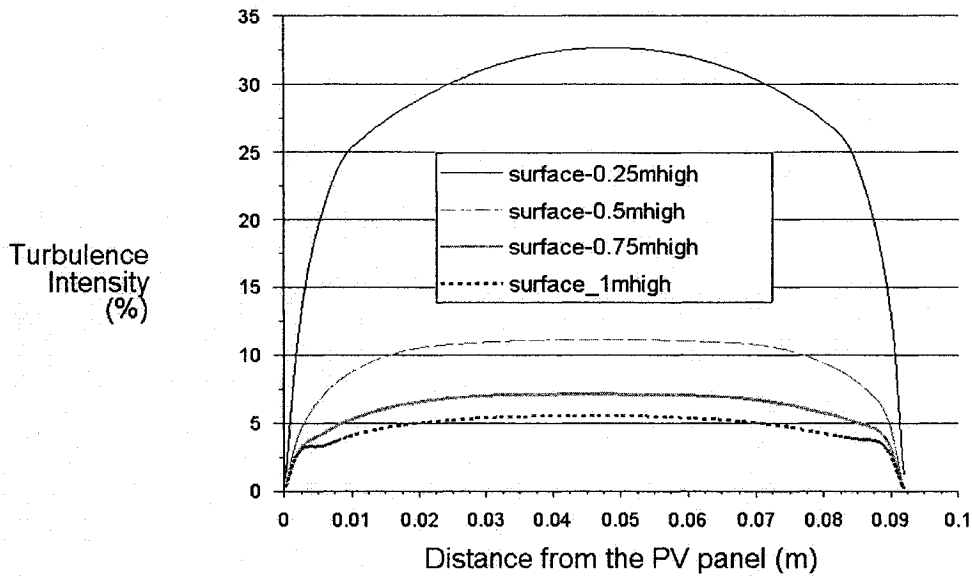

Figure 5.5 Turbulence intensity graph at different heights

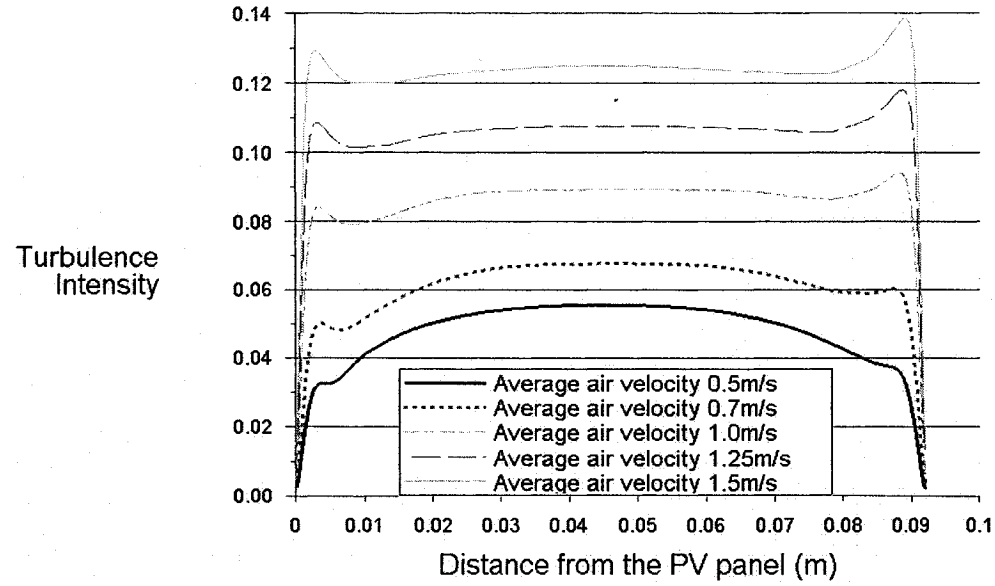

Figure 5.6 Turbulence intensity profile for various air velocities

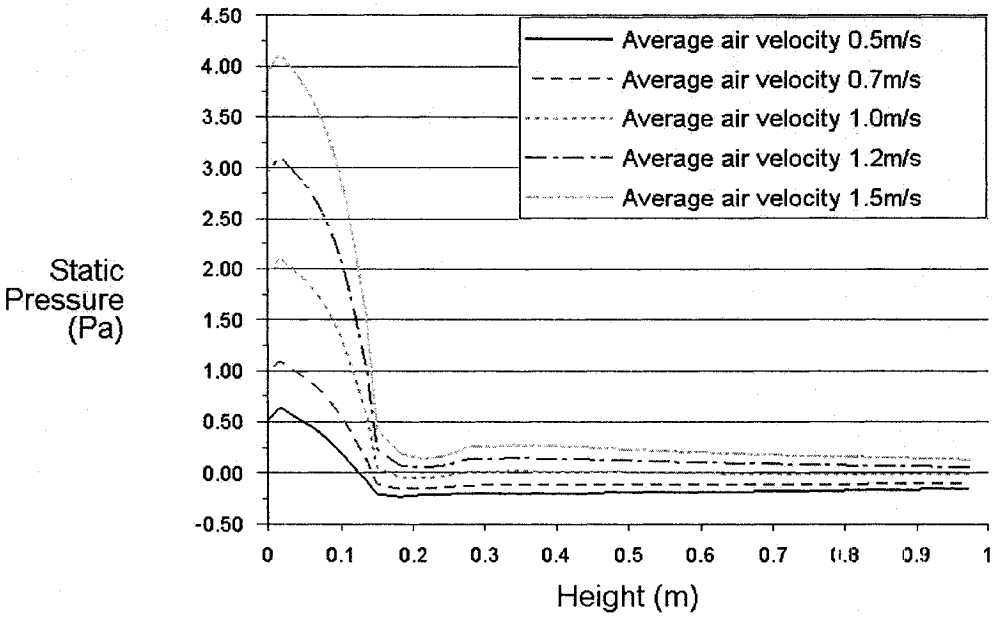

Figure 5.7 Pressure distribution for different average air velocities

5.6 Study of the inlet region

Generally the complexity of the inlet region often gives trouble to the CFD modeling and

system heat transfer analysis. In addition, some bad assumption of the inlet region can even cause the final modeling results away from the physical reality. The modeling of the inlet is thus almost critical for the whole CFD model to get accurate results, especially when the flow is in the developing region. Some flow vectors simulation of the inlet region is plotted in this section and qualitative analysis is discussed.

To take the common case as the example, the winter condition with the ambient temperature 0 °C is studied. The pressure difference is around 0.5 Pa and average air speed is 0.5 m/s. The boundaries remain the same as the previous settings.

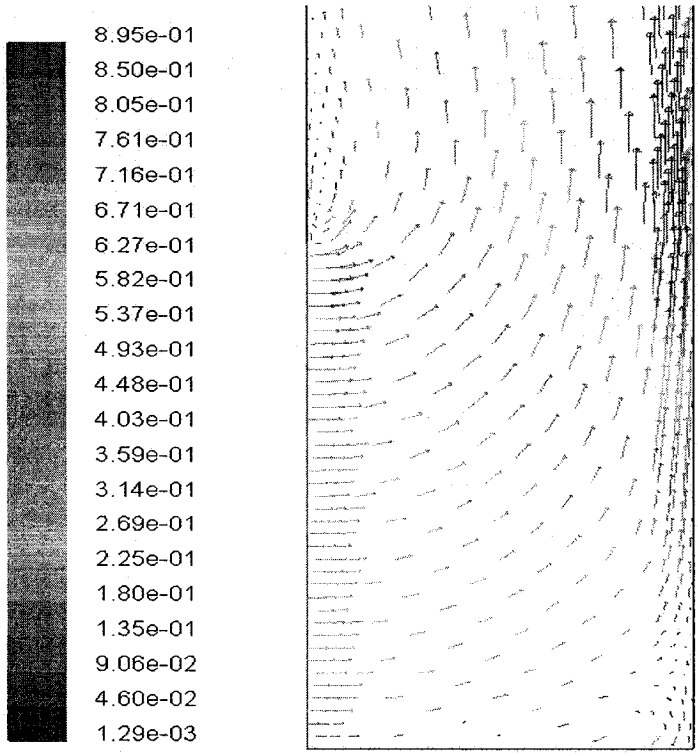

Figure 5.8 Vectors simulation result at the inlet region

The velocity vectors simulation result at the inlet region is presented in Figure 5.8. From the plot we can clearly discover the idea how the flow enters into the cavity and why the large turbulence is generated at the inlet region. The air enters into the cavity under the fan force and also some stack effect, and then it undergoes the 90° turning right afterwards. From the sizes and colors of the vector arrows we can discover that the velocity is much higher at the

insulation side than at the PV side due to the turning. Right above the inlet on the left side, vortex flow is generated and can be easily seen from this plot. This will explain why the convective heat transfer coefficients at the insulation side is higher than the PV panel side and also why the large turbulence intensity is generated. This effect could be reduced or removed by smoothing the inlet path. Some curved fins can be used to guide the flow and then reduce both the pressure loss and turbulence intensity.

5.7 Generation of Convective Heat Transfer Coefficients

After detailed study of the air flow dynamics and thermal behavior inside the cavity, the convective heat transfer coefficients for both the PV panel and insulation are generated in this section. The convective heat transfer coefficient profile is presented for various air velocities and a correlation of the average convective heat transfer coefficient is later generated for future use.

To start with the basic case, winter condition in Montreal is simulated. The boundary conditions are set according to the experimental data. The intake air temperature is set to 0 °C and average air speed 0.5 m/s. The PV temperature is specified using the curve fitting according to the measurement. The adiabatic surface is assigned as the right surface boundary. The modeling result for this case is presented in Figure 5.9. The profile starts from the top of the inlet so as to avoid the uncertainty of the inlet region.

Figure 5.9 shows the calculated (from CFD model) convective heat transfer coefficient profiles for the two main cavity surfaces: the PV surface and insulation. As expected, at the leading edge, which is just after the inlet, the convective heat transfer coefficient is quite high and that is also why the PV boundary temperature profile increases exponentially as expected (see Figure 3.2). In addition, although the buoyancy effect increases the heat transfer rate near the PV panel, the convective heat transfer coefficient at the insulation side is still higher. First, since the inlet is at the bottom left side, the air enters, then turns and has a significant velocity component towards the insulation surface. This can be seen from the velocity domain simulation of 2-D CFD model as shown in Figure 5.8. The velocity near the insulation is faster

than near the PV panel side, thus the convective heat transfer is stronger near this surface. Second, the insulation surface is further heated by the longwave radiation and because there is negligible heat flux through the insulation the insulation heats up and transfers the energy by convection to the air.

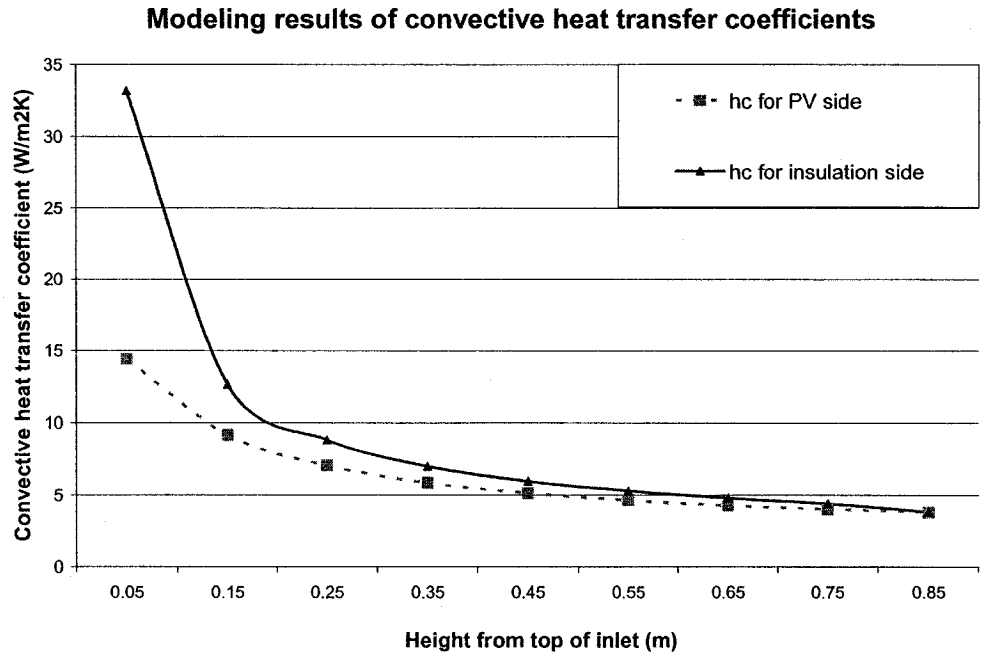

Figure 5.9 Convective heat transfer coefficient profile
at PV panel interior surface and at insulation

The convective heat transfer coefficients are also generated for different average air velocities. In Figure 5.10, convective heat transfer coefficients at the PV panel side is plotted and in Figure 5.11, the convective heat transfer coefficients at the insulation side is presented. When the flow speed is high, the convective heat transfer coefficient at the leading edge is quite high. For example, the convective heat transfer coefficient reaches 80 W/m^2K at the average air speed 1.5 m/s near the inlet region. The error between the numerical results and experimental data may be because of the uncertainty from the inlet region. The CFD model, which is based on some modeling assumptions, may not accurately predict the complex convective heat

transfer at the inlet region. That is also why CFD models always need experimental data to be validated. The validation studies are presented in the next chapter.

For future applications of modeling results, the average convective heat transfer coefficients and radiative heat transfer coefficients are summarized in table 5.2 and the correlation is generated and plotted in Figure 5.12. From the correlation graph, we can observe that the convective heat transfer coefficients are increasing step by step as the flow speed increases. In addition, the convective heat transfer coefficient at the insulation side has a higher decreasing gradient. This is mainly because the flow is coming from the left bottom (PV side) of the cavity and forms a blowing region at the leading edge of the insulation side.

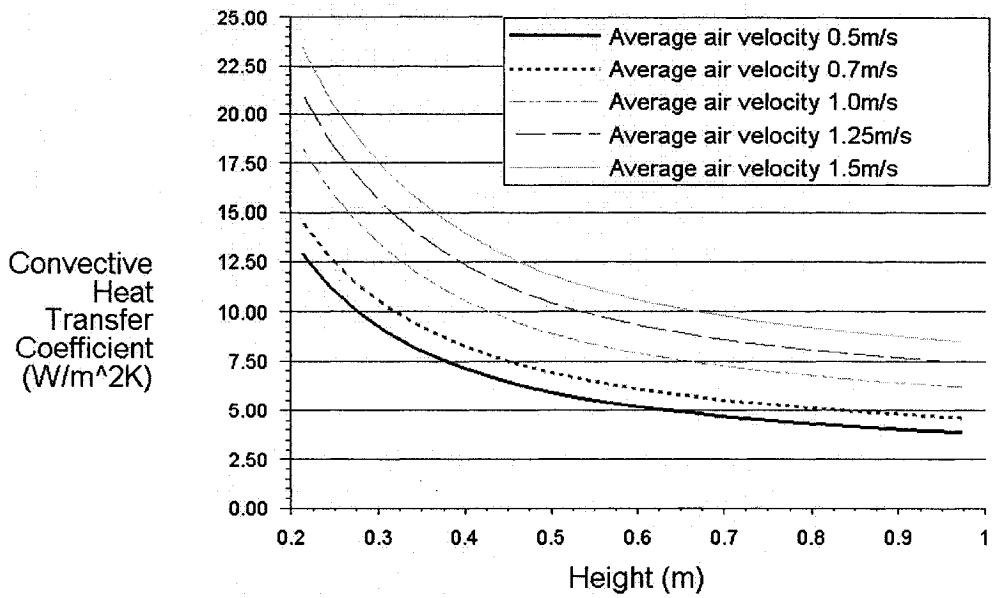

Figure 5.10 Convective heat transfer coefficient profiles for different air velocities at PV panel side

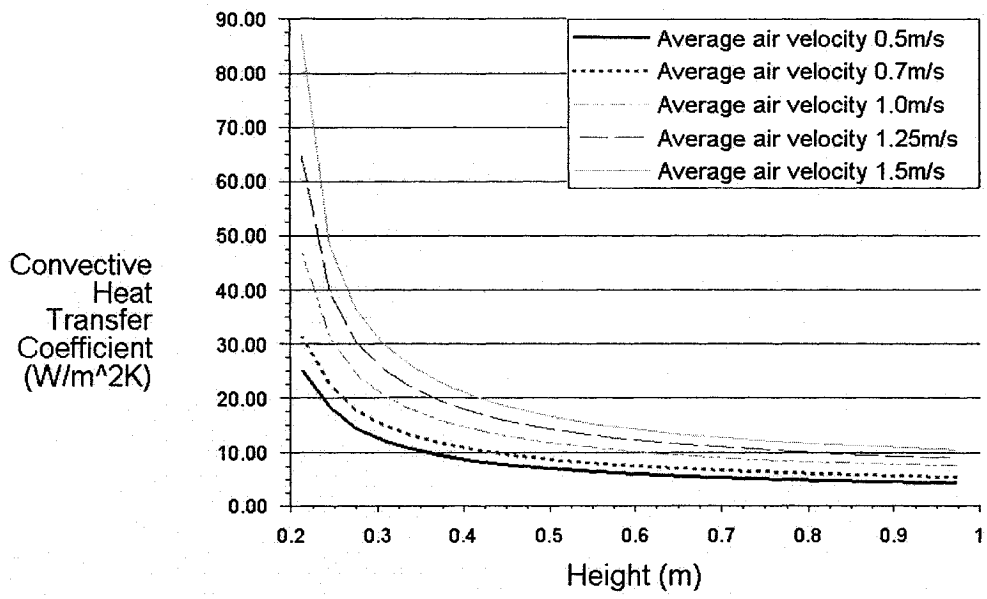

Figure 5.11 Convective heat transfer coefficient profiles for different air velocities at insulation side

Table 5.2 Summary of heat transfer coefficients in the air flow cavity

Air velocity (m/s)	Convective heat transfer coefficient for PV panel (W/m^2K)	Convective heat transfer coefficient for insulation (W/m^2K)	Radiative heat transfer coefficient (W/m^2K)
0.5	5.8	8.6	4.8
0.7	6.9	10.3	4.8
1.0	8.8	13.6	4.8
1.25	10.2	15.8	4.7
1.5	11.5	17.9	4.7

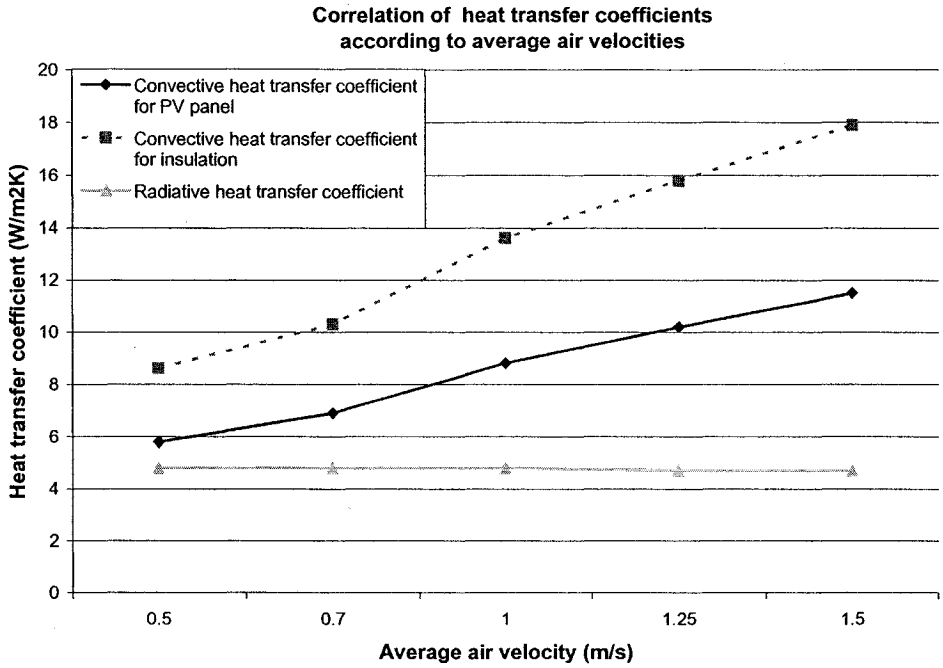

Figure 5.12 Correlation of heat transfer coefficients according to various air velocities

Two suggestions are made to optimize the convective heat transfer for PV panels in BIPV-thermal system. First, the Configuration of the BIPV system could be further improved. Since the convective heat transfer coefficients are higher at the inner (back) side of the cavity, it should be better to mount the PV panel at the inner side of the cavity. Then to make sure the PV panel can receives as much solar radiation as possible, the outer side will need to be mounted with clear glazing with high transmittance and low-e coating. The back side of the PV panel can be connected with another thin air flow cavity or directly attached to the phase change material (PCM) board so that the heat from the back of PV panel is also restored. Second, if the PV panel is needed to be mounted as the outer façade of the cavity for some reasons, some well-designed flow guiding fins can lead the flow more towards to the PV panel instead of the insulation. Also if the air is pCharronxed at the inlet damper with the returning air coming from the room, there will be more air passing near the PV panel so that the convective heat transfer coefficients at the PV side can be enhanced.

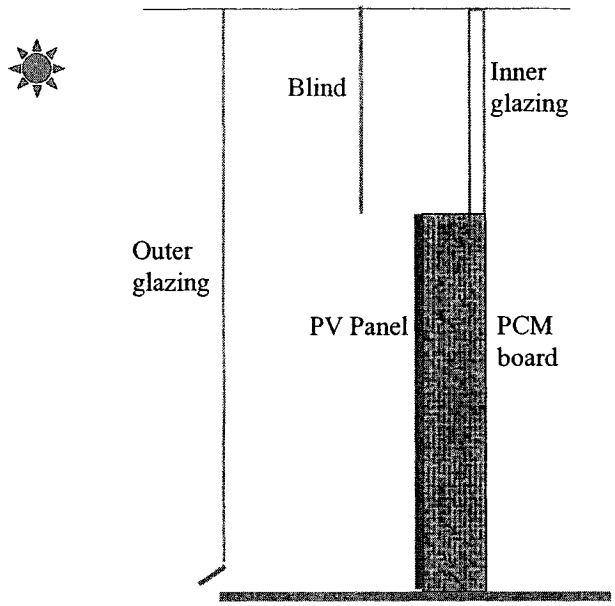

Figure 5.13 Suggestion of the Configuration of BIPV thermal system

Besides of the convective heat transfer coefficients, dimensionless form of the correlation of Nusselt number according to different Reynolds number is generated and can be used for later comparison with other models. The result is plotted in Figure 5.14. The characteristic length for the dimensionless numbers is set to the width of the cavity, which is 0.092 m. Other parameters are set according to the air properties at 0 °C. In Figure 5.14, a linear correlation is found for Nusselt number as a function of Reynolds number.

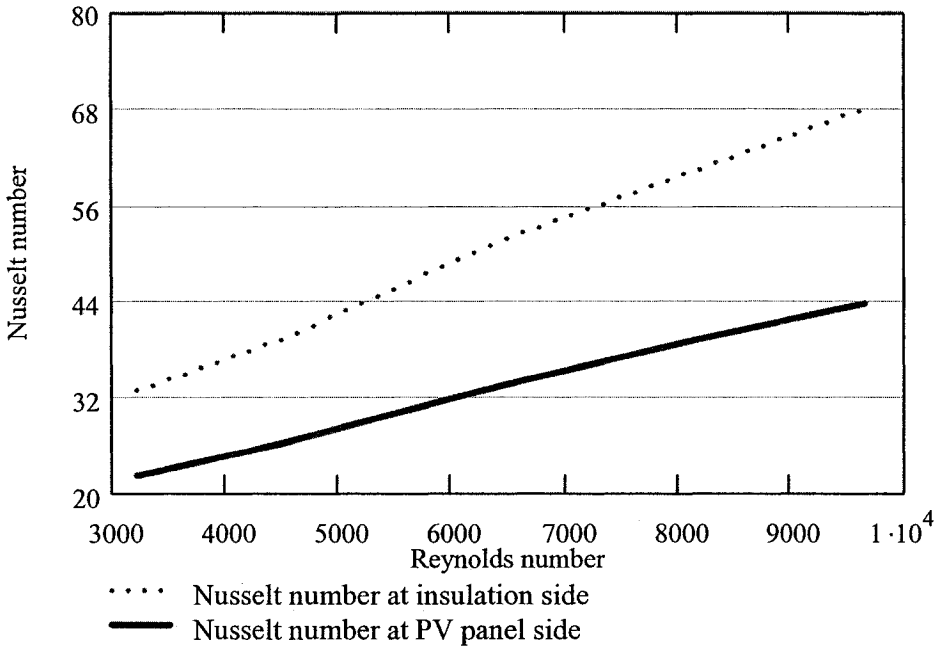

Figure 5.14 Dimensionless correlation for Configuration 1 (Photowatt side)

5.8 Correlation of Heat Transfer Coefficients

To be able to integrate into Charron&Athienitis' 2-D model and also for future applications, the profiles of convective heat transfer coefficients are put into some mathematic formulations. These correlations can be quickly used in any software or program to calculate the local convective heat transfer coefficient at certain position and thus the heat transfer rate could be easily generated. In this section, mathematic methods are employed to generate this correlation of the convective heat transfer coefficients with channel height and flow speed.

From the shape of the profile plotted in Figure 5.10 and 5.11, we can observe that the convective heat transfer coefficients points fall into the exponential correlation with channel height. Thus the typical exponential correlation ($h_c = a \cdot e^{b \cdot h} + c$) is used here for regression. Since the coefficients of this exponential correlation are also the function of average air speed. Double-regression has to be made to generate the proper function for both the height and average air speed.

After mathematical procession, the correlation functions of convective heat transfer coefficients according to the channel height and average air speed are generated.

The regressed correlation at the PV panel side is as follows:

$$h_c = 36.3 \cdot e^{(2.042 \cdot \overline{V} - 7.375)h} + 3.987 \cdot \overline{V} + 2.127 \quad (5.1)$$

The regressed correlation at the insulation side is given by:

$$h_c = \left(184.946 \cdot \overline{V} - 32.715\right) \cdot e^{(-1.144 \cdot \overline{V} - 6.439)h} + 6.927 \cdot \overline{V} + 1.025 \quad (5.2)$$

where h is the channel height and $\overline{V}$ is the average air speed.

The numerical results and regression profile of the convective heat transfer coefficients are plotted in Figure 5.15 and 5.16. As can be seen there is a good fit of the regression curves to the numerical results.

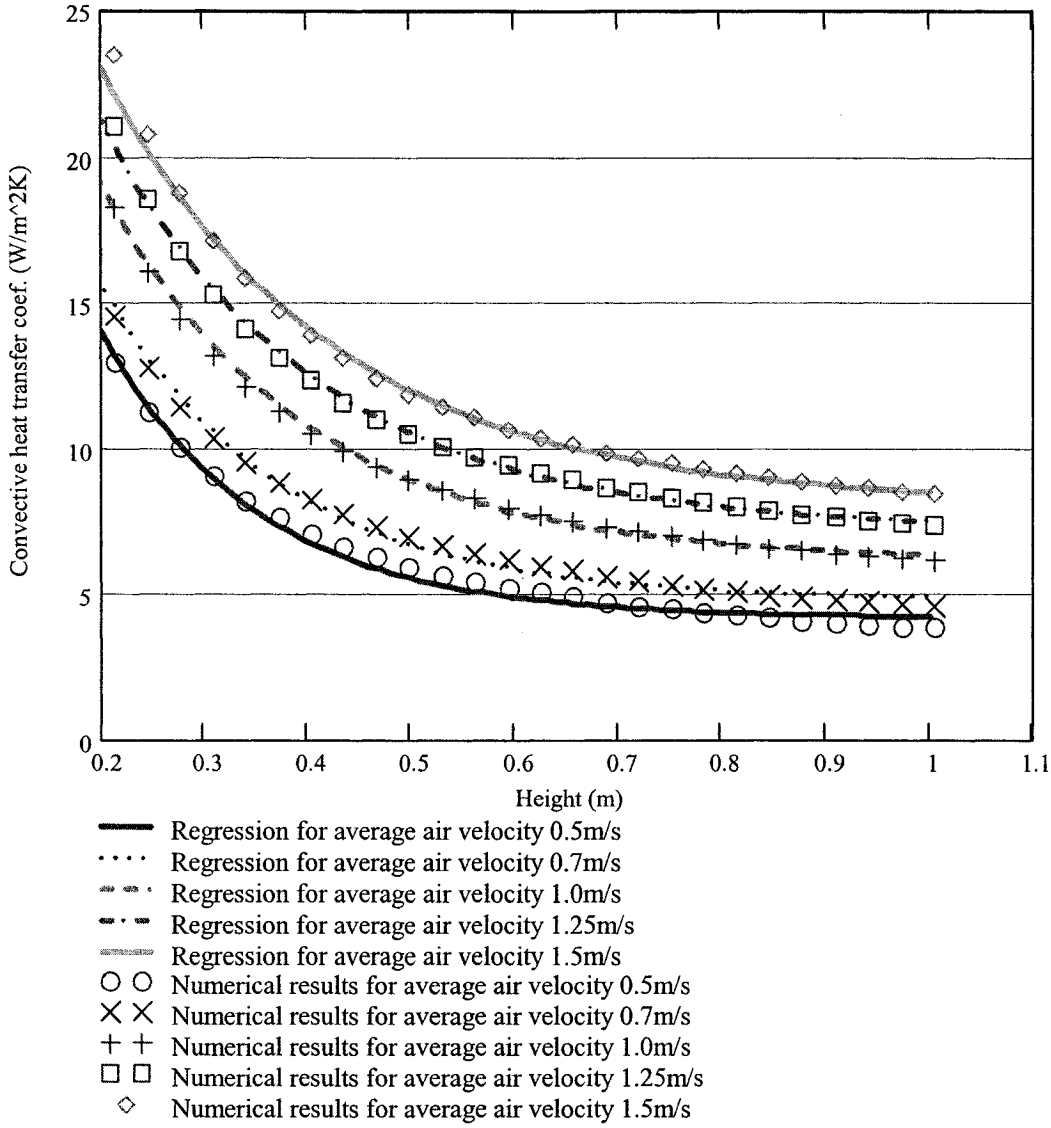

Figure 5.15 Regression for the convective heat transfer coefficients numerical results at PV panel side

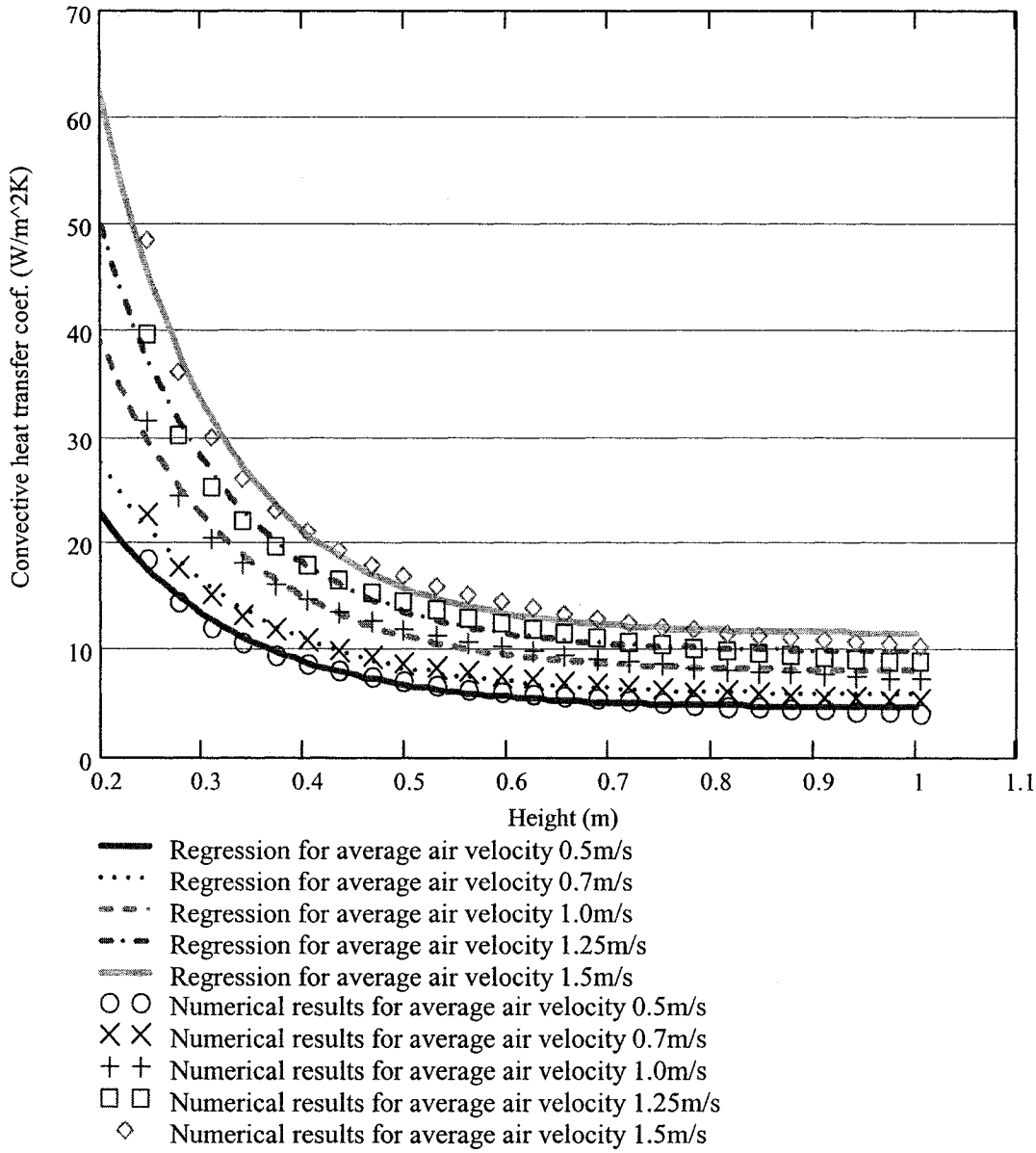

Figure 5.16 Regression for the convective heat transfer coefficients numerical results at insulation side

To generalize this convective heat transfer problem in the air flow channel, non-dimensional characteristic numbers are calculated. For this 2-D fluid flow problem, the cavity gap width is the best value to be used as the characteristic length, and thus the Reynolds number can represent the air flow dynamics well and will not change along the channel height. To divide

the channel height (h) by the width of the cavity (L), we can get the non-dimensional channel height (H). At the same time the local Nusselt number (Nu_H) can represent the same trend of convective heat transfer coefficients along the channel height. Taking the width of the cavity (L) as the characteristic length (see figure 3.1), local Nusselt number can be calculated at different height using the local convective heat transfer coefficient (equation 5.3). Reynolds numbers are generated using the same characteristic length and average air velocity (equation 5.4). Then, the local Nusselt numbers according to non-dimensional channel height and Reynolds numbers can be generated and plotted.

$$Nu_H = \frac{h_c(\overline{V}, h) \cdot L}{K_{air}} \tag{5.3}$$

$$\mathrm{Re} = \frac{\rho \cdot \overline{V} \cdot L}{\mu} \tag{5.4}$$

where,

H is the dimensionless channel height, $H = h / L$

Nu_H is the local Nusselt number,

Re is the Reynolds number.

hc is the local convective heat transfer coefficient

In Figure 5.17 and 5.18, the correlation profile of Nusselt numbers according to non-dimensional height and Reynolds numbers are presented. Figure 5.17 shows the results for PV panel side while Figure 5.18 shows the profiles at the insulation side. Similar regression procession is also taken to get the mathematical formulation of the correlation equation. Exponential form is used for regression because the shape of the correlation profile best fit into this exponential form.

The correlation equation for the local Nu_H at the PV panel side is as below:

$$Nu_H = (0.011 \cdot \mathrm{Re} + 62.856) \cdot e^{-0.475 \cdot H} + 2.766 \times 10^{-3} \cdot \mathrm{Re} + 5.58 \quad (5.5)$$

The correlation equation at the insulation side is as below

$$Nu_H = (0.109 \cdot \mathrm{Re} - 124.344) \cdot e^{(-1.635 \times 10^{-5} \cdot \mathrm{Re} - 0.593)H} + 4.098 \times 10^{-3} \cdot \mathrm{Re} + 3.896 \quad (5.6)$$

From Figure 5.17 and 5.18 we can see that the regression equations 5.5 and 5.6 fit the data points well. The decreasing trend of the Nusselt number along the channel height is presented and big Nusselt number can be observed in the leading edge. Values from the literature are found a bit less than this correlation (Brinkworth 2002; Sparrow and Garcia 1986). Brinkworth (2002) used the Nusselt number developed from thermally-developed channel flow with a fully-developed velocity profile from the beginning. The Nusselt numbers at the heated surface side start from 55 at the inlet region and shrink to 28 at the height ratio (H/D) 100. Since he used the fully-developed velocity profile at the inlet region, the Nusselt numbers are obviously less than the correlation given in this thesis at the inlet region. However, we can see that our correlation stops at the height ratio 11 with a Nusselt number 34 which is near the literature given 32. From the trend of the correlation we can predict that when the flow is becoming fully developed at higher position the correlation will correlate with the literature better. Since the air dynamics are sensitive especially at the inlet region and developing region, the calculated convective heat transfer coefficients or Nusselt numbers may be easily influenced by the boundary settings and ambient conditions. Brinkworth (2002) comments in his paper "the required basic data (Nu_c and θ) on the heat transfer in a parallel-plate duct for simultaneously-developing turbulent flow do not yet seem to hand". Ong (1995) examined various empirical formulas for calculating forced convection heat transfer coefficients between parallel plates and found that the variation between calculated values may range by as much as $\pm 50\%$. The correlation used in Charron's 2-D model resulted in the uncertainty level 10%-21% (Charron 2003c) when compared with the experimental data.

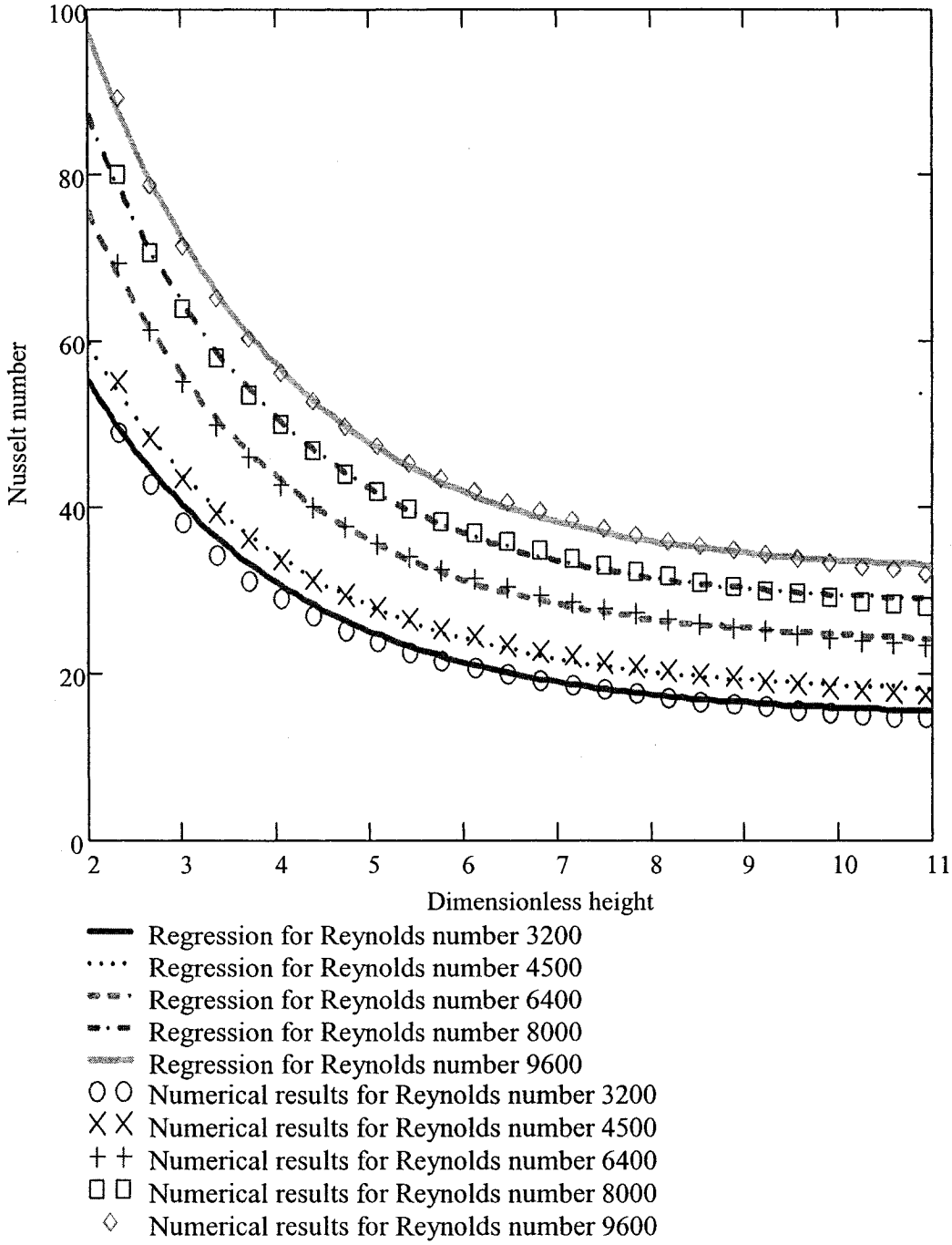

Figure 5.17 Correlation and regression profile of dimensionless numbers at the PV panel side

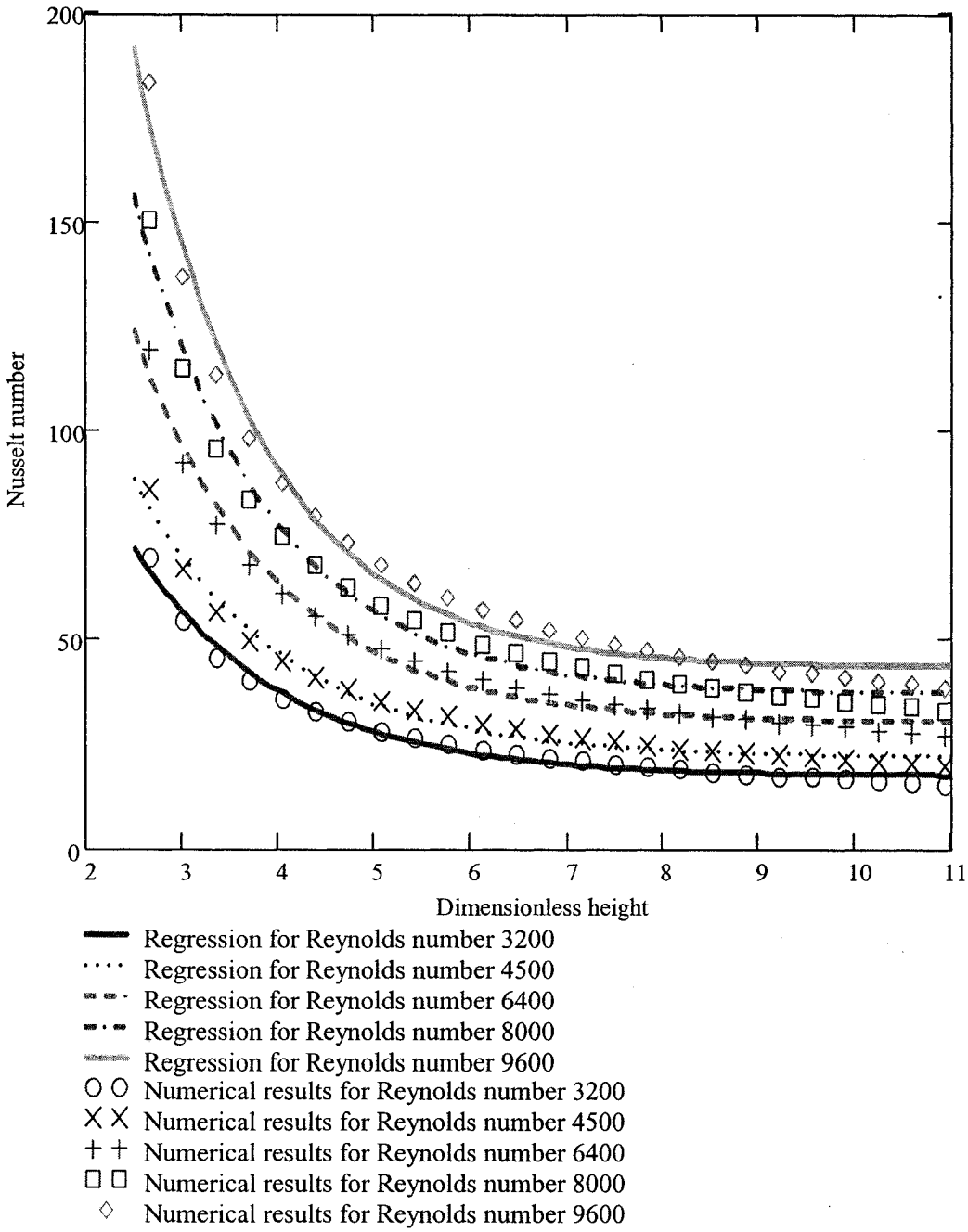

Figure 5.18 Correlation and regression profile of dimensionless numbers at insulation side

5.9 Convective Heat Transfer Coefficient for configuration 2 (Spheral solar side)

The convective heat transfer coefficients and local Nusselt numbers for configuration 1 (Photowatt side) are generated and correlations are regressed. However, due to the complexity of the cavity geometry for configuration 2 (Spheral solar side), these results can hardly be calculated directly from the CFD model. The main difficulties still lie in the turbulent flow in the inlet region. How much the effect of the middle panel will make to the air flow pattern and how much percentage of flowrate goes to each separated cavity? These values are especially hard to predict from the model and thus need the experimental assistance.

Fortunately, we can observe that the cavity for configuration 1 (Photowatt side) and the cavity for configuration 2 (Spheral solar side) have the same type of material, same ambient conditions and same inlet position (left bottom side), so these two cavities should follow the similarity theory of heat transfer. According to this similarity theory of heat transfer, the air flow channels which share the similar physical properties should have the same correlation of dimensionless numbers. Therefore, the correlation of the dimensionless numbers (Equation 5.5-5.6) can be applied to Configuration 2 (Spheral solar side). In addition, with the assistance of the experiment we can calculate the Reynolds number in each separate cavity. Then the local Nusselt number according to height can be generated. Using the separate cavity width as the characteristic length, the convective heat transfer coefficients can finally be evaluated.

From the PIV experiment on March 30th, 2005, we observed that under the fan frequency 15Hz, the average air velocity in the inner cavity is around 0.4 m/s and outer cavity around 0.25 m/s. The cavity width of inner cavity is measured 55 mm and 35 mm for outer cavity. Therefore, the Reynolds number for inner air flow cavity in this situation is calculated to be 1500 and Reynolds number for outer cavity is 600. For this example, we can use the equation 5.5 and 5.6 to derive the local Nusselt number and convective heat transfer for Configuration 2 (Spheral solar side). Substituting the Reynolds numbers into equation 5.5 and 5.6, we can get the correlation of Nusselt numbers according to dimensionless height.

The local Nusselt number at the PV panel in the inner cavity

$$Nu_H = 79.356 \cdot e^{-0.475 \cdot H} + 9.729 \tag{5.7}$$

The local Nusselt number at the insulation in the inner cavity

$$Nu_H = 39.156 \cdot e^{-0.61753 \cdot H} + 10.043 \tag{5.8}$$

The local Nusselt number at the glazing in the outer cavity

$$Nu_H = 69.456 \cdot e^{-0.475 \cdot H} + 7.24 \tag{5.9}$$

The local Nusselt number at the PV panel in the outer cavity

$$Nu_H = -58.9 \cdot e^{-0.603 \cdot H} + 6.355 \tag{5.10}$$

To get the average Nusselt number, we can use the following formulation:

$$Nu_{ave} = \frac{\int_{H1}^{H2} Nu_H dH}{H2 - H1} \tag{5.11}$$

Then the average convective heat transfer coefficient can be generated by:

$$\bar{h}_c = \frac{Nu_{ave} \cdot K_{air}}{L} \tag{5.12}$$

Therefore, under a fan frequency of 15Hz, the average convective heat transfer coefficient for the outer glazing, PV panel outer surface, PV panel inner surface, and insulation surface can thus be calculated to be 4.3W/m^{2}K, 5.3W/m^{2}K, 5.1W/m^{2}K, and 4.6W/m^{2}K.

Under a fan frequency of 30Hz, the average air velocity is around 1 m/s. The air velocities in separate cavities are measured to be 1.2 m/s in inner cavity and 0.3 m/s in outer cavity. The Reynolds number can thus be calculated 4500 for inner cavity and 720 for outer cavity. Using the correlation of equation 5.5-5.6, and following the same procedure given by formula 5.7-5.12, we can generate the average convective heat transfer coefficients. These average

convective heat transfer coefficients for the outer glazing, PV panel outer surface, PV panel inner surface, and insulation surface are calculated to be 4.7 W/m^{2}K, 5.5 W/m^{2}K, 9.2 W/m^{2}K, and 11.3 W/m^{2}K respectively.

From the calculation of the Reynolds number we can observe that the flow is changing from the turbulent flow for Configuration 1 (Photowatt side) to laminar flow in outer cavity for Configuration 2 (Spheral solar side). Hence, the theory of similarity may not be able to predict the accurate convective heat transfer coefficient profile. However, from the experimental results we can observe that the convective heat transfer coefficients profiles are falling into a same exponential shape. Thus this exponential shape assumption is made to get the convective heat transfer coefficient profile according to the average values above.

For a fan frequency 15Hz, the generated convective heat transfer coefficient profiles for the outer glazing, PV panel outer surface, PV panel inner surface, and insulation surface are listed as follows (5.13-5.16):

$$h_c = 36.3 \cdot e^{-6.57 \cdot h} + 2.7 \tag{5.13}$$

$$h_c = 74.4 \cdot e^{-7.2 \cdot h} + 2.2 \tag{5.14}$$

$$h_c = 36.3 \cdot e^{-6.57 \cdot h} + 3.5 \tag{5.15}$$

$$h_c = 74.4 \cdot e^{-7.2 \cdot h} + 1.5 \tag{5.16}$$

For a fan frequency 30Hz, the generated convective heat transfer coefficient profiles for the outer glazing, PV panel outer surface, PV panel inner surface, and insulation surface are listed as follows (5.17-5.20):

$$h_c = 36.3 \cdot e^{-6.57 \cdot h} + 3.1 \tag{5.17}$$

$$h_c = 74.4 \cdot e^{-7.2 \cdot h} + 2.4 \tag{5.18}$$

$$h_c = 49.4 \cdot e^{-8.64 \cdot h} + 7.93 \quad (5.19)$$

$$h_c = 161.11 \cdot e^{-12.13 \cdot h} + 9.83 \quad (5.20)$$

We have to note that since the Reynolds numbers (especially in the outer cavity) for Configuration 2 (Spheral solar side) is quite low compared to Configuration 1 (Photowatt side), therefore the air flow is more likely to appear laminar in the channel. The correlation developed originally from the 2-D turbulent model for Configuration 1 (Photowatt side) may not represent the air dynamics well in this Configuration 2 (Spheral solar side) cavity. Further detailed CFD studies for Configuration 2 (Spheral solar side) are needed to give the most accurate values.

5.10 Energy Balance Prediction of BIPV/T System

Using these convective heat transfer coefficients correlation as input into Charron&Athientis' 2-D model, we can easily calculate the energy fluxes and electricity generation in this BIPV/T system. Since the heat transfer profile function is used, the BIPV/T system can be subdivided into several small control volumes and the thermal performance of each control volume can be calculated separately. Thus the hot spot of the Photovoltaic panel is able to be predicted.

Take the experimental data on Feb. 18th, 2004 for example. The solar radiation on that day was measured 858W/m^2 and ambient air temperature was around -4.0 °C. The experiment was carried on continuously for 30 minutes from 10:50 to 11:20 to avoid the transient effect. The wind effect was low on that day and the experimental data stayed relatively stable.

Using these ambient condition values and the convective heat transfer coefficient correlation (5.1-5.2) into Charron&Athienitis' 2-D model and we can numerically predict the energy balance in this BIPV/T system. The total incident energy to the PV panel is calculated to be 668.8 W. Among this amount of energy, 63.47 W is turned into electricity with an electrical efficiency 9.5%. In addition, 211.16 W is captured by the air flow through convection with a thermal efficiency 31.6%. However, 69.23 W is reflected by PV panel to the outside and 324.94 W is lost to the outside by convection. The combined thermal and electrical efficiency

is around 41.1%. The hottest spot along the PV panel is examined to be at 0.85m high with the temperature 29.3 °C. The predicted PV temperature and insulation surface temperature are presented in Figure 5.19 with comparison to the experimental data. From the figure we can observe that the predicted surface temperatures correlate with the experimental data well (within 3 °C).

With the same ambient conditions, the BIPV system is also numerically studied for Configuration 2 (Spheral solar side). The energy balance is achieved using Charron&Athienitis' 2-D model. The total incident solar radiation is calculated to be 687 W to the whole façade. Among this amount of energy 28 W is turned into electricity with an electrical efficiency 4%. In addition, 155 W of thermal energy is captured by the front cavity and 236 W of thermal energy is captured by the back cavity. The thermal efficiency reaches as high as 47.9%. However, 94 W of the incident radiation is reflected to the outside and 174 W of the energy is lost by convection and radiation. The combined thermal and electrical efficiency rises to 51.9%. The hottest spot along the PV panel is predicted at the top position with the temperature 53 ° C. The comparison of the energy balance prediction is presented in Figure 5.20.

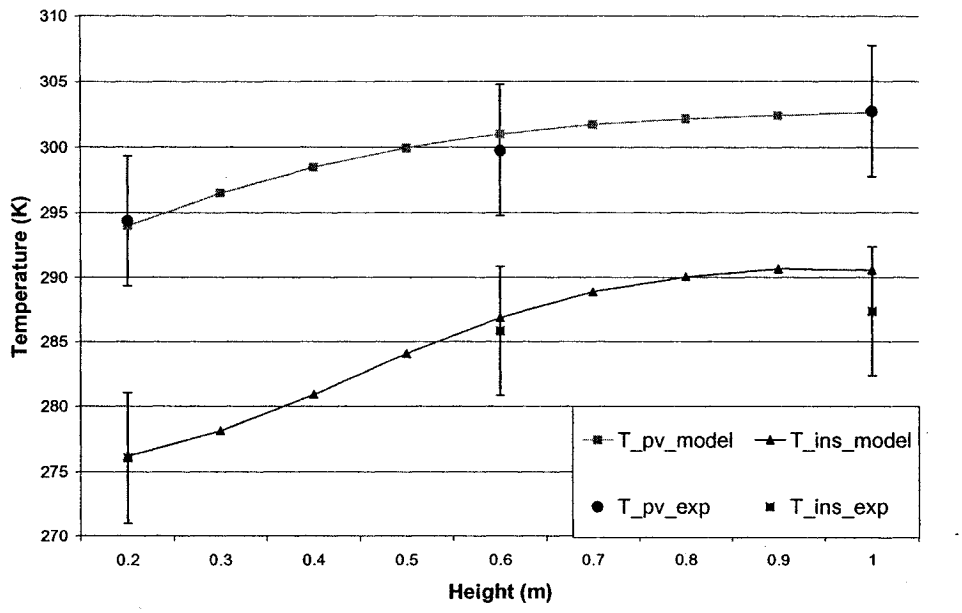

Figure 5.19 PV temperature and insulation surface temperature predictions and comparison with experimental data

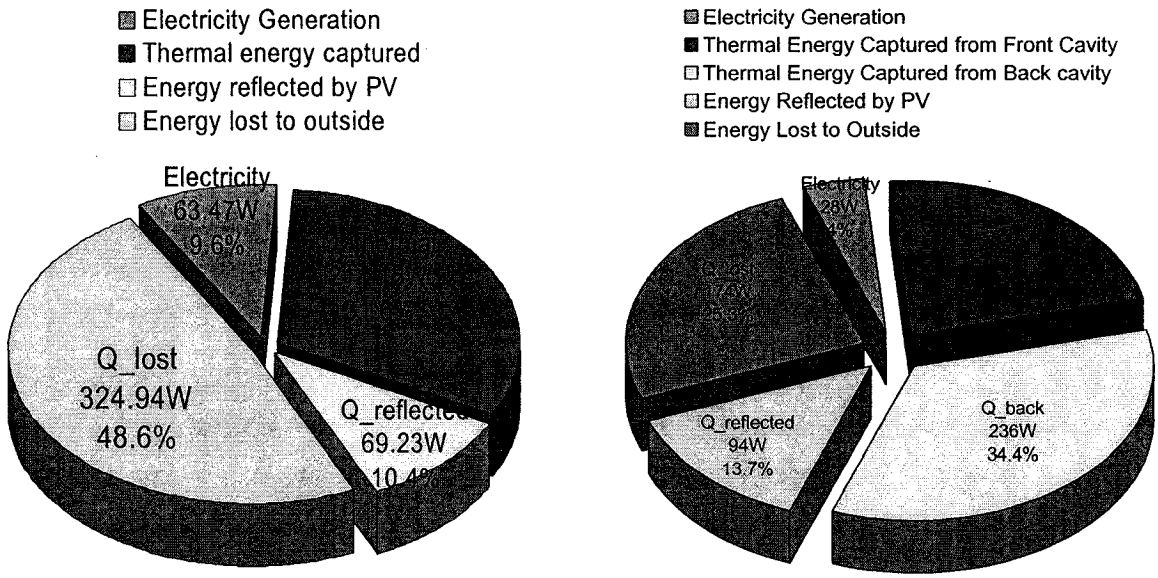

Figure 5.20 Comparison of the energy balance prediction for Configuration 1 (Photowatt side) (left) and Configuration 2 (Spheral solar side) (right)

5.11 BIPV System Optimization

The overall efficiency of the BIPV thermal system is coupled with many parameters, including average air velocity, channel width, channel length, fins usage. Among these, average air velocity and channel width are the parameters that are most important and also most controversial.

From the correlation 5.1-5.2, we can observe that the average air velocity appears as one exponential factor of the convective heat transfer coefficients correlation. In addtion from Fig5.10-Figure 5.11, we can easily discover that the convective heat transfer profile rises when the average air velocity increases. The higher is the average air velocity, the greater is the convective heat transfer coefficient and stronger heat transfer between the surfaces and the air flow. Thus the thermal efficiency is increased and PV panel is more cooled down to generate a higher electrical efficiency also. However, two main points need to pay attention when we

need to increase the air velocity. First, the increase of the air velocity will end up with the quadrate increase of the fan pressure and cubic increase of the fan power. The fan energy consumption will increase dramatically when the air velocity increases. Second, when the average air velocity goes up to 2 m/s in the channel, the sound may become loud enough and annoying. We should try to avoid the air velocity exceeding this level. From the empirical experience, the air velocity is better under 1.5m/s and the BIPV thermal system gives a good performance with the average air velocity around 1m/s for our system.

The channel width may be more challenging to optimize. Among previous correlations, the only related correlation to optimize the channel width is the non-dimensional form. However, the channel width is the characteristic length and appears as part of every dimensionless variable in the correlation. Even the formula optimization needs a lot of mathematics and not easy to figure out. Fortunately, from the PIV investigation and numerical simulation we can observe that the channel flow is still in the developing region in this Configuration (92 mm channel width) and mainly appears like the separate plate flow. Therefore, the small change of the channel width will not influence the heat transfer much. Nevertheless, when the channel width is further shrunk, the two separate plate flow will begin to meet and the velocity profile will change. The thermal boundary layer at each surface will melt into each other and the heat transfer rate is restrained.

Optimization of the other parameters is relatively easier. The increase of the channel height will end up with an increase of the total heat transfer from the PV panel but have negligible effect on the heat flux in unit PV area. The usage of the fins will always help the heat transfer from the surface to the air flow.

Optimization of the whole BIPV thermal system needs to pay special attention to the specific final goals. For this complex system, we have to fix the some parameters first. Normally the channel geometry needs to fix first. Then we can optimize the air flow velocity according to this channel width. Higher air flow velocity will help increase the electrical efficiency and also thermal efficiency and lower air velocity will give a higher air temperature rise. Please note that, for the reasons discussed above, the average air velocity above 2 m/s is not recommended.

5.12 Conclusion

In this chapter, the CFD modeling results are presented. Characteristic flow parameters are investigated to study the air flow dynamics and thermal behavior in the BIPV cavity.

First, the heat transfer rates for different conditions are calculated and compared with each other. The increasing trend of convective heat transfer and stable trend of radiative heat transfer are observed. Later, the temperature profile shows the trend of convective heat transfer from the surface to the air and also the radiative heat transfer from the PV panel to the insulation surface. Velocity profile is generated with detailed investigation of the buoyancy effects on the velocities. This buoyancy effect (stack effect) is more obvious when the flow speed is low however it becomes hard to observe when the flow speed is high and forced convection dominants. Turbulence intensity is also plotted and this result appears a bit lower than the experiment. Then the convective heat transfer coefficients for both PV panel and insulation are calculated for different air velocities. The correlation of the convective heat transfer coefficients for various flow speeds is presented for future use. In addition the correlation between the non-dimensional Nusselt number and Reynolds number is generated. According to the convective heat transfer coefficients for two cavity surfaces, some suggestions of the BIPV system Configuration are discussed. Then the exponential regression correlations for convective heat transfer coefficients are generated for both Configuration 1 (Photowatt side) and Configuration 2 (Spheral solar side). With integration with Charron&Athienitis' 2-D model, the energy balance calculation is finally achieved and the hottest spots of PV panels are predicted. Finally, the optimization of BIPV-thermal system is discussed. Suggestions are given including for the average air velocity optimization and for channel width optimization.

Chapter 6

MODEL VALIDATION

6.1 Introduction

In this chapter, the model is validated using full-scale experimental data. This 2-D CFD model can be hardly compared to the literature because the air flow under study is still in the developing region and mainly turbulent. The complexity of the conjugate heat transfer and uncertainty of the inlet region is not comparable to the simple air flow channel case, so the model is validated using the experimental results with the same geometry settings in the outdoor test facility at Concordia University. The temperature profile at the top of cavity is first compared with the experimental data. Then the velocity profiles for various air velocities are validated using the particle image velocimetry (PIV) results. Finally the predicted surface temperatures using the convective heat transfer coefficient correlation are compared with experimental data under various conditions.

6.2 Comparison of Temperature Profile

For comparison in the similar ambient conditions, the experimental data on February 18th 2004 is chosen. On that day, the ambient temperature was -3.3 °C and wind effect was low. The average PV temperature was measured 25.8 °C which was similar to the boundary setting. The temperature profile was measured using T-type thermocouples at the top of air flow cavity. The experimental result is compared with the modeling result using the same intake temperature and comparison graph is plotted in Figure 6.1.

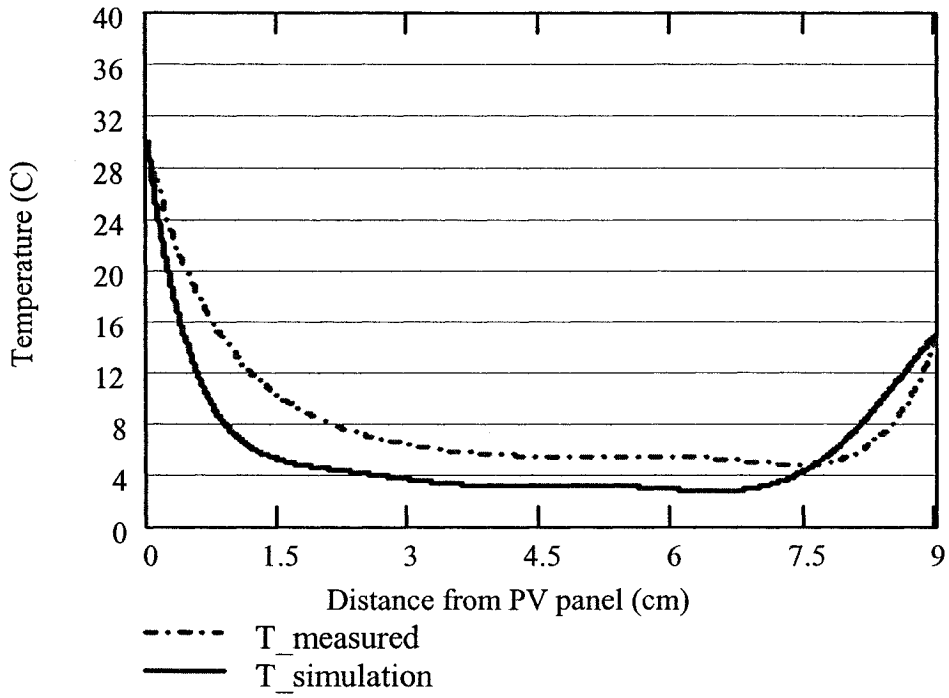

Figure 6.1 Comparison of the outlet air temperature profile from CFD model and experimental measurements.

From the comparison of two curves, we can see that two curves follow the same trend. The temperature falls sharply in the thermal boundary layer from 30 °C to about 4-6 °C and then remains flat in the inflow region until the thermal boundary layer near the insulation, which is heated by the longwave radiation from the PV panel.

Note that the experimental result appears with a little higher temperature near the PV side and with a little lower temperature at the insulation side. This means the heat transfer near the PV side is a little underestimated by the CFD model. The buoyancy effect in real experiment is stronger and caused more turbulence than the CFD model expected and thus enhanced the heat transfer at the PV side. The turbulence intensity predicted by the CFD is around 6-10% and is lower than that measured by the PIV (15-20%) because of wind effects and framing that increase the turbulence in our situation.

6.3 Comparison of Velocity Profile

Since the velocity is coupled with the temperature in the convection term of energy conservation equation and coupled with the pressure difference in the momentum conservation equation and the velocity profile is also influenced by the buoyancy force near the PV panel side, the velocity profile is becoming the key parameter to validate a CFD model. However, due to the difficulty of measurement, the validation of the 2-D velocity profile of BIPV/T system is not yet found in related literature. As discussed in previous chapter the traditional Hot-wire Anemometer is not good to measure the velocity profile in the cavity. In this section, in order to get accurate validation of the CFD model, the velocity profile is investigated with particle image velocimetry (PIV) and comparison result is presented.

Figure 6.2 shows the velocity profile at the top of the cavity from CFD simulations comparing with particle image velocimetry (PIV) experimental data. Average velocities of 0.4 m/s and 1 m/s (from PIV) correspond to a pressure drop of 0.3 Pa and 2 Pa respectively. For the lower flow speed of averagely 0.4 m/s and higher flow speed of averagely 1.0 m/s, the modeling results match the PIV test profile well, within the error range ± 0.05 m/s. As can be seen in the graph, for a low pressure difference of 0.3 Pa, we observe a buoyancy-induced-peak in the velocity profile near the left hot surface (PV panel). As the pressure difference between inlet and outlet is increased, we observe that the buoyancy-induced peak disappears and another small peak appears near the insulation side. This change is predicted from the simulations and is confirmed with the experimental measurements. Since the pressure different used in the CFD boundary settings is not accurate, it is reasonable that the modeling results have some small offset from the experimental measured profile.

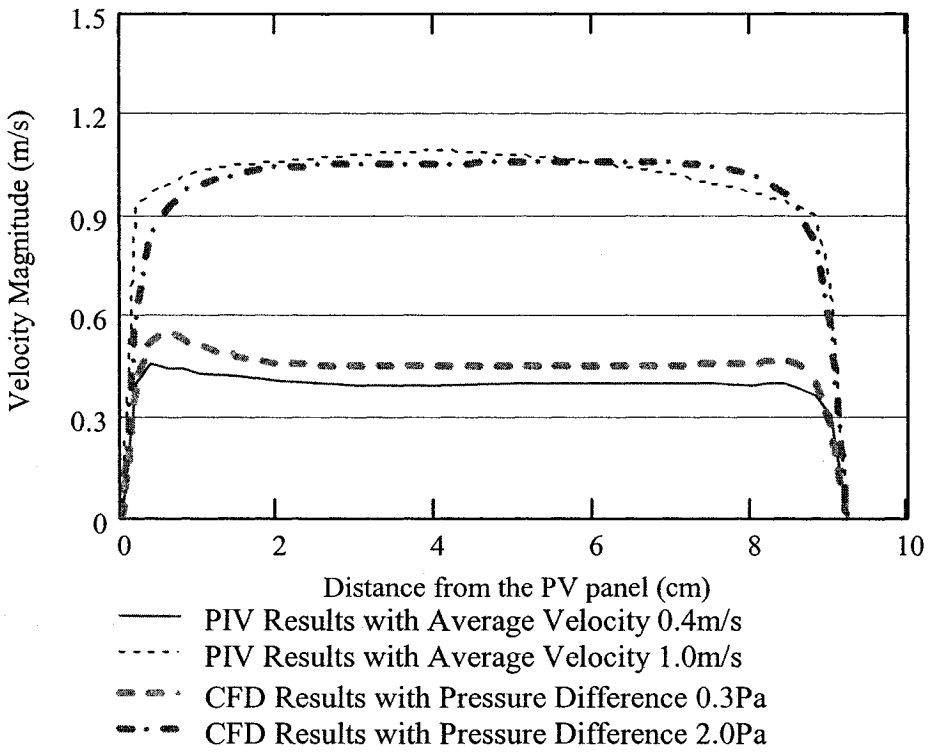

Figure 6.2 Velocity profile from particle-image velocimetry compared with CFD results for two average air velocities

6.4 Comparison of Surface temperatures

Since the convective heat transfer coefficients cannot be compared to the experimental results directly, the surface temperatures are calculated using these convective heat transfer coefficients and compared with accordingly experimental data. Because the other parameters in the heat balance calculation, such as the solar radiation, ambient temperature, outside heat transfer coefficient, are directly measured in the experiment or can be checked out from the literature, the convective heat transfer coefficient is the only unknown in the calculation. Then if the surface temperatures predicted can match the experimental data, the convective heat transfer coefficients are validated.

The average convective heat transfer coefficient is calculated to be 5.8 W/m^2K for the PV panel and 8.6 W/m^2K for the insulation (average of the two is 7.1 W/m^2K). The heat transfer

coefficients are well validated for the velocity range from 0.3 m/s to 0.6 m/s and ambient temperatures from -10 °C to 10 °C. The radiation heat transfer coefficient is 4.8 W/m^2K. These values are substituted into the modified 1-D model (Charron and Athienitis 2003a, b) to predict the PV and insulation temperatures. The 1-D model with two different convective heat transfer coefficients predicted by the two-dimensional CFD model is used to calculate the surface temperature for PV panel and insulation. Table 6.1 shows the comparison of predicted temperatures and experimental data for several days in Montreal, Canada. The predicted temperatures match the experiment within 2 °C. This difference could be attributed to the experimental error of the temperature measurement or the wind effect at the inlet region, or some small variation of the outside heat transfer coefficient.

Integrating the convective heat transfer coefficient profiles with the two-dimensional model by Charron and Athienitis (2003) local PV cell temperatures and local insulation temperatures with various heights are predicted as shown in Figure 6.3. The ambient conditions on March 29th, 2004 are used in the 2-D model and the calculated PV and insulation temperature profiles are compared with the experimental data on that day. The PV panel and insulation are divided into 9 control volumes and solved with the finite volume method (upwind scheme). The model results shown match the experimental data within 2 °C.

Table 6.1: Comparison of experimental and predicted temperatures under quasi-steady state conditions

Experimental Data						Input heat transfer Coefficients				Calculated Results	
Date (2004)	Incident Solar Radiation (W/m2)	Average Velocity (m/s)	To (°C)	Tpv (°C)	Tin (°C)	ho (W/m2K)	hpv (W/m2K)	hin (W/m2K)	hr (W/m2K)	Tpv model (°C)	Tin model (°C)
Feb. 08	1096	0.60	-14.1	21.0	1.7	15	5.8	8.6	4.8	21	4
Feb. 11	1031	0.05	-6.7	34.0	25.4	15	5.0	5.0	4.8	34	28
Feb. 18	858	0.30	-4.0	25.8	10.0	15	5.8	8.6	4.8	24	12
Mar. 10	768	0.30	3.4	35.7	19.1	10	5.8	8.6	4.8	36	21
Mar. 22	944	0.40	-11.4	21.7	6.1	14	5.8	8.6	4.8	21	8
Mar. 29	714	0.40	9.7	34.5	23.6	14	5.8	8.6	4.8	34	24
Mar. 30	712	0.30	10.8	37.2	25.9	13	5.8	8.6	4.8	37	25

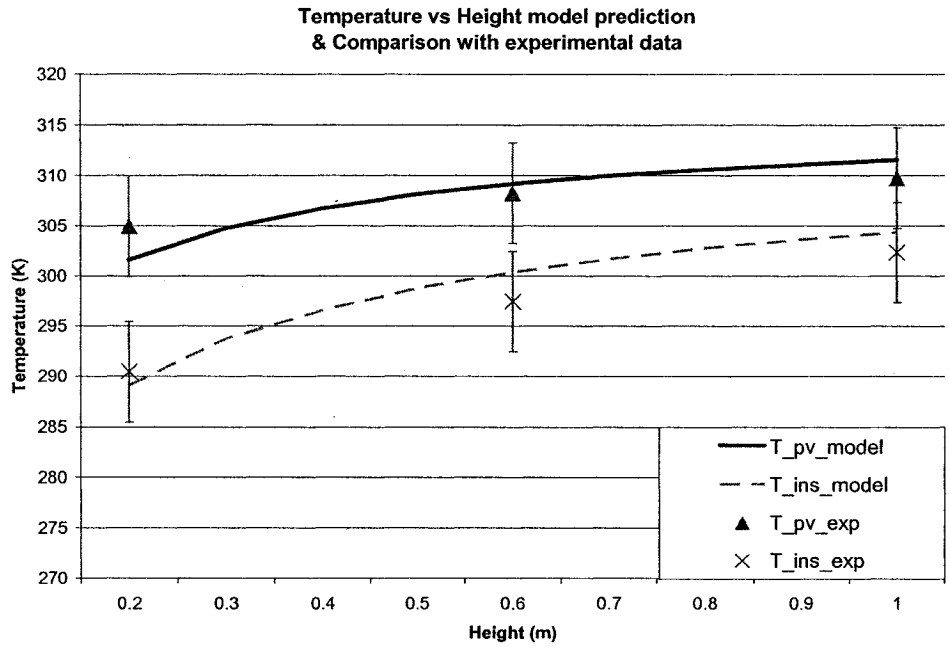

Figure 6.3 Comparison of the predicted PV and insulation temperature profile with experimental data for March 29, 2004

This predicted temperature profile matches the experimental measured profile and thus the convective heat transfer profile generated by the 2-D CFD model is validated. The convective heat transfer profile later can be used to predict the PV temperature profile for different height, and the local cell temperature can be predicted and used to calculate the cell efficiency. The electrical performance of every single PV cell could be predicted. However, these are beyond the objective of this thesis and are not presented here.

6.5 Conclusion

Results obtained from the 2-D CFD model in this thesis correlate well with the experimental investigations. The temperature and velocity profiles at the top of air flow cavity are compared and validated with the experimental profile within the error range ± 2 °C and ± 0.03 m/s respectively. The same trend of the profile and same characteristic of the air dynamics and thermal behavior are found by the comparison of the modeling results and experimental results. The main uncertainty still lies on the inlet region, where the air dynamics are complex

and hard to model in CFD studies. However, since the place where we are most interested in is at some distance higher than the inlet, the detailed modeling of the inlet region is not that costeffective for the objectives and applications of this BIPV thermal system. Another difference can be observed by comparison that the turbulence intensity appears larger in the real measurement than in CFD modeling. This is reasonable because some assumptions have to be made for any CFD modeling and these effects all could result in some reduction of the turbulence in the air cavity.

Convective heat transfer coefficients are validated indirectly. The PV panel temperature and insulation temperature are calculated using these predicted convective heat transfer coefficients and results are compared with the experimental data. Since the convective heat transfer coefficients are the only unknown parameter in the BIPV system, the validation of the surface temperatures will result in the validation of the convective heat transfer coefficients. Comparison shows that the difference between the modeling results and experimental results falls in the range of ± 2 °C, within the error range of measurement. The convective heat transfer coefficients are often used as the key parameter for the whole heat transfer model but difficult to obtain due to the sensitivity of the air. Ong (1995) examined various empirical formulas for calculating forced convection heat transfer coefficients between parallel plates and found that the variation between calculated values may range by as much as $\pm 50\%$. The correlation used in Charron's 2-D model resulted in the uncertainty level 10%-21% (Charron 2003c) when compared with the experimental data. This is also why the predicted results are not compared with the cases in the literature and the experimental investigations under the same geometry settings are the strongest validation for this model.

Chapter 7

CONCLUSION

7.1 Conclusion

A two-dimensional CFD model is successfully developed to study the fluid dynamics and thermal performance inside the BIPV thermal system and develop relationships for convective heat transfer coefficients. A 2-D k-ε turbulent model is used in the FLUENT program to simulate the turbulent flow and convective heat transfer in the cavity, in addition to the buoyancy effect. Longwave radiation between boundary surfaces is also modeled. Experimental measurements taken in a full scale outdoor test facility at Concordia University are in good agreement with the 2-D CFD model.

Experimental investigation of the BIPV thermal system facility built at Concordia University shows that the total system efficiency for configuration 1 (Photowatt side) can reach 62.1% while for Configuration 2 (Spheral solar side) it can reach 78%. In the other side, the electrical efficiency for configuration 1 (Photowatt side) is 8.5% and for configuration 2 (Spheral solar side) it is 4.3%. Particle Image Velocimetry (PIV) is employed to investigate the velocity profile at inlet and outlet inside the cavity. The turbulence in the inlet region is investigated using PIV for fan frequencies of 15Hz and 30Hz. The PIV measuring velocity profile for different fan frequencies are presented for both the Configuration1 (Photowatt side) and Configuration 2 (Spheral solar side). Experiment also shows that black color painting on the back of Spheral solar PV panel can result in increasing the electrical efficiency up to 2-2.5% and putting some reflection materials at the bottom of PV panel can increase the PV electrical efficiency by 1-1.5%.

Using a 2-D CFD model, the temperature and velocity profiles at the top of air flow cavity are predicted and results are in agreement of the experimental profile within the error range ±2 °C and ±0.05 m/s respectively. The same trend of the profile and same characteristic of the air dynamics and thermal behavior are found by comparison of modeling results with

experimental results. The main uncertainty still lies in the inlet region, where the air dynamics are complex and hard to model in CFD studies. Average and local convective heat transfer coefficients for both cavity surfaces are generated. These coefficients are put into exponential regression formula to get the generalized correlation of convective heat transfer coefficients according to average air velocity and channel height. Characteristic dimensionless numbers (Nusselt number, Reynolds number etc.) are also calculated and exponential regression correlations are generated. Since the convective heat transfer coefficients are the only unknown parameter in the BIPV system, the validation of the predicted surface temperatures using these convective heat transfer coefficients will result in the validation of the convective heat transfer coefficients. The PV panel temperature and insulation temperature are calculated using these predicted convective heat transfer coefficients and results are compared with the experimental data. Comparison shows that the difference between the modeling results and experimental results falls in the range of ± 2 °C, within the error range of measurement. These heat transfer coefficients can be utilized in simpler models to facilitate the design of BIPV/T systems.

7.2 Future Work

The BIPV thermal system is a complex system with integration of various components. Therefore simulation and prediction of the performance of such a system accurately is challenging. This thesis is focusing on the air dynamics and thermal behavior simulation using numerical model and experimental investigation. There are still several areas which are just briefly discussed or barely covered in this thesis. These following areas are suggested for future studies:

- A CFD model to study the development of the air dynamics and thermal performance in the blind section. The outlet results of the 2-D model in this thesis can be utilized as the inlet boundary condition into this CFD model.

- The correlation of the system pressure drop according to the air velocity and outside conditions (temperature, solar radiation, wind speed, etc.) needs to be investigated further.

- Proper control strategies of the air flow speed according to the measured pressure drop need to be designed. The ultimate goal of this control strategy is to achieve the maximum system efficiency for building applications in different seasons (summer and winter).

- The effects of the wind speed on this building-integrated photovoltaic system have to be estimated. This study should include how much the wind effect on the outside convective heat transfer coefficients and on the inlet air velocity into the system.

- Optimization methods based on the model predictions and experimental investigations. The optimization method should aim at the ultimate system efficiency for building applications.

REFERENCES

Andrews, G.E., Bradley, D., and Hardy, G.F., (1972), Hot-Wire Anemometer Calibration for Measurements of Small Gas Velocities, Int. Journal of Heat and Mass Transfer, Vol. 15, pp.1765-1786.

Athienitis, A.K. and Santamouris, M., (2002) Thermal Analysis and Design of Passive Solar Buildings, James & James (Science Publishers) Ltd, London, UK

Balocco, C., (2002) A Simple Model to Study Ventilated Facades Energy Performance, Energy and Buildings 34, 469-475

Bartak M., et al. (2002) Integrating CFD and Building simulation, Building and Environment 37, 865-871

Bazilian M.D., Kamalanathan, H. and Prasad, D.K. (2002) Thermographic Analysis of a Building Integrated Photovoltaic System, Renewable Energy 26 (2002) 449-461

Benemann, Joachim and Chehab, Oussama, (1996) Pilkington Solar International For PV Applications in Building, WREC 1996, p452-457

Brinkworth, B.J., (2002) Coupling of Convective and Radiative Heat Transfer in PV Cooling Ducts, Transactions of the ASME, 124, pp. 250-255.

Charron, R. and Athienitis, A.K., (2003a) A Two-Dimensional Model of a PV-Integrated Double-Façade, SESCI CONFERENCE, Kingston, ON, Canada

Charron, R. and Athienitis, A.K., (2003b) Optimization of the performance of PV-integrated double-façades, ISES Solar World Congress, Sweden

Charron, R., (2003c) One- and Two-Dimensional Modeling of Ventilated Façades with Integrated Photovoltaics, M.A.Sc thesis in department of building civil and environmental engineering, Concordia University.

Corrsin, S. (1943), "Investigation of Flow in an Axially Symmetrical Heated Jet of Air," NACAWR-W-94, (Issued as: NACA-ACR-3L23)

DANTEC DYNAMICS website document, Near wall measurements with hot-wirea and hot-film probes require special care, Aerodynamics, Dantec Dynamics website www.dantecdynamics.com

Durst, F., Zanoun, E.-S. and Pashstrapanska, M., (2001) In situ calibration of hot wires close to highly heat-conducting walls, Experiments in Fluids 31, 103-110

FLUENT 6, (2002), User's Guide, Lebanon, USA.

Hinze, J.O., 1975, "Turbulence," McGraw-Hill Book Co., New York

Holman P.J., (1991) Heat Transfer, McGraw-Hill, New York, 1991.

Incropera, F.P., Dewitt, D.P., (1990) Introduction to Heat Transfer, Wiley, New York, 1990, p.524

Khedari, J., Rungsiyopa, M., Sarachitti, R. and Hirunlabh, J., (2004) A New Type of Vented Concrete Block For Zero Cooling Energy, Building and Environment 39 (2004) 1193-1197

Kovasznay, L.S.G., (1959), Turbulence Measurements, Applied Mechanics Reviews, Vol. 12, No.6, pp.375-380

Liao, L. Athienitis, A, and Park, K.W., Poissant, Y., (2005a) Experimental And Numerical Investigation of A BIPV System, ISES Solar World Congress 2005, Orlando, Florida, USA

Liao L., Athienitis, A., and Park, K.W., etc. (2005b) Numerical Study of Conjugate Heat Transfer in a BIPV-Thermal System, ISEC2005, 2005 International Solar Energy Conference, August 6-12, 2005, Orlando, Florida

Lorenzo, Eduardo et al (1994), Solar Electricity. Engineering of Photovoltaic Systems, ISBN: 84-86505-55-0, Institute of Solar Energy Polytechnic University of Madrid

Lowell, H.H., (1950), Design and Application of Hot-Wire Anemometers for Steady-State Measurements at Transonic and Supersonic Airspeeds, NACA-TN-2117

Mei, L., Infield D., etc. (2003) Thermal Modelling of a Building with an Integrated Ventilated PV Façade, Energy and Buildings 35 605-617

Mohammad, H. Hosni, (2002) Development of a Particle Image Velocimetry for Measuring Air Velocity in Large-Scale Room Airflow Applications HI-02019-2 (RP-978) ASHRAE TRANSACTION 2002, V. 108 Pt.2

Mootz, F., Bezian, J.J. (1996) Numerical Study of a Ventilated Façade Panel, Solar Energy, Vol. 57, No. 1, pp29-36, 1996

Moshfegh, B. and Sandberg, M., (1996a) Investigation of Fluid Flow and Heat Transfer In a Vertical Channel Heated From One Side by PV Elements, Part I-Numerical Study, WREC 1996, 248-253

Moshfegh, B. and Sandberg, M., (1996b) Investigation of Fluid Flow and Heat Transfer in a Vertical Channel Heated From One Side by PV Elements, Part II-Experimental Study, WREC 1996, 254-258

Ossenbrink, Heinz, and Helmke, Claas, (1996) Experience With Building Integration Of A Photovoltaic Façade, IEEE 1996, 25th PVSC, May 13-17, Washington, D.C.

Park, C.S., Augenbroe, G., and Messadi, T. etc., (2004) Calibration of a Lumped Simulation Model For Double-skin Façade Systems, Energy and Buildings 36 (2004) 1117-1130

Patankar, S. V., (1980) Numerical Heat Transfer and Fluid Flow, Hemisphre Publishing Corporation

Poissant Y., Couture L., Dignard-Bailey L., Thevenard D., (2003) Simple test methods for evaluating the energy ratings of PV modules under various environmental conditions, ISES Solar Congress 2003, Sweden.

Raithby, G. D. (1976a) A Critical Evaluation of Upstream Differencing Applied to Problems Involving Fluid Flow, Comp. Methods Appl. Mech. Eng., vol 9, p75.

Raithby, G. D. (1976b) Skew Upstream Differencing Schemes for Problems Involving Fluid Flow, Comp. Methods Appl. Mech. Eng., vol. 9, p153

Saelens D., (2002) Energy Performance Assessment of Single Storey Multiple-Skin Facades, PhD Thesis, Katholieke Universiteit Leuven.

Saelens, D., Roels, S. and Hens, H., (2004) The Inlet Temperature as a Boundary Condition for Multiple-Skin Façade Modeling, Energy and Buildings 36 825-835

Sanberg M., (1999) Cooling of Building Integrated Photovoltaics by Ventilation Air, HybVent Forum 1999, Sydney.

Sandborn, V.A., (1972), "Resistance Temperature Transducers", Metrology Press, Fort Collins, Colorado.

Sparrow, E. M., Garcia, A., and Chuck, W., (1986) "Numerical and Experimental Turbulent Heat Transfer Results for a One-sided Heated Rectangular Duct", Numerical Heat Transfer, 9, pp301-322.

Stainback, P.C. and Nagabushana, K.A., (1996) Review of Hot-Wire Anemometry Techniques and the Range of their Applicability for Various Flows, Electronic Journal of Fluids Engineering, Transactions of the ASME

Warren M.R., James P. H., Young I.C., (1998) Handbook of Heat Transfer, 3rd Edition, McGraw-Hill, New York, 1998

Zhai Z., et al., (2002) On Approaches to Couple Energy Simulation and Computational Fluid Dynamics Program, Building and Environment 37, 857-864

Zollner, A., Winter, E.R.F., and Viskanta, R., (2002) Experimental Studies of Combined Heat Transfer in Turbulent Mixed Convection Fluid Flows in Double-skin-facades, International Journal of Heat and Mass Transfer, 45, pp. 4401-4408.

APPENDIX A

Mathcad program to process the experimental data
and calculate the BIPV/T system efficiency

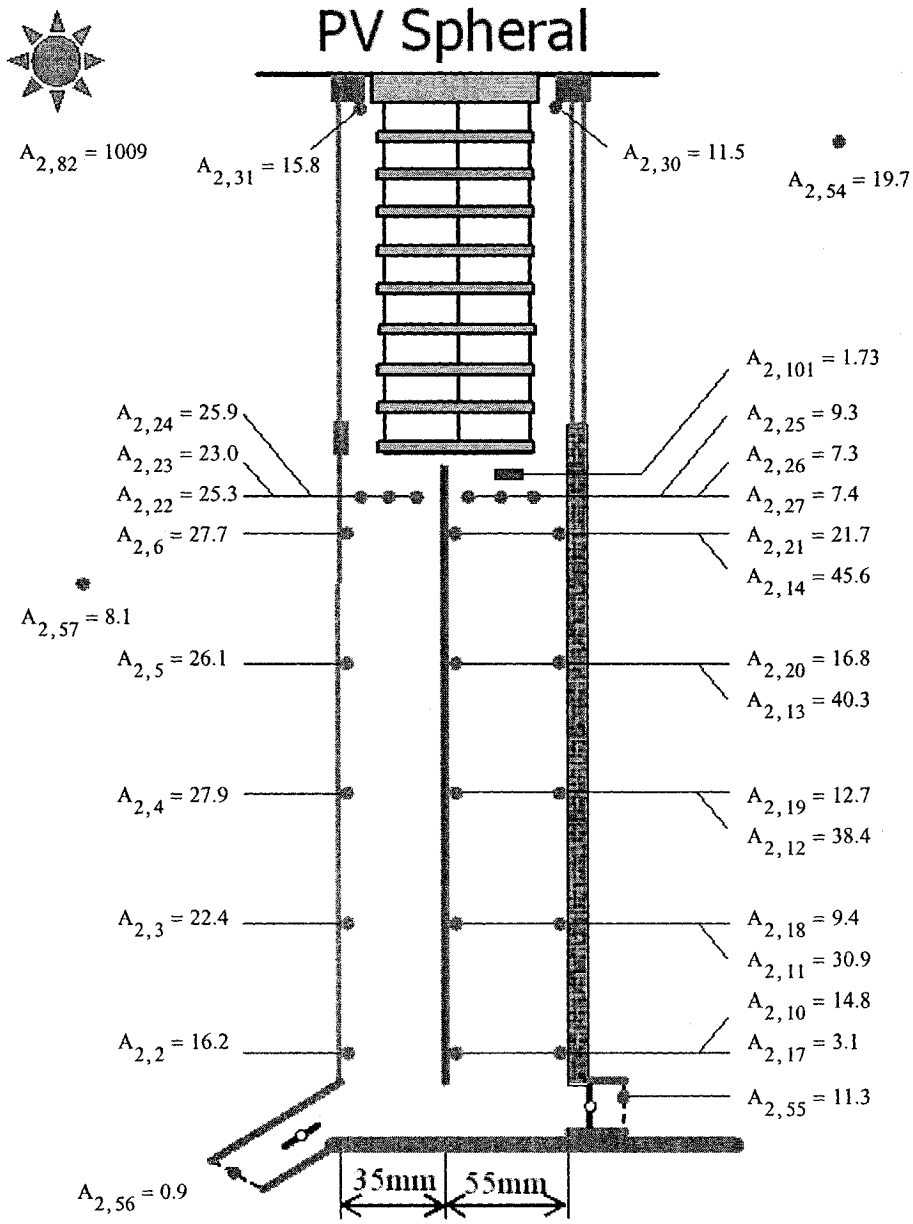

Reflector not covered ref = 1.1

$$T_{glz\_ave} := \frac{A_{2,2} + A_{2,3} + A_{2,4} + A_{2,5} + A_{2,6}}{5}$$

$T_{glz\_ave} = 24.0 degC$

$$T_{pv\_sph\_ave} := \frac{A_{2,10} + A_{2,11} + A_{2,12} + A_{2,13} + A_{2,14}}{5}$$

$T_{pv\_sph\_ave} = 34.0 degC$

$$T_{wall\_ave} := \frac{A_{2,17} + A_{2,18} + A_{2,19} + A_{2,20} + A_{2,21}}{5}$$

$T_{wall\_ave} = 12.7 degC$

CALCULATION OF OVERALL EFFICIENCY

$S := A_{2,82}\,\text{ref}\cdot\frac{\text{watt}}{\text{m}^2}$ incident total solar (approx. 150 is diffuse)

gap_width $Li := .055\,\text{m}$ $Lo := .035\,\text{m}$ $L := Li + Lo$ $Sdiff := 150\frac{\text{watt}}{\text{m}^2}$

Average measured velocities

$Vo := 0.24\,A_{2,101}\,\frac{\text{m}}{\text{sec}}$ $Vi := 0.71\,A_{2,101}\,\frac{\text{m}}{\text{sec}}$

$Vo := 0.3\frac{\text{m}}{\text{s}}$ $Vi := 1.2\frac{\text{m}}{\text{s}}$ **Overwrite the value using the PIV data**

$V := \frac{Vi\cdot Li + Vo\cdot Lo}{Li + Lo}$ **overall average velocity** $V = 0.85\frac{\text{m}}{\text{s}}$

Dimensions of panels (two panels in series)

Total width $W := 0.912\,\text{m}$ Height $\text{height} := 1.12\,\text{m}$

$Asph := W\cdot\text{height}$ $Asph = 1.021\,\text{m}^2$

$t\alpha := 0.84$ for spheral around noon $\tau\alpha_{diff} := 0.54$ assume tau diffuse = 0.54

Absorbed solar radiation: $Sa := Asph\cdot\left[t\alpha\cdot(S - Sdiff) + \tau\alpha_{diff}\,Sdiff\right]$ $Sa = 906.1\,\text{W}$

$Tintake := A_{2,56}$ Intake air temperature $To := A_{2,57}$ Ambient temperature $To = 8.1\,\text{degC}$

$Tintake = 0.9\,\text{degC}$

$Tair\_in\_top := \frac{A_{2,25} + A_{2,26} + A_{2,27}}{3}$ Average temperatures at top of inner and outer cavities

$Tair\_in\_top = 8.0\,\text{degC}$

$Tair\_o\_top := \frac{A_{2,22} + A_{2,23} + A_{2,24}}{3}$

$Tair\_o\_top = 24.7\,\text{degC}$

$Tav := \frac{Vi\cdot Li\cdot Tair\_in\_top + Vo\cdot Lo\cdot Tair\_o\_top}{(Li + Lo)\cdot V}$ mixed air T at top of spheral PV $Tav = 10.3\,\text{degC}$

$Tair_{i\_ave} := 0.5\cdot(Tair\_in\_top + Tintake)$ $Tair_{o\_ave} := 0.5\cdot(Tair\_o\_top + Tintake)$ Average air temp. for heat transfer coefficient calculation

$DT := Tav - Tintake$ Temperature rise of the air heated by spheral PV $DT = 9.4\,\text{degC}$

$c := 1003\frac{\text{joule}}{\text{kg}\cdot\text{degC}}$ ...air specific heat $Tave\_air\_mid := Tintake + \frac{DT}{2}$

$p := 1 \cdot atm$ $R_a := 287.08 \frac{joule}{kg \cdot K}$ $\rho := \frac{p}{R_a \cdot (Tave\_air\_mid + 273) \cdot K}$

$\rho = 1.267 \frac{kg}{m^3}$ density of air

$Qthermal_i := Li \cdot W \cdot Vi \cdot \rho \cdot c \cdot (Tair\_in\_top - Tintake)$ $Qthermal_o := Lo \cdot W \cdot Vo \cdot \rho \cdot c \cdot (Tair\_o\_top - Tintake)$

$Qthermal_i = 543.836W$ $Qthermal_o = 289.908W$ $Qthermal_i + Qthermal_o = 833.7W$

Thermal energy $Qthermal := L \cdot W \cdot V \cdot \rho \cdot c \cdot DT$ $Qthermal = 833.7watt$

Heat transfer coefficient calculation

$Qthermal_i = h_i \cdot W \cdot height \cdot (T_{pv\_sph\_ave} + T_{wall\_ave} - 2 \cdot Tair_{i\_ave})$

$Qthermal_{oi} = h_o \cdot W \cdot height \cdot (T_{pv\_sph\_ave} + T_{glz\_ave} - 2 \cdot Tair_{o\_ave})$

$hcav_i := \frac{Qthermal_i}{W \cdot height \cdot (T_{pv\_sph\_ave} + T_{wall\_ave} - 2 \cdot Tair_{i\_ave})}$ $hcav_i = 14.062 \frac{watt}{degC \cdot m^2}$

$hcav_o := \frac{Qthermal_o}{W \cdot height \cdot (T_{pv\_sph\_ave} + T_{glz\_ave} - 2 \cdot Tair_{o\_ave})}$ $hcav_o = 8.745 \frac{watt}{degC \cdot m^2}$

Resistance of load at maximum power point [redacted] ohms

$Pelectric := \frac{(A_{2,84})^2}{R_{sph}} \cdot watt$ $Pelectric = 49.0W$

$effi\_elec := \frac{Pelectric}{S \cdot Asph}$ $effi\_elec = 0.043$

$effi\_tot := \frac{Qthermal + Pelectric}{S \cdot Asph}$ $effi\_tot = 0.779$

Energy Balance Analyze:

$$ho := \frac{0.9 \cdot A_{2,82}}{A_{2,53} - A_{2,57}} \cdot \frac{watt}{m^2} \qquad ho = 24.678 \frac{watt}{m^2}$$

Overwrite ho if the value is not good

$$ho := 15 \frac{watt}{m^2} \qquad (10 - 15)$$

$Qtotal1 := S \cdot Asph$ $\quad Qtotal1 = 1133W$

$\rho_{ref} := 0.05$ $\quad Q_{loss\_conv} := ho \cdot (T_{glz\_ave} - To) \cdot Asph$ $\quad Q_{loss\_conv} = 244.519W$

$(0.05 - 0.10)$

$Q_{loss\_rad} := \rho_{ref} \cdot S \cdot Asph$ $\quad Q_{loss\_rad} = 56.672W$

$Q_{loss} := Q_{loss\_conv} + Q_{loss\_rad}$ $\quad Q_{loss} = 301.192W$

$Qthermal = 833.744W$

$Pelectric = 48.999W$

$Qtotal2 := Q_{loss} + Qthermal + Pelectric$ $\quad Qtotal2 = 1184W$

If the Qtotal1=Qtotal2, it means the energy balance is achieved.

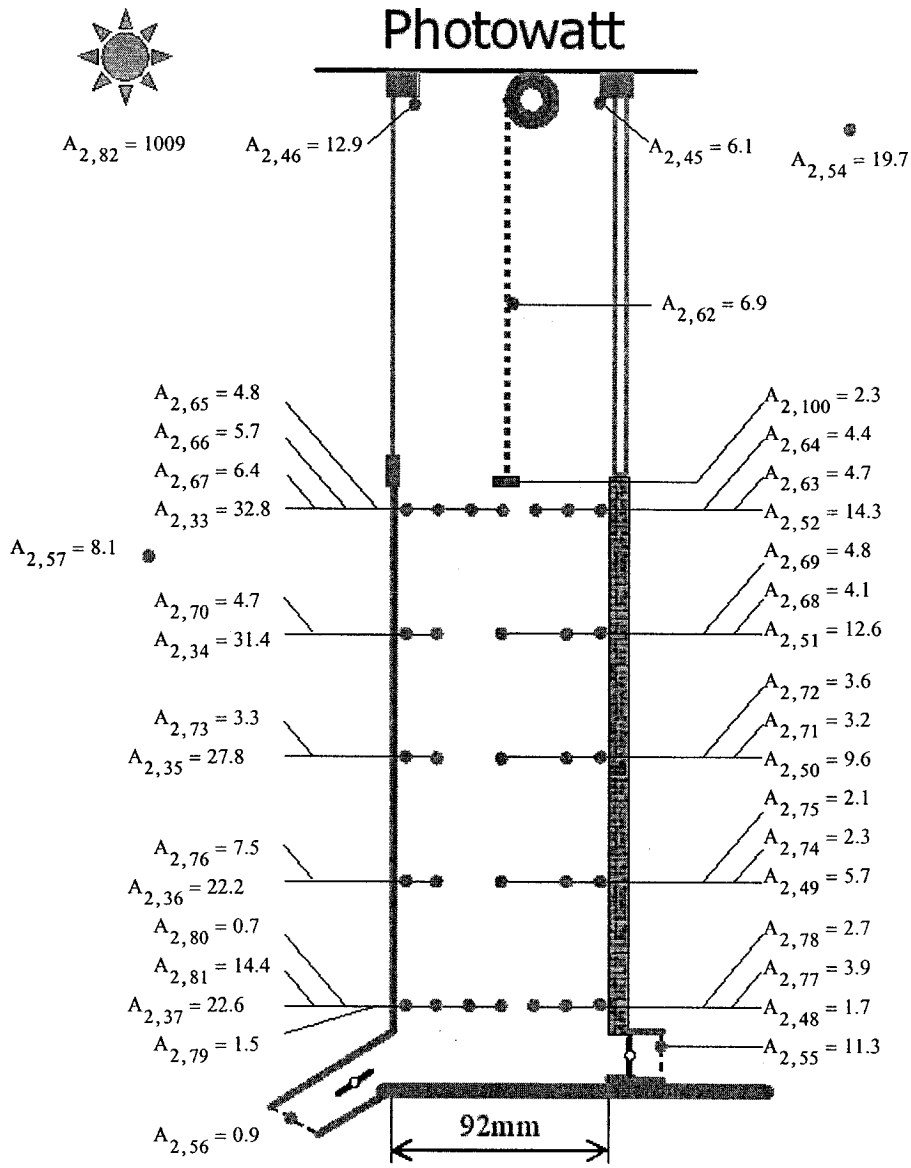

$$Tpw\_ave := \frac{A_{2,37} + A_{2,36} + A_{2,35} + A_{2,34} + A_{2,33}}{5}$$

$Tpw\_ave = 27.4 degC$

$$Tpw\_wall\_ave := \frac{A_{2,48} + A_{2,49} + A_{2,50} + A_{2,51} + A_{2,52}}{5}$$

$Tpw\_wall\_ave = 8.8 degC$

gap_width $Lpw := 0.092\,m$

Air velocity $Vpw := 0.5 \cdot A_{2,100} \cdot \frac{m}{sec}$ $Vpw = 1.165 \frac{m}{s}$

Dimensions of panels Total width $Wpw := 0.906\,m$ $Hpw := 0.993m$

$Apw := Wpw \cdot Hpw$ $Apw = 0.9m^2$

$t\alpha := 0.94$ $\tau\alpha_{diff} := .6$ assume tau diffuse = 0.6

Absorbed solar radiation: $Sa := Apw \cdot \left[t\alpha \cdot (S - Sdiff) + \tau\alpha_{diff} \cdot Sdiff\right]$ $Sa = 892.5W$

$Tpw\_air := \frac{A_{2,63} + A_{2,64} + A_{2,65} + A_{2,66} + A_{2,67}}{5}$ Average air temperature at top of panels $Tpw\_air = 5.2degC$

$Tpw\_in := \frac{A_{2,77} + A_{2,78} + A_{2,79} + A_{2,80} + A_{2,81}}{5}$ Average temperature of air at bottom of panels $Tpw\_in = 4.6degC$

Intake air temperature

$DT := Tpw\_air - Tintake$ **Air temperature rise (heated by PV)** $DT = 4.3degC$

$Tave\_air\_mid := Tintake + \frac{DT}{2}$

$p := 1 \cdot atm$ $R_a := 287.08 \frac{joule}{kg \cdot K}$ $\rho := \frac{p}{R_a \cdot (Tave\_air\_mid + 273) \cdot K}$

$\rho = 1.279 \frac{kg}{m^3}$ Density of air

Thermal energy

$Qthermal := Lpw \cdot Wpw \cdot \rho \cdot Vpw \cdot c \cdot (Tpw\_air - Tintake)$ $Qthermal = 535.1W$

Electric energy

Resistance of load at maximum power point [redacted] ohms

$Pelectric := \frac{(A_{2,83})^2}{R_{pv}} \cdot watt$ $A_{2,83} = 36.461$ $Pelectric = 84.7W$

$\frac{37.1^2}{\frac{15.7}{900}} = 0.097$

$effi := \frac{Qthermal + Pelectric}{S \cdot Apw}$ $effi = 0.621$

$\eta e := \frac{Pelectric}{(S \cdot Apw)}$ $\eta e = 0.085$

Energy Balance Analyze:

$$ho := \frac{0.9 A_{2,82}}{A_{2,53} - A_{2,57}} \cdot \frac{watt}{m^2} \qquad ho = 24.678 \frac{watt}{m^2}$$

Overwrite ho if the value is not good

$$ho := 15 \frac{watt}{m^2}$$

$Qtotal1 := S \cdot Apw$ $\quad Qtotal1 = 998W$

$\rho_{ref} := 0.1$

$Q_{loss\_conv} := ho \cdot (T_{glz\_ave} - To) \cdot Apw$ $\quad Q_{loss\_conv} = 215.366W$

$Q_{loss\_rad} := \rho_{ref} \cdot S \cdot Apw$ $\quad Q_{loss\_rad} = 99.831W$

$Q_{loss} := Q_{loss\_conv} + Q_{loss\_rad}$ $\quad Q_{loss} = 315.197W$

Qthermal = 535.079W

Pelectric = 84.675W

$Qtotal2 := Q_{loss} + Qthermal + Pelectric$ $\quad Qtotal2 = 935W$

If the Qtotal1=Qtotal2, it means the energy balance is achieved.